Detection of Biological Tissue Anomalies Using Low-Frequency Electromagnetic Fields

by

Hamid Akbari Chelaresi

A thesis
presented to the University of Waterloo
in fulfillment of the
thesis requirement for the degree of
Doctor of Philosophy
in
Electrical and Computer Engineering

Waterloo, Ontario, Canada, 2025

© Hamid Akbari Chelaresi 2025

Examining Committee Membership

The following served on the Examining Committee for this thesis. The decision of the Examining Committee is by majority vote.

External Examiner:	Natalia Nikolova Professor, Dept. of ECE, McMaster University
Supervisor:	Omar M. Ramahi Professor, Dept. of ECE, University of Waterloo
Internal Member:	Amir Hamed Majedi Professor, Dept. of ECE, University of Waterloo
Internal Member:	George Shaker Associate Professor, Dept. of ECE, University of Waterloo
Internal-External Member:	Parsin Haji-Reza Professor, Dept. of SYDE, University of Waterloo

Author's Declaration

I hereby declare that I am the sole author of this thesis. This is a true copy of the thesis, including any required final revisions, as accepted by my examiners.

I understand that my thesis may be made electronically available to the public.

Abstract

This PhD thesis presents a novel biomedical imaging modality—proposed and developed for the first time—for the detection of breast cancer using low-frequency electromagnetic (EM) fields. The core principle stems from the fact that the penetration depth of EM waves into biological tissues is inversely proportional to their operating frequency. Unlike conventional high-frequency imaging techniques, this approach leverages sub-GHz frequencies (hundreds of MHz), which offer significantly deeper tissue penetration, making them particularly suitable for imaging dense breast tissues (BI-RADS categories C and D), where conventional X-ray mammography fails.

Operating at low frequencies introduces critical challenges in designing radio-frequency (RF) components that are compact, human-compatible, and suitable for clinical deployment. To address this, a novel low-frequency metasurface-based film antenna—conceptually analogous to traditional X-ray films—has been developed. This metasurface sensor effectively captures scattered EM fields after interaction with biological tissues, enabling high-fidelity imaging while operating within a non-ionizing and biologically safe frequency range.

The proposed system is cost-effective and portable, with strong potential for widespread deployment in low-resource settings where access to magnetic resonance imaging (MRI) is limited. Unlike MRI, which is expensive and not readily available, or ultrasound, which is prone to operator-dependent errors, this technique enables consistent and repeatable screening.

Also, this work investigates the impact of various EM sources on image resolution and contrast. It is shown that magnetically enhanced sources significantly improve field-tissue interaction, thereby increasing sensitivity to early-stage tumorous anomalies. Advanced post-processing algorithms, including differentiation techniques and both supervised and unsupervised machine learning models, were implemented to enhance image quality and minimize diagnostic errors, further improving the system's diagnostic performance.

The methodology has been rigorously validated through both numerical simulations and experimental studies. Multiple iterations of the transmitter antennas and metasurface sensors have been developed, optimized, and evaluated throughout the course of the research. The final system demonstrates high accuracy in detecting early-stage abnormalities.

Moreover, this thesis introduces a new low-frequency tomography method, also for the first time, that reconstructs images of internal tissues by modeling the X-ray-like behavior of localized, electrically small transmitters and receivers. A novel mathematical framework has been proposed and implemented using Radon transform techniques, enabling accurate spatial reconstruction of the object under test.

Acknowledgements

I am profoundly thankful to my supervisor, Professor Omar M. Ramahi, for his exceptional mentorship, continuous support, and inspiring conversations. His guidance extended far beyond academic matters, offering me valuable insights into both research and life itself. The opportunity to learn from him has been a rare and invaluable experience that I will always cherish.

I would like to sincerely thank my committee members, Prof. George Shaker, Prof. Parsin Haji-Reza, Prof. Karim Karim, and Prof. Amir Hamed Majedi, for their valuable feedback, insightful comments, and support throughout this process.

Special thanks to Prof. Vahid Nayyeri for his support and assistance.

I would like to acknowledge my colleagues during my Ph.D. studies at the University of Waterloo. Specifically, I would like to thank Seyed Hossein Mirjahanmardi, Ghazaleh Tashtarian, Saleh Ba Rayan, and Rania Rabhi.

Dedication

To my beloved parents for their unconditional love and support.

Table of Contents

Examining Committee Membership ii

Author's Declaration iii

Abstract iv

Acknowledgements v

Dedication vi

List of Figures x

List of Tables xvii

1 Introduction 1

1.1 Motivation 1

1.2 Project Description and Objectives 2

1.3 Thesis Outline 2

2 Literature review 4

2.1 X-ray Imaging 4

2.1.1 Conventional Radiography 5

2.1.2 Computed Tomography (CT) 5

2.1.3 Fluoroscopy . . . 6
2.1.4 Healthcare Efficiency and Safety Enhancement by Digital X-Ray Imaging Technology . . . 7
2.2 Magnetic Resonance Imaging (MRI) . . . 8
2.3 Positron Emission Tomography (PET) . . . 9
2.4 Ultrasound Imaging . . . 10
2.5 Microwave Imaging . . . 12
2.5.1 Microwave Tomographic Imaging . . . 14
2.5.2 Radar-Based Microwave Imaging . . . 21
2.6 New modalities in Microwave Imaging . . . 28
2.6.1 Low-frequency Computerized Tomography . . . 28
2.6.2 Microwave Film . . . 31

3 Using Low-Frequency Electromagnetic Fields for Breast Cancer Detection 38
3.1 Introduction . . . 38
3.2 Unitcell Design . . . 41
3.3 LFEM Imaging System Design . . . 45
3.4 Numerical Simulation, Results, and Discussion . . . 48
3.5 Deep learning classifications . . . 52
3.6 Deep Feature Learning for Microwave Mammography With Convolutional Autoencoders . . . 57
3.7 The Proposed Prototype Implementation . . . 59

4 Source Optimization for Enhanced Imaging Performance in LFEMF Modality 61
4.1 Introduction . . . 61
4.2 Investigation of Fundamental Electromagnetic Excitation Sources . . . 62
4.3 Design of Magnetic-field Dominant Excitation Source . . . 69

4.4 Metasurface Fabrication . . . 74
4.5 System Evaluation . . . 75
4.5.1 Realistic Numerical Phantom Models . . . 75
4.5.2 Simulation Results . . . 80
4.5.3 Experimental Validation . . . 87

5 Design and Implementation of a Miniaturized Metasurface Receiver for Enhanced LFEMF Imaging 91
5.1 Introduction . . . 91
5.2 Miniaturized Metasurface Design . . . 92
5.3 Simulation Results . . . 96
5.4 Experimental System Setup . . . 99
5.4.1 Using Dipole Antenna as the Source . . . 101
5.4.2 Using Loop Array Antenna as the Source . . . 105
5.5 Data Acquisition automatization . . . 108

6 Quasi-Electrostatic Computerized Tomography 113
6.1 Introduction . . . 113
6.2 Theory of Quasi-Electrostatic Computerized Tomography . . . 116

7 Conclusion and Future Work 129
7.1 Accomplished Work . . . 129
7.2 Future Work . . . 132
7.2.1 Suggestion 1 . . . 132
7.2.2 Suggestion 2 . . . 133
7.2.3 Suggestion 3 . . . 133

References 135

List of Figures

2.1 Sensing principle of UPT and image reconstruction of inclusions with different acoustic impedance [27]. 13

2.2 Displaying the imaging system prototype devised by Meaney et al.: (a) Depiction of the examination table. (b) Illustration of the data acquisition system with the microwave source [36]. 17

2.3 The retrieved 900 MHz relative permittivity and conductivity images from Patient 1 for the left breast [36]. 18

2.4 The retrieved 900 MHz relative permittivity and conductivity images from Patient 1 for the right breast [36]. 18

2.5 Grzegorczyk et al.'s breast cancer testing prototype system: (a) Exhibits a 3D schematic of the testing setup. (b) Displays a photograph of the system's hardware [46]. 19

2.6 3D microwave tomographic permittivity images at 1300 MHz from Grzegorczyk et al.'s system: (a) Shows the tumor in the right breast. (b) Depicts the tumor-free left breast [46]. 19

2.7 (a) Illustrates the entire system, and (b) specifically presents the breast holder featuring the antenna array immersed in a liquid bath [47]. 20

2.8 Diagram of the system devised by Son et al [47]. 22

2.9 Images of a breast model with a 10 mm cylindrical tumor at 1,700 MHz: (a) without a tumor, (b) tumor at the center, and (c) tumor 30 mm right of center. Circles mark actual breast and tumor boundaries [47]. 22

2.10 The TSAR prototype, a radar-driven Medical Imaging (MI) system designed by Fear et al., is engineered for detecting breast cancer through tissue sensing [49]. 24

2.11 (a) Depicts an aerial view of the antenna and laser setup. (b) Presents the breast holder assembly, featuring a tank, laser, and antennas [49]. 24

2.12 Images reconstructed by the TSAR system developed by Fear et al [49]. . 25

2.13 System configuration developed by Porter et al [50]. 25

2.14 A breast cancer detection system utilizing an antenna array equipped with a radome [50]. 26

2.15 Image reconstruction from the breast phantom detection system developed by Porter et al. The tumor is highlighted by a red spot; the "x" markers indicate antenna positions, while the diamond markers represent the actual tumor center locations [50]. 27

2.16 Configured setup for analyzing the OUT as illustrated in Figure 15: featuring the transmitter, receiver, OUT, 50 Ω - cables, positioner, and vector network analyzer [55]. 29

2.17 Analysis of a four-layer cylinder and its projection profiles: (a) placement between transmitter and receiver. (b) receiver's collection of magnitude transmission coefficient profile, $|S21|$, relative to location [55]. 30

2.18 Reconstructed image of one slice of the OUT shown in Fig. 2.17 (a) [55]. . 30

2.19 (a) Schematic depiction of the designed ELC unit cell. (b) Simulation outcomes of the unit cell featuring the reflection coefficient S11 and the power dissipation in the resistive load at the resonance frequency of 1.9 GHz. (c) Surface current distribution on the ELCs at the resonance frequency. The visualization uses a color gradient where red indicates the highest intensity at 112 A/m, and blue denotes the lowest intensity at 0 A/m. The uneven current distribution near the edge of the metasurface arises from the lack of periodicity in those particular unit cells. (d) Metasurface scanning procedure demonstrating the length and direction of the scan steps. The inset illustrates the sequence of scanning steps [2]. 32

2.20 Models depicting an extremely dense breast: (a) featuring a 5-mm tumor and (b) without a tumor. Power pattern recordings on the metasurface film for various breast models: (c) displaying a breast with a cancerous tumor and (d) without a tumor. The red arrows highlight specific areas of differentiation compared to (c) [2]. 33

3.1 a) 3D view of the unitcell, (b) top view, and (c) bottom view. 43

3.2 $|S_{11}|$ for different values of (a) t, (b) L, and (c) $R_1 = R_2$, where the non-variant parameters are set to L = 100nH, $R_1 = R_2 = 470\Omega$, and t = 40 mm. (d) $|S_{11}|$ and power delivered to the terminal resistors of the optimized unit-cell, where the incident power is 0.5 Watts. 44

3.3 Metasurface array (10 cm × 10 cm): (a) top view and (b) bottom view, showing the two termination resistors (c) scanning technique for increasing the pixels of the impression, where $\Delta x = 1$ cm is the length of the square unitcell. The arrows show the directions of the displacements. (d) breast model, inclusing skin, fat tissues, fibro-glandular tissues, and a tumor positioned at C_t with the diameter of 10 cm. 46

3.4 Simulation setup 49

3.5 (a) Simulation model of the healthy breast (b) simulation model of the tumorous breast (c) recorded impression of the healthy breast (d) recorded impression of the tumorous breast, where the red circles indicate the border of the tumor with a radius of 10 mm and location of C_{t_1} (see TABLE 3.2). 50

3.6 Model of the tumorous breast with a 10 mm tumor placed in: (a) upper-left corner, (b) upper-right corner, (c) lower-left corner, and (d) lower-right corner with the corresponding impressions shown in (e)-(h), respectively. . 51

3.7 Model of the tumorous breast with a 7.5 mm tumor placed at: (a) upper-left corner, (b) upper-right corner, (c) lower-left corner, and (d) lower-right corner with the corresponding impressions shown in (e)-(h), respectively. . 52

3.8 Model of the tumorous breast with a 5 mm tumor placed at: (a) upper-left corner, (b) upper-right corner, (c) lower-left corner, and (d) lower-right corner with the corresponding impressions shown in (e)-(h), respectively. . 53

3.9 Increment of the fat tissues in the dataset breast models 53

3.10 (a) Deep learning architecture composed of seven convolutional neural networks and two fully connected layers. (b) Graph of loss function's values for training and validation sets over 100 epochs. The model with the least validation loss is marked with x and used for testing purposes. 54

3.11 t-SNE visualization of the training data for twelve classes shown in TABLE 3.3. (a) Based on the features extracted from the deep learning architecture (b) Based on the HOG features. 56

3.12 Auto-encoder network composed of encoder, latent space, and decoder sections. (a) Complete network schematic, (b) Input image, (v) Reconstructed output obtained by the designed auto-encoder model. 58

3.13 UMAP visualization of the training data for all twelve classes belonging to various tumor sizes and locations 58
3.14 Mammography system setup 60

4.1 Schematic of the system setup featuring an electrically small dipole antenna. 63
4.2 Schematic of the system setup featuring an electrically small circular loop antenna. 64
4.3 (a) Electric field amplitude calculated for (a) the healthy breast and (b) the breast with a tumor. 65
4.4 Captured image of a tumorous breast using electric field. Red circles indicating the borders of an 8 mm radius PEC tumor located at the bottom of the breast. 65
4.5 (a) Magnetic field amplitude calculated for the healthy breast and (b) magnetic field amplitude calculated for the breast with a tumor. 66
4.6 Captured image of a tumorous breast using magnetic fields. Red circles indicating the borders of an 8 mm radius PEC tumor located at the bottom of the breast. 66
4.7 Captured images of a tumorous breast with red circles indicating the borders of an 8 mm radius spherical tumor with a permittivity of 80 and conductivity of 3, located at the bottom of the breast, using (a) the electric field and (b) the magnetic field. 67
4.8 Captured images of a tumorous breast with red circles indicating the borders of an 5 mm radius spherical PEC tumor,located at the bottom of the breast, using (a) the electric field and (b) the magnetic field. 67
4.9 Captured images of a tumorous breast with red circles indicating the borders of an 8 mm radius spherical PEC tumor located in the middle of the breast using (a) the electric field and (b) the magnetic field. 68
4.10 (a) Design of the proposed transmitter antenna and (b) Photograph of the fabricated prototype of the transmitter antenna. 71
4.11 $|S_{11}|$ of the transmitter antenna. 72
4.12 a) 3D view of the unitcell, (b) top view, and (c) bottom view. 76
4.13 $|S_{11}|$ of the unitcell. 77

4.14 Top view (facing the breast) of the fabricated 10×10 unit cell array using FR-4. 77
4.15 Photograph of the fabricated prototype of the metasurface: (a) the top view and (b) the back view. 78
4.16 Simulation setup with the heterogeneously dense breast numerical phantom. The plate above the breast represents the antenna, while the bottom thick plate represents the metasurface. 81
4.17 (a) Simulation model of the healthy breast and (b) recorded impression of the healthy breast. 82
4.18 Simulation model of the tumorous breast: (a) the side view (b) the top view. 83
4.19 Recorded impression of the tumorous breast with a spherical PEC tumor of 10 mm radius. 83
4.20 The difference in power distributions between the healthy and tumorous breast with a spherical PEC tumor of 10 mm radius. 84
4.21 Tumorous breast model with a spherical PEC tumor (radius: 10 mm) positioned at four distinct coordinates: (a) (15 mm, -15 mm, 36 mm), (b) (15 mm, 15 mm, 35 mm), (c) (-15 mm, -15 mm, 35 mm), and (d) (-15 mm, 15 mm, 36 mm). The difference in power distributions between the healthy and tumorous breasts, corresponding to each tumor position, is shown in (e), (f), (g), and (h), respectively. 84
4.22 The difference in power distributions between the healthy and tumorous breasts with a spherical PEC tumor located at the bottom of the breast, with tumor radii of (a) 8 mm, (b) 7 mm, (c) 6 mm, and (d) 5 mm, respectively. 85
4.23 (a) Model of a tumorous breast with a tumor having a radius of 8mm, permittivity of 80, and conductivity of 3 S/m, and (b) the difference in power distributions between the healthy and tumorous breasts. 86
4.24 (a) Experimental setup for the detection modality. (b) OUT with the transmitter antenna and metasurface. 89
4.25 Difference in power distributions between the cases without the inclusion and with the inclusion positioned at (0 mm, 0 mm) in the x-y plane. 90
4.26 Difference in power distributions between the cases without the inclusion and with the inclusion positioned at the corner of the x-y plane. 90

5.1 (a) Perspective view (b) top view, and (c) bottom view of the unitcell, where $w = 3.3$ mm, $t = 1.6$ mm, $R_O = 1.5$ mm, $R_I = 1.3$ mm, $C = 250$ pF. . . . 92
5.2 Voltage across the capacitor vs frequency graph 93
5.3 (a) Top view of the metasurface (b) bottom view of the metasurface 94
5.4 Simulation setup: (a) healthy phantom (b) phantom with inclusion 97
5.5 Obtained impressions for (a) healthy phantom (b) phantom with 10-mm radius PEC inclusion 97
5.6 Subtracted impression, where the location of the inclusion has been illustrated by the circle. 98
5.7 Obtained impressions for (a) healthy phantom (b) phantom with 5-mm radius realistic inclusion. 99
5.8 Subtracted impression, where the location of the inclusion has been illustrated by the circle 99
5.9 (a) Transmitter antenna and (b) the stacked-up experimental setup, where the bottom of the layout is exposed 101
5.10 The image captured of the object under test 102
5.11 The image captured for the case that a metallic inclusion placed in the middle of the object under test 103
5.12 The image after subtracting the healthy model and the one with inclusion . 104
5.13 Imaging system setup, including the signal generator, power amplifier, isolator, transmitter antenna, metasurface antenna, oscilloscope, and PC. . . 106
5.14 The photograph of the experimental system setup highlights the object under test, displaying the stacked-up layers integral to the configuration. . . . 107
5.15 The obtained image highlights the anomaly, with its location distinctly marked by the blue box for clear identification. 107
5.16 Schematic of the 4-layer PCB: (a) top layout (b) bottom layout 109
5.17 Schematic of the 4-layer PCB: (a) mechanical layer 1 (b) mechanical layer 2 109
5.18 Controlling circuit of the switching network 110
5.19 PCB design (back layout) 111

6.1 The electric intensity observed when stimulating the structure with a localized electrostatic source positioned in the near-field region, with media 1 to 6 having the subsequent permittivities:$\epsilon_1 = 2\epsilon_0$, $\epsilon_2 = 6\epsilon_0$, $\epsilon_3 = 2\epsilon_0$, $\epsilon_4 = 2\epsilon_0$, $\epsilon_5 = 2\epsilon_0$, and $\epsilon_6 = 2\epsilon_0$. 118

6.2 electrostatic computed tomography system setup. 119

6.3 Back-projected graph from the source side to the detector side. 120

6.4 Fourier transform of g(ρ_k,θ_l) from the x-y plane to u-v plane. 121

6.5 (a) Back-projected profiles g(ρ,θ_l) with different angles of θ_l (b) the corresponding sinogram of $\theta = \theta_1 = 0°$ (c) $\theta = \theta_2 = 45°$, and (d) $\theta = \theta_3 = 90°$. 122

6.6 (a) OUT-1 model for one tumor (b) X-polarized excitation (c) Y-polarized excitation at $\theta_l = 0°$. 123

6.7 Pencil beam setup. 123

6.8 (a) The obtained image using the pencil beam method for OUT-1 for the X-polarized source (b) for the Y-polarized source. 124

6.9 Fan beam setup. 125

6.10 Images obtained using the fanbeam method for OUT-1 for the X-polarized source (b) for the Y-polarized source. 126

6.11 (a) OUT-2 model for two cylindrical inclusions. (b) X-polarized excitation (c) Y-polarized excitation at $\theta_l = 0°$. 126

6.12 Images obtained using the pencilbeam method for OUT-2 for the X-polarized source (b) for the Y-polarized source. 127

6.13 Images obtained using the fanbeam method for OUT-2 for the X-polarized source (b) for the Y-polarized source. 127

List of Tables

2.1 Comparison between traditional cancer detection techniques 13

2.2 Summary of clinical investigations of microwave and conventional breast imaging systems 36

2.3 Summary of different MI methods and algorithms 37

3.1 Design Parameters of the unitcell 42

3.2 various locations of the tumor 47

3.3 Size and location of the tumors for different classes 55

4.1 Comparison between the electric field generated by a dipole antenna and the magnetic field generated by a circular loop antenna. 69

4.2 Geometrical Features of Spiral Resonators 70

4.3 Design Parameters of the Feeding Network 74

4.4 Design Parameters of the unitcell 76

4.5 Breast Tissue Parameter 78

Chapter 1

Introduction

1.1 Motivation

The absence of an affordable, non-invasive, and high-resolution breast cancer detection technology poses significant challenges for early-stage diagnosis. Current methods, with issues like ionizing radiation exposure, enduring scanning time, and limited image quality, necessitate the development of a new non-hazardous, low-cost, and easy-to-use system. While X-ray mammography is the current gold standard, its drawbacks include patient discomfort and radiation risks [1] . Microwave imaging, utilizing non-ionizing electromagnetic waves, offers deep tissue penetration but copes with resolution limitations. To address this challenge, metasurface antenna, configured as an array of detectors, shows promise in detecting breast tissue malignancies [2, 3] . Metasurface antennas are types of antennas constructed from an arrangement of closely spaced electrically-small resonators [4–6] . These resonators can have various patterns and can be either planar or three-dimensional. The geometry and dimensions of these resonators directly affect their resonant frequency. At the resonance frequency, they are able to store electromagnetic energy in their near-field range. This characteristic, combined with the inherent narrow-bandedness of electrically-small resonators, makes them well-suited for sensing applications, where the object under test is in close proximity to the sensor.

1.2 Project Description and Objectives

In our recent research [7], we introduced a novel low-frequency electromagnetic field (LFEMF) mammography system. This system utilizes an electrically-small antenna (ESA) as a transmitter, positioned in the near field of the female breast. The use of ESA enables comprehensive excitation of breast tissues, as ESAs can emit a wide variety of polarizations in their near-field region while radiating. To enhance image resolution, we developed a metasurface with highly miniaturized unit cells operating at 200 MHz, achieving a level of miniaturization equivalent to $\lambda/150$. This metasurface can be conceptualized as an LFEMF film effectively capturing images, where each unit cell acts as pixels composing the resulting image. Subsequently, deep neural networks (DNNs) are employed to analyze the captured images. Remarkably, DNNs have achieved an impressive 100% accuracy rate in classifying healthy and unhealthy breast tissue impressions within the provided dataset framework. Notably, DNNs could not only detect tumors but also precisely identify their locations and sizes.

While this study has demonstrated the feasibility of the proposed concept, our other endeavors will focus on constructing a prototype to empirically validate the effectiveness of our detection method. Our goal is to implement the mammography system configuration depicted in Fig. 3.14, serving as a preliminary demonstration of the proposed setup. We assessed various strategies to advance our project, including enhancing the radiated power of the transmitter antenna to facilitate more interactions between breast constituents and electromagnetic waves. Additionally, we explored alternative scanning methods to enhance breast tissue characterization and refined unit cell miniaturization for higher image resolution. Furthermore, our exploration extended to different deep learning algorithms, encompassing both supervised and unsupervised image categorization.

1.3 Thesis Outline

In the second chapter, we explored conventional cancer detection methods, such as x-ray, Magnetic Resonance Imaging (MRI), Positron Emission Tomography (PET), and Ultrasound Imaging. We thoroughly examined their methodology, excitation source, cost, resolution, and user-friendliness, along with their respective advantages and drawbacks. Subsequently, we explored microwave-based techniques for identifying anomalous tissues in the body, categorizing them into passive, hybrid, and active methods. Active microwave methods, including tomography and radar-based approaches, were extensively reviewed

in the literature. Additionally, two emerging modalities, low-frequency computerized tomography, and the use of microwave film for image-impression recording, were introduced, laying the foundation for our subsequent discussion in Chapter 3.

In Chapter 3, we presented our initial work, commencing with the design of a miniaturized low-frequency ELC resonator with dimensions of $\lambda/150$, operating at 200 MHz. These resonators were then organized into an array of 10 $\times$ 10, forming a metasurface or low-frequency electromagnetic film for capturing body impressions. Following this, we simulated 144 scenarios involving various tumor sizes and locations in diverse breast models. The resulting dataset underwent analysis using a supervised deep learning algorithm, yielding highly accurate classification outcomes.

In Chapter 4, we examined how the choice of source affects the performance of the proposed LFMEMF modality. Specifically, we analyzed various electromagnetic sources and their impact on image quality. The primary sources evaluated were electric dipole and magnetic dipole antennas. Our findings indicated that magnetic dipole antennas provided superior performance in detecting anomalies within the breast. Building on this, we introduced a loop-array transmitter, designed as an array of loops to deliver uniform illumination to the target and enhance magnetic field interactions within the body. This system was subsequently fabricated, implemented, and experimentally validated by the end of the chapter.

In Chapter 5, we introduced a novel metasurface antenna capable of accommodating a significantly higher number of pixels—900 instead of 100—within the same 10 cm $\times$ 10 cm area. This design also simplifies the fabrication process, as the substrate thickness was reduced from several centimeters, which posed challenges for PCB manufacturing, to just a few millimeters—consistent with standard PCB substrates. Furthermore, by integrating nine times more pixels within the same area as the LFEMF film, the proposed antenna considerably improves the image resolution.

In Chapter 6, we explored an image reconstruction method aimed at fully reconstructing the object under test within the proposed low-frequency cancer detection modality. This method was inspired by traditional CT scan reconstruction techniques and employed the Radon Transform. For the first time in a low-frequency system, we demonstrated that by using electrically and physically compact electromagnetic transmitters and receivers—along with pencil beam and fan beam approaches—the full reconstruction of the object is achievable, rather than merely obtaining a rough impression.

In Chapter 7, the research will be concluded, and recommendations for future work will be presented.

Chapter 2

Literature review

Advancements in medical imaging technologies have revolutionized the landscape of cancer detection and diagnosis, offering a diverse array of modalities that cater to varying aspects of the disease. Magnetic Resonance Imaging (MRI), X-ray, Positron Emission Tomography (PET), Ultrasound, and Microwave imaging represent a spectrum of powerful diagnostic tools, each offering distinct advantages in visualizing, characterizing, and localizing cancerous tissues within the human body. The unique capabilities of these modalities, from the high-resolution anatomical detail of MRI to the metabolic insights provided by PET, and the promising emerging realm of Microwave imaging, have collectively propelled the field of oncology towards more precise, early, and comprehensive detection strategies. This review delves into the individual strengths, limitations, clinical applications, and the evolving role of each imaging modality in the context of cancer detection, presenting a comprehensive overview of their contributions to the field.

2.1 X-ray Imaging

Conventional Radiography, Computed Tomography (CT), and Fluoroscopy are all medical imaging techniques that use X-rays to produce images, but they differ in their specific applications, technology, and how they create and visualize these images.

2.1.1 Conventional Radiography

Conventional radiography, also known as X-ray imaging, is a fundamental and widely utilized diagnostic tool in medicine. It relies on the use of X-rays, a form of electromagnetic radiation, to create two-dimensional images of the body's internal structures. X-rays are produced by an X-ray tube that emits a controlled amount of radiation, which passes through the body and interacts with various tissues. Upon exposure to the body, X-rays are absorbed differently by different tissues: denser structures like bone absorb more radiation and appear as lighter areas on the resulting images, while less dense tissues like muscles or organs allow more X-rays to pass through and appear darker. This creates a high-contrast image that aids in identifying abnormalities, fractures, and certain conditions within the body[8, 9].

The applications of conventional radiography span various medical fields. It is commonly used to detect and evaluate bone fractures, providing detailed images that aid in diagnosing the location and severity of fractures, enabling treatment planning. Additionally, X-rays of the chest are valuable in diagnosing conditions such as pneumonia, lung cancer, and other respiratory diseases. In dentistry, dental X-rays are routinely used to visualize teeth, gums, and jawbones, aiding in the identification of cavities, bone loss, and other dental issues. While its primary strength lies in bone imaging, it can also occasionally reveal abnormalities in soft tissues, such as tumors or foreign objects[10].

Despite its widespread use, conventional radiography has certain limitations. One major drawback is its relatively lower soft tissue contrast compared to other advanced imaging modalities like magnetic resonance imaging (MRI) or computed tomography (CT). This means that while it is excellent at displaying bones and certain abnormalities, it may not provide as much detail or clarity in visualizing soft tissues. Moreover, since X-rays involve ionizing radiation, there's a concern about cumulative radiation exposure, although modern machines have significantly reduced the radiation dose, making X-ray imaging a safer and more efficient diagnostic tool than in the past. Despite these limitations, it remains an invaluable and cost-effective method for diagnosing and monitoring a wide range of medical conditions and injuries[11].

2.1.2 Computed Tomography (CT)

Computed Tomography (CT) is an advanced medical imaging technique that generates detailed cross-sectional images of the body, providing more comprehensive and in-depth views than conventional X-rays. A CT scanner combines a rotating X-ray machine with a

sophisticated computer to create detailed, three-dimensional images of the body's internal structures. The CT scanner captures a series of X-ray images from multiple angles around the body, producing thin cross-sectional slices that are then reconstructed by the computer into detailed images. This technology allows for the visualization of tissues, organs, and abnormalities with remarkable clarity and precision[12].

The applications of CT imaging are extensive. It is particularly useful in diagnosing various medical conditions and injuries. It provides detailed images of the head, chest, abdomen, and pelvis, aiding in the detection and evaluation of tumors, fractures, blood clots, infections, and other abnormalities. In emergency settings, CT scans are often used to rapidly assess traumatic injuries, helping guide immediate medical interventions. Furthermore, it is utilized in treatment planning and monitoring the effectiveness of certain therapies due to its ability to capture detailed anatomical and pathological information[13].

One of the strengths of CT imaging lies in its ability to capture high-resolution images of soft tissues, bones, and blood vessels. This distinguishes it from conventional radiography by offering a more comprehensive view of internal structures. However, despite its diagnostic advantages, CT scans use ionizing radiation, which, while generally safe, presents a slight risk of cumulative radiation exposure over time. Efforts in the field continually aim to optimize scanning techniques and reduce radiation doses to maintain safety while maximizing the diagnostic benefits of this powerful imaging modality. The evolution of CT technology has led to advancements in areas such as multi-slice CT, spectral CT, and the integration of artificial intelligence, enhancing both image quality and diagnostic capabilities[14].

2.1.3 Fluoroscopy

Fluoroscopy is a dynamic and real-time medical imaging technique that employs X-rays to create continuous moving images of the body's internal structures. It operates using a fluoroscope, which consists of an X-ray source and a detector, typically a fluorescent screen or a digital monitor. The X-ray source emits a continuous beam of radiation that passes through the patient's body, and the resulting images are displayed in real-time on a monitor. This allows medical professionals to view the movement and function of organs, tissues, or structures as they occur, aiding in various diagnostic and interventional procedures[15].

The applications of fluoroscopy are diverse and widespread across medical specialties. In gastroenterology, it is used to visualize the gastrointestinal tract, such as the esophagus,

stomach, and intestines, by administering contrast agents to highlight structures for procedures like barium studies or evaluating swallowing function. In interventional radiology, fluoroscopy guides minimally invasive procedures, such as angiography (visualizing blood vessels), catheter insertions, or placing medical devices within the body. In orthopedics, it assists in realigning fractures or guiding joint injections[16].

One of the distinctive features of fluoroscopy is its ability to provide real-time visualization, making it an invaluable tool during medical procedures. However, the use of continuous X-ray exposure during fluoroscopic imaging poses certain risks related to radiation exposure, particularly for patients and healthcare professionals. Efforts are constantly made to minimize radiation exposure during fluoroscopy by using the lowest possible dose while still maintaining image quality, employing modern equipment with dose-reduction features, and adhering to stringent safety protocols. The combination of real-time imaging and the continuous evolution of safety measures contributes to the ongoing usefulness of fluoroscopy in various medical settings[17].

2.1.4 Healthcare Efficiency and Safety Enhancement by Digital X-Ray Imaging Technology

Digital X-ray imaging represents a significant advancement in medical imaging technology. This method uses electronic sensors known as digital detectors to capture X-ray images instead of the traditional film used in conventional X-rays. The process begins with an X-ray machine emitting a controlled dose of radiation, and the electronic detectors immediately capture the transmitted X-rays. The captured information is then converted into digital signals, creating high-resolution images that are instantly available for viewing on a computer screen or digital monitor. This immediate availability allows healthcare providers to swiftly assess and diagnose conditions, significantly enhancing the efficiency of patient care[18].

The transition to digital X-ray technology has revolutionized the way medical images are handled. Digital X-rays offer immediate access to images without the need for film processing, as seen in traditional radiography. This eliminates the time-consuming chemical development process required in film-based X-rays. Moreover, these digital images can be effortlessly stored, transmitted, and retrieved electronically. The digital format permits the storage of images in electronic health records, facilitating easy sharing among healthcare providers and enabling seamless integration into patient medical records. This efficient workflow not only enhances diagnostic accuracy but also streamlines consultations and enables quicker decision-making in patient care[19].

The advantages of digital X-ray imaging extend beyond immediate accessibility. The digital format allows for the manipulation and enhancement of images to optimize diagnostic precision. Healthcare professionals have the ability to adjust image characteristics such as contrast and brightness digitally, improving image clarity and aiding in accurate diagnoses. Additionally, these digital images can be magnified or zoomed in for a closer examination, providing a detailed view of anatomical structures. This flexibility in image enhancement significantly contributes to the diagnostic capabilities of digital X-ray imaging and assists in determining the appropriate treatment plans for patients[20].

Furthermore, digital X-ray technology is associated with lower radiation doses compared to conventional X-ray methods. These systems often use optimized radiation doses to acquire images while maintaining or improving image quality. This reduction in radiation exposure aligns with the principle of minimizing potential risks for patients. The capability to acquire high-quality images with reduced radiation exposure is a critical aspect of ensuring patient safety in medical imaging practices[20].

However, digital X-ray imaging, while offering significant advantages in healthcare, does come with certain hazards and disadvantages. One primary concern is the potential for radiation exposure. Despite efforts to reduce radiation doses, X-ray imaging still involves ionizing radiation, and prolonged or repeated exposure can pose a risk of cellular damage and an increased risk of certain health issues, such as cancer.

2.2 Magnetic Resonance Imaging (MRI)

Magnetic Resonance Imaging (MRI) is an advanced medical imaging technique that uses a powerful magnetic field, radio waves, and a computer to generate detailed images of the body's internal structures. It provides a non-invasive, high-resolution view of soft tissues, organs, and bones, allowing healthcare professionals to diagnose and monitor a wide range of medical conditions. Unlike X-rays or CT scans, MRI does not use ionizing radiation, making it a safer option for repeated imaging studies[21].

The fundamental principle of MRI involves the interaction of hydrogen atoms in the body with a strong magnetic field. When a patient is placed inside the MRI machine, these hydrogen atoms align themselves in the magnetic field. Radio waves are then used to temporarily disrupt this alignment, causing the hydrogen atoms to emit signals. The MRI machine detects these signals and, with the help of a computer, generates cross-sectional images that display the distribution of hydrogen atoms in various tissues. These images provide detailed information about the body's anatomy, revealing different tissues' densities, composition, and physiological characteristics[21].

One of the key strengths of MRI lies in its ability to produce images with remarkable soft tissue contrast, offering clear views of organs, muscles, nerves, and other soft structures. It is particularly valuable in diagnosing and monitoring conditions such as brain and spinal cord disorders, musculoskeletal injuries, abdominal and pelvic conditions, cardiac issues, and various types of cancer. Additionally, MRI can show differences between healthy and diseased tissues, providing insights into the nature and extent of abnormalities[22].

MRI machines come in various configurations and are tailored for different purposes. High-field MRI machines offer exceptional image quality and are commonly found in hospitals and diagnostic centers. Open MRI machines, designed for patients who may feel uncomfortable in confined spaces, provide more space and a less confining environment. Functional MRI (fMRI) is a specialized MRI technique used to assess brain activity by detecting changes in blood flow, allowing researchers and medical professionals to map brain function and study neurological conditions[22].

Despite its numerous advantages, MRI does have limitations. Patients with certain medical implants or devices, such as pacemakers, cochlear implants, or metal clips, may not be eligible for an MRI due to safety concerns. Additionally, the procedure can be noisy and some patients may experience discomfort due to the confined space of the MRI scanner. Also, MRI examinations can be more time-consuming compared to other imaging techniques like X-rays or CT scans. Lastly, MRI represents an expensive approach for routine screening needs[22].

2.3 Positron Emission Tomography (PET)

Positron Emission Tomography (PET) is an advanced nuclear imaging technique used in medical diagnostics to produce three-dimensional images of the body's functional processes. Unlike other imaging modalities like CT or MRI, PET scans provide information about the body's metabolism, allowing for the detection and monitoring of diseases at a molecular level. This technique involves the use of a radioactive tracer—a biologically active substance labeled with a positron-emitting radionuclide—that is injected, inhaled, or swallowed by the patient. Once inside the body, the tracer emits positively charged particles called positrons. These positrons collide with electrons in the body, producing gamma rays that are detected by specialized cameras to create detailed images[23].

PET scans are particularly effective in visualizing metabolic activities within tissues. The radioactive tracer used in PET scans targets specific molecules or compounds within the body, such as glucose, water, or specific proteins. This allows physicians to observe the

activity of cells and tissues, detecting abnormalities in function much earlier than structural changes visible in other imaging techniques like X-rays or CT scans. PET is especially beneficial in oncology for cancer detection, staging, treatment planning, and monitoring treatment response, as cancer cells often have different metabolic activity compared to normal cells[23].

PET/CT scans combine PET and CT imaging, offering a comprehensive view of both structure and function. PET images showing metabolic activity are overlaid with CT images, providing more precise anatomical localization of abnormalities. This fusion of information enhances diagnostic accuracy and is particularly valuable in oncology, neurology, cardiology, and other areas where both structural and functional information is vital for accurate diagnosis and treatment planning[24].

While PET imaging offers exceptional insights into physiological processes, there are some limitations and considerations. One limitation is the cost associated with PET scans due to the need for specialized equipment, radiotracers, and trained personnel. Additionally, the radioactive tracers used have a short half-life, which means they decay quickly, limiting the time available for imaging after injection and necessitating an on-site cyclotron for tracer production. Furthermore, due to the use of radioactive materials, there are concerns about radiation exposure, although the doses used in PET scans are generally considered safe[24].

2.4 Ultrasound Imaging

Ultrasound imaging, also known as ultrasonography or sonography, is a medical diagnostic technique that employs high-frequency sound waves, typically between 2 to 18 megahertz, to create images of structures within the body. This non-invasive imaging method works by using a device called a transducer, which emits sound waves at frequencies higher than what the human ear can detect. These sound waves travel into the body and bounce off organs, tissues, and other structures. The transducer then receives the echoes of the sound waves and sends them to a computer that processes the information to generate real-time images displayed on a monitor[25].

Beamforming is a technique used in ultrasound imaging to generate a focused ultrasound beam capable of traversing tissue and producing an image. This beam can be steered either mechanically, using a single transducer element or an annular array, or electronically, by controlling an array of smaller transducer elements. In two-dimensional (2D) scanning, a common configuration employs a linear array consisting of 256 transducer elements. This

number is chosen as it offers a good balance between imaging resolution and hardware complexity, and is also efficient for digital processing systems. A typical beamforming setup uses an aperture composed of 16 adjacent elements. This aperture is incrementally shifted along the array one element at a time to capture the full image. Since the aperture is moved across the 256-element array with a step size of one, the total number of distinct beamforming positions is 241 lines (calculated as $256 - 16 + 1$). In this specific scanning scenario, each of these 241 aperture positions corresponds to a single line in the final image. Digital control is used to apply appropriate time delays for beam formation and to manage the apodization (tapering) of the aperture. To prevent aliasing, the system's sampling frequency must be at least twice the maximum ultrasonic frequency, as required by the Nyquist criterion. Enhanced imaging precision can be achieved by applying a finite impulse response (FIR) digital filter, or by converting the received radio-frequency (RF) signals to baseband using quadrature demodulation. This conversion enables fine phase rotation adjustments, improving the accuracy of time delay application and, ultimately, image quality [26].

The process involves applying a special gel on the skin to assist with the transmission of sound waves. The transducer is placed against the skin and moved over the area being examined. As the sound waves encounter tissues of varying densities, they produce echoes that are captured and converted into images. The resulting images help medical professionals visualize and evaluate the internal organs, blood flow, and abnormalities within the body.

Ultrasound imaging is widely used across various medical specialties and for different purposes. In obstetrics, it is commonly employed to monitor fetal development during pregnancy, assess the health of the fetus, and determine its position in the womb. In cardiology, ultrasound is used to examine the heart and its function, providing insights into conditions such as valve problems or heart defects. Additionally, it is used to examine the abdomen, pelvis, blood vessels, and other body parts, aiding in the detection and diagnosis of conditions like gallstones, kidney stones, tumors, and vascular issues[25].

There are different types of ultrasound imaging techniques. Doppler ultrasound, for example, is used to assess blood flow by detecting the movement of blood cells within vessels. This specialized form of ultrasound helps in evaluating conditions related to blood circulation, such as blood clots, arterial blockages, and aneurysms.

The benefits of ultrasound imaging include its safety, as it does not involve electromagnetic radiation, making it a preferred choice for various patients, including pregnant women. It is a real-time imaging technique, meaning that the images are produced instantly and can be observed immediately by healthcare professionals. As technology advances, the

quality of ultrasound images continues to improve, providing clearer and more detailed visuals for better diagnostics and treatment planning[27].

Ultrasonic Process Tomography (UPT) utilizes ultrasound's multiple transmission features in a medium, resembling radiation tomography in directional propagation at higher frequencies. However, ultrasound waves exhibit complex behaviors at the interface of different acoustic impedance media, including reflections, transmissions, refractions, and Doppler effects, making it a versatile multi-mode tomography. UPT offers non-hazardous, non-intrusive, clamp-on usability, making it ideal for industrial process monitoring. It encompasses ultrasonic transmission tomography (UTT) and ultrasonic reflection tomography (URT) (seen in Fig. 2.1). UPT collects time-of-flight (TOF) and sound attenuation data along various ray paths to reconstruct acoustic property distributions. URT locates boundaries and reconstructs inclusion shapes using reflected ultrasound waves due to acoustic impedance differences. Enhancing the number of transducers in UPT improves projection data but lowers data sampling rates due to slower ultrasound propagation in fluids. The typical number of transducers is around 16 to 32, and fan-beam transducers help increase receiving transducers under each excitation. UTT excels near boundaries, while URT offers superior reconstruction in central areas. A dual-mode UPT combining UTT and URT through a single array of ultrasonic transducers has emerged, collecting ultrasound attenuation and TOF data from all transducers, showing potential for high-speed industrial multiphase flow imaging [28].

Ultrasound imaging, while widely used and valuable in medicine, has limitations. It faces challenges in penetrating bone and air-filled structures, leading to poor visualization in these areas, as well as difficulties in imaging obese patients or those with substantial scar tissue. Additionally, it relies on operator skill, may not provide detailed bone images, and can be hindered by the presence of gas or air, limiting its diagnostic scope. Ultrasound might not detect certain abnormalities and does not always offer a comprehensive assessment, potentially necessitating further imaging modalities for a complete diagnosis[27].

2.5 Microwave Imaging

Challenges and constraints in the traditional clinical detection methods have inspired researchers to explore and create novel imaging approaches utilizing microwaves[29, 30]. The idea of employing microwaves for detecting cancerous tumors gained considerable interest and thorough exploration from multiple research groups due to their various benefits. These advantages encompass lower costs, utilizing non-hazardous radiation, and enhanced

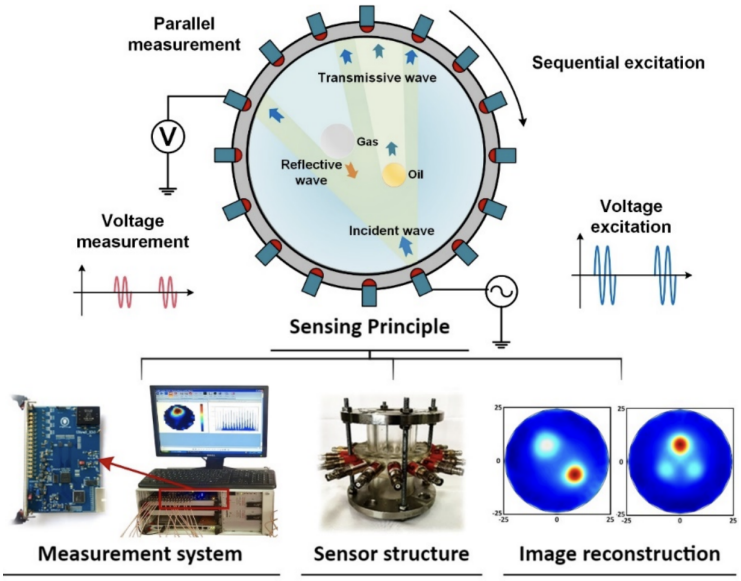


Figure 2.1: Sensing principle of UPT and image reconstruction of inclusions with different acoustic impedance [27].

Table 2.1: Comparison between traditional cancer detection techniques

X-ray	MRI	Ultrasound	PET
Ionizing radiation	Non-ionizing radiation	Non-ionizing radiation	Ionizing radiation
Inexpensive	Very expensive	Inexpensive	Relatively expensive
Acceptable accuracy	Very reliable	Operator-based	Reliable
Easy-to-use	Not user-friendly	Easy-to-use	Complex operation

user-friendliness when compared to existing techniques, as detailed in Table 2.1. Furthermore, microwave imaging (MI) offers improved sensitivity and the capacity to identify small tumors by leveraging the contrast in electrical properties between healthy and tumorous tissues[31, 32].

Microwave-based methods for detecting body tissues capitalize on differences in electrical properties between healthy and tumor-affected tissues. These techniques explore three

categories—passive, hybrid, and active methods.

The passive approach involves using a radiometry device to detect temperature differences between healthy and malignant body tissues, with tumorous tissues displaying higher temperatures due to distinct electrical properties[33]. Hybrid techniques, known as thermoacoustic methods, use microwave sensors and ultrasound transducers to identify tumors. Microwaves are absorbed by body tissues, with malignant tissues absorbing more energy and emitting stronger acoustic waves due to higher electrical conductivity. Ultrasound transducers capture these waves for image reconstruction[34]. Active Microwave Imaging (MI) utilizes microwave signals to illuminate body tissues and measure dielectric property differences within a specific frequency range. By assessing the back-scattered signals, this technique reconstructs an image, highlighting tumors with stronger reflected signals compared to healthy tissues[35].

Active microwave methods for body cancer imaging encompass various techniques, notably tomography and radar-based methods [36]. Tomography typically involves solving a nonlinear inverse problem through iterative reconstruction algorithms, requiring substantial computational resources to estimate the spatial distribution of dielectric properties within the body. These methods utilize inverse scattering techniques to analyze both absorbed and reflected microwave signals, thereby reconstructing detailed tissue structures from the measured data [37].

In contrast, radar-based approaches use an external microwave source to emit ultra-wideband (UWB) signals that illuminate the body. The back-scattered signals are then analyzed to detect and localize anomalies, such as tumors [38, 39]. Unlike tomography, radar-based imaging does not attempt to reconstruct full dielectric maps and is typically favored for its lower computational demands and faster processing, making it suitable for real-time detection applications.

2.5.1 Microwave Tomographic Imaging

Microwave tomography (MT) uses microwave signals to scan body tissue, aiming to create a detailed profile of the body's permittivity and conductivity. This method focuses on quantitatively reconstructing the dielectric properties of the imaged region. It typically involves solving a challenging nonlinear inverse scattering problem by estimating the scattered fields and comparing them with signals acquired from a known or healthy reference model [37].

While MT and radar-based methods both follow a general process of data acquisition, analysis, and image presentation, the primary difference lies in their goals and method-

ologies. MT seeks to reconstruct high-resolution maps of dielectric properties using full-wave inversion, whereas radar-based imaging typically focuses on detecting and localizing anomalies using backscattered signal analysis.

The MT imaging process consists of three main stages: data collection through microwave scanning, data analysis, and image display. In the data collection phase, body tissue is exposed to a microwave signal, and the resulting interactions are stored in tomographic data files. The analysis phase involves applying inverse scattering algorithms to retrieve the dielectric properties of both healthy and tumorous tissues from this data. In the final stage, the computed information is visualized as 2D or 3D tomographic images that indicate the presence, position, and size of tumors [40].

An MT-based cancer detection system consists of both hardware and software components. The hardware includes microwave sensors and probes, while the software implements advanced image reconstruction algorithms.

In microwave tomography (MT) for body tumor imaging, reconstruction methods play a crucial role in generating images. Within the literature, two distinct approaches have been utilized to address the nonlinear inverse problems in MT for body imaging: the gradient-based local methods and the global methods. Both are employed to reconstruct images of body tumors through MT[41, 42].Both the gradient-based local methods and the global methods in microwave tomography (MT) formulate the MT problem as a cost function. This function is then resolved through an iterative process in both techniques.

In the methodology employing local gradient-based techniques, the resolution of nonlinear inverse problems involves the utilization of specific data-processing algorithms intended for the detection of cancers within the body. These algorithms include the conjugate gradient least squares (CGLS) algorithm, the least squares QR (LSQR) algorithm, and the Landweber algorithm. The distinct advantage of using these gradient-based algorithms lies in their efficiency, as they require fewer iterations, thereby resulting in reduced processing times during the image reconstruction process for cancer detection within the body[43]. The global method in microwave tomography operates by utilizing randomization to explore various local minima distributed across the entire solution space. Unlike the local gradient-based approach that confines its search to the gradient direction, this method ventures through different areas to identify the global minimum of a cost function. It employs evolutionary algorithms like the genetic algorithm (GA) and particle-swarm optimization (PSO) algorithm[44, 45]. Within the realm of microwave tomography imaging, multiple innovative image reconstruction algorithms have been developed and applied. These algorithms are specifically designed to tackle the intricate, ill-posed nonlinear problems associated with the detection of body cancer, employing diverse methodologies to enhance

the efficiency of cancer detection through microwave tomography.

In this particular section, an analysis is conducted on some of the most renowned tomography MI systems within the literature. The examination takes into account various factors that significantly impact the performance and functionality of each system. These encompass the operational frequency, antenna type, the sophistication of the data acquisition system in terms of the number of channels, the array configuration, the time required for scanning during examination, the coupling medium utilized, the quantity and nature of clinical trials conducted, the specific algorithms employed for the reconstruction of both 2D and 3D tomographic images, and notably, the remarkable ability of these systems to detect even the minutest tumors.

The evaluation of these features is critical as it allows for a comprehensive assessment of each system's efficiency, accuracy, intricacy, and overall ease of use. By examining these varied facets, it becomes possible to gauge and compare the overall performance of these MI systems, shedding light on their individual strengths and limitations within the domain of tumor detection and imaging through microwave technology.

The pioneering near-field tomography MI system for breast cancer detection, as reported in [36], featured a 32-channel data acquisition subsystem with a heterodyning modulation scheme, a 200 kHz A/D board, and signal phase and amplitude extraction. It employed a cylindrical array of 16 transceiving monopole antennas within the 300–1000 MHz frequency range, along with an HP85070B dielectric probe kit and an HP 8753C network analyzer. All components were integrated into a portable cart. During examination, saline served as the coupling medium between the breast and the antenna array. The setup required the patient to lie down on a bed and place the breast into the MI bath underneath, as shown in Fig. 2.2. This system was used in clinical exams involving five women, with scan times of 10 to 15 minutes per breast. The resulting images (Fig. 2.3 and Fig. 2.4) show the recovered 900 MHz relative permittivity and conductivity images for both left and right breasts of Patient 1, providing visual insights into the examination outcomes.

While the presented prototype demonstrates a promising approach to microwave breast imaging, several limitations temper its immediate clinical applicability. The study is based on a very small sample size of only five participants, which limits the generalizability of the findings and raises questions about the robustness and reproducibility of the results. Additionally, the reconstruction methodology, although innovative, is still in the preliminary stage, and the spatial resolution (1 cm) may not be sufficient to reliably detect small lesions typically encountered in clinical settings. The higher-than-expected permittivity values also suggest variability that could complicate diagnosis. Furthermore, the reliance

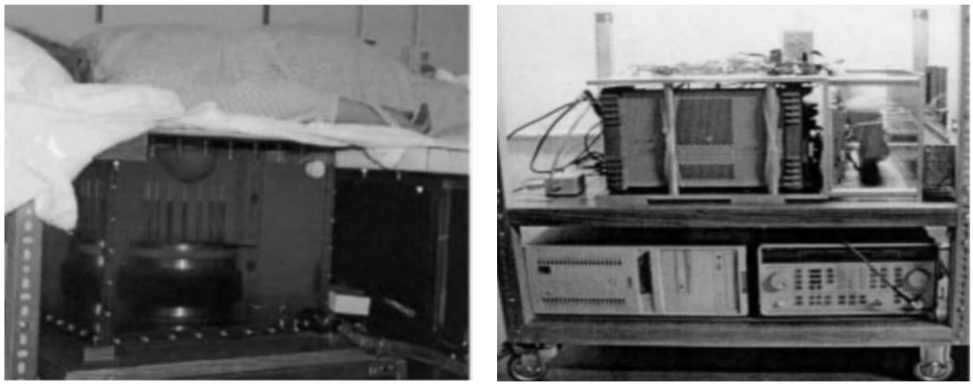


Figure 2.2: Displaying the imaging system prototype devised by Meaney et al.: (a) Depiction of the examination table. (b) Illustration of the data acquisition system with the microwave source [36].

on water coupling and the prone positioning, while practical in the experimental setting, may pose logistical challenges and patient comfort issues in real-world applications. Overall, significant further validation, larger clinical trials, and refinement of imaging techniques are necessary before microwave imaging can be considered a reliable adjunct or alternative to established modalities like mammography.

The same research group introduced the first 3D prototype tomography MI system based on the 3D finite element modeling (FEM) method for microwave tomography [46]. Overcoming limitations in both hardware and software, the system employed a 16-antenna array and hydraulic seals in the tank base, allowing unrestricted vertical antenna movement for comprehensive data acquisition. The setup is shown in Fig. 2.5.

It achieved sub-centimeter image resolution, maintaining examination times below two minutes and processing durations under 20 minutes. The system harmonized hardware and software for near real-time imaging without compromising accuracy. Dividing antennas into two sets of eight, controlled by separate motors, enabled precise vertical positioning. Clinical trials demonstrated the system's capability by successfully detecting a 1.5 cm $\times$ 1.2 cm $\times$ 1 cm tumor in the right breast of a 55-year-old patient, as shown in Fig. 2.6 [46].

The clinical trial presented in the paper is preliminary, involving only a few cases—two examples out of over 400 exams conducted at the Dartmouth Hitchcock Medical Center. Although the results are promising, demonstrating the system's potential for screening and therapy monitoring, the limited sample size restricts the ability to draw definitive

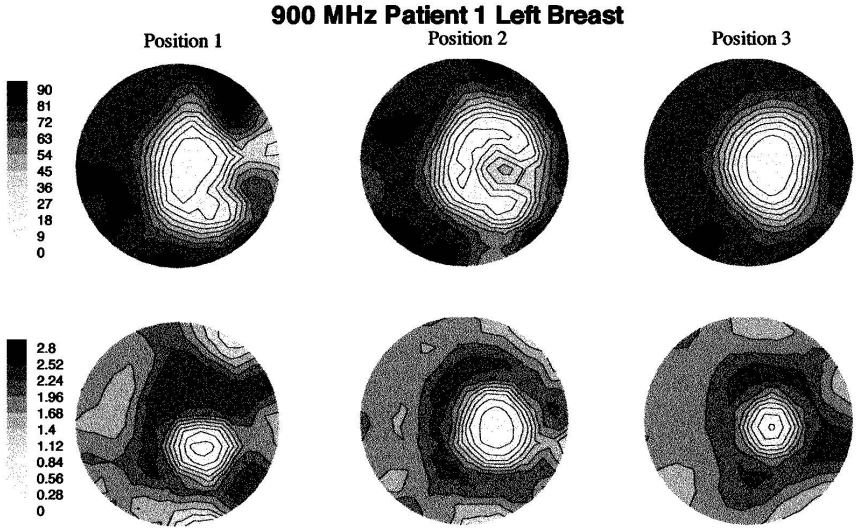


Figure 2.3: The retrieved 900 MHz relative permittivity and conductivity images from Patient 1 for the left breast [36].

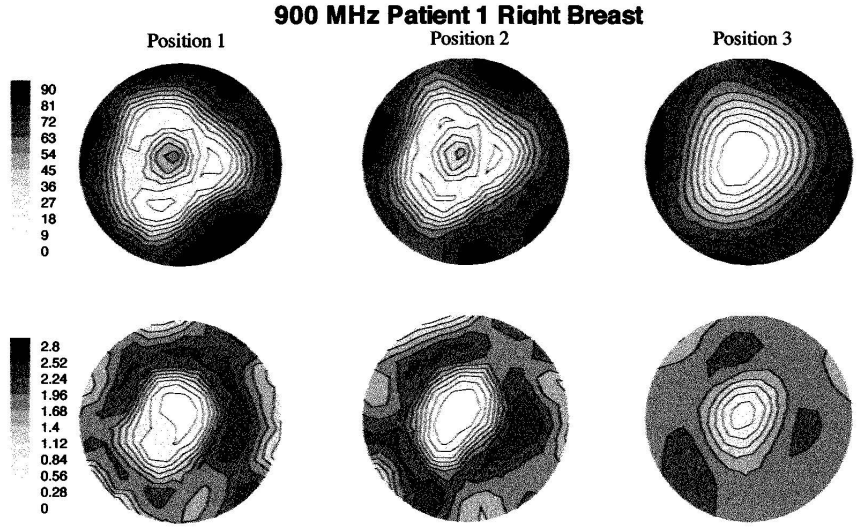


Figure 2.4: The retrieved 900 MHz relative permittivity and conductivity images from Patient 1 for the right breast [36].

conclusions regarding the system's diagnostic accuracy, sensitivity, and specificity across a broader patient population. The early-stage nature of these trials implies that further

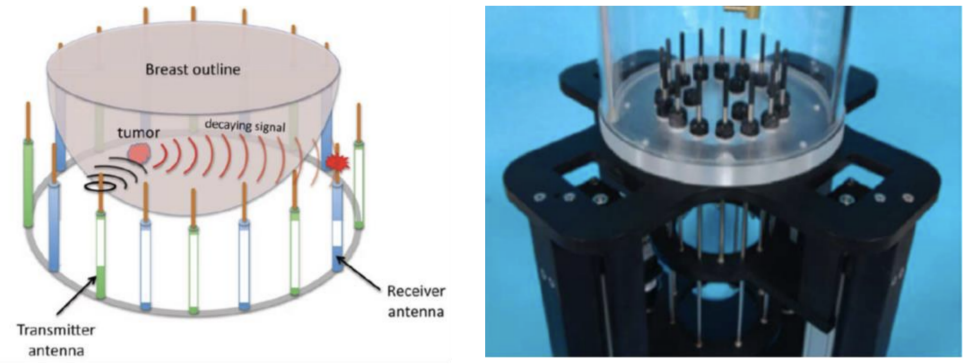


Figure 2.5: Grzegorczyk et al.'s breast cancer testing prototype system: (a) Exhibits a 3D schematic of the testing setup. (b) Displays a photograph of the system's hardware [46].

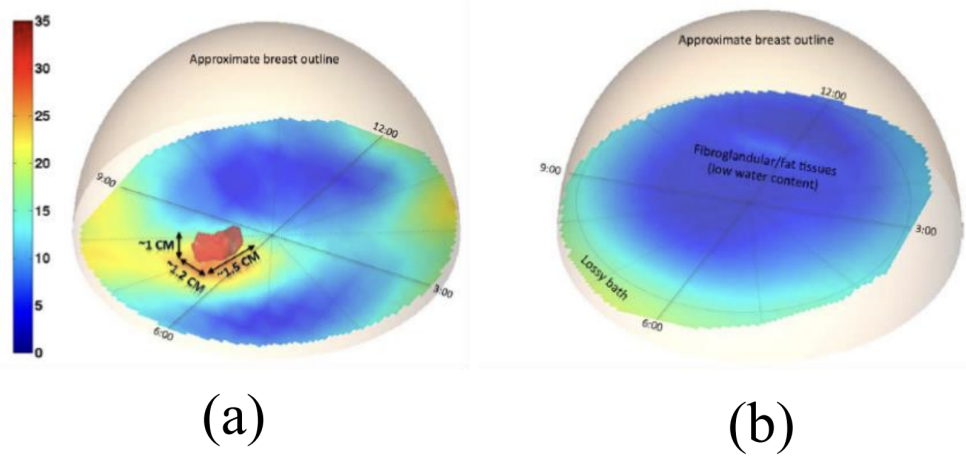


Figure 2.6: 3D microwave tomographic permittivity images at 1300 MHz from Grzegorczyk et al.'s system: (a) Shows the tumor in the right breast. (b) Depicts the tumor-free left breast [46].

extensive validation with larger, more diverse cohorts is necessary to establish clinical efficacy and reliability before it can be considered a proven diagnostic tool.

Furthermore, although the authors emphasize computational speed and 3D capability, the imaging results were not validated against actual clinical data or in vivo human tissue. The absence of comparisons with standard imaging modalities (e.g., mammography, ultrasound, MRI) also limits the ability to assess the system's diagnostic accuracy. Additionally, the tumor size (1 cm) and high contrast used in the phantom experiments may not reflect challenging clinical scenarios involving small or low-contrast lesions. While the system shows promise in preclinical settings, further evaluation under realistic anatomical and pathological conditions is essential before clinical applicability can be confirmed.

A preclinical prototype MT system for breast cancer detection was developed by Son et al., as depicted in Fig. 2.7 (a) [47]. In this system, a 16-element circular array was placed into an imaging bath containing a matching liquid. Each antenna was used for signal transmission and reception across a frequency band ranging from 500 MHz to 3000 MHz. A matching liquid was utilized to fill the imaging bath in order to reduce reflections from the breast surface, as shown in Fig. 2.7 (b). The total number of transmit-receive data points amounted to 240 (measurements were carried out for each frequency at each imaging plane). The data acquisition unit used a programmable switch matrix, as demonstrated in Fig. 2.8 [47].

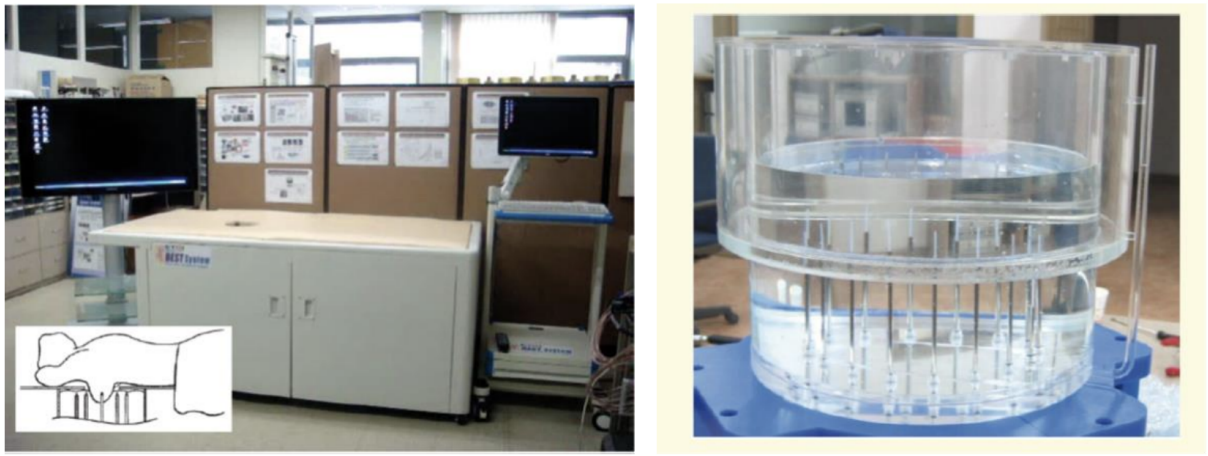


Figure 2.7: (a) Illustrates the entire system, and (b) specifically presents the breast holder featuring the antenna array immersed in a liquid bath [47].

The 2D tomography system suggested in [47] is suitable for testing both on patients and on models. The described initial system effectively identified a 10 mm tumor within

a model. Figure. 2.9 depicts the reconstructed images of a breast model with a cylindrical 10 mm tumor at 1700 MHz. It showcases images of the breast model without a tumor, with a tumor placed at the breast's center, and with a tumor positioned 30.0 mm to the right of the center.

The study [47] presents the development of a preclinical 3-D microwave tomography (MT) system aimed at breast imaging. A notable strength of the work lies in the engineering effort toward modular hardware design, automation of vertical scanning, and flexible acquisition using a circular 16-antenna array immersed in a matching fluid. The system is designed to scan multiple horizontal planes for full 3-D dielectric reconstruction, showing progress toward clinical readiness. However, the study remains limited in its evaluation. The imaging experiments are confined to a series of phantom tests, with no in vivo or clinical data provided. The phantoms, although anatomically inspired, include idealized tumor shapes and homogeneous backgrounds, which do not fully represent the structural and dielectric heterogeneity of real breast tissue. Additionally, the reconstructions are primarily presented at a single frequency (1300 MHz), despite the system's broadband capability. The paper does not quantify performance metrics such as spatial resolution, sensitivity, or specificity, nor does it benchmark the system against other modalities. While the imaging results demonstrate localization of inclusions and a functioning 3-D imaging pipeline, the lack of clinical validation or comparison with radiological ground truth limits the ability to assess the true diagnostic value of the system. Further work involving anatomically realistic, heterogeneous phantoms and eventual transition to patient trials is essential to demonstrate clinical efficacy.

2.5.2 Radar-Based Microwave Imaging

Radar-based methods utilize an external microwave source to illuminate breast tissue using ultra-wideband (UWB) signals. These signals, when scattered back from the breast, aid in the detection of breast tumors. The initial radar-based medical imaging (MI) system was introduced by Bridges et al. in 1997, aiming to create breast images without relying on complex nonlinear inverse scattering algorithms to fully capture the breast's dielectric properties [41, 48]. This method employed a wide microwave signal emitted by an antenna array positioned around the breast to illuminate its tissues [41]. Subsequently, the same antennas received the back-scattered microwave signals, which were then processed using radar-based MI techniques to identify the location and size of tumors. The contrast in dielectric properties between normal and tumorous tissues at microwave frequencies was used to detect the presence of tumors in these back-scattered signals. Radar-based MI involves radar-based methods and beam-forming algorithms. While radar-based methods define the

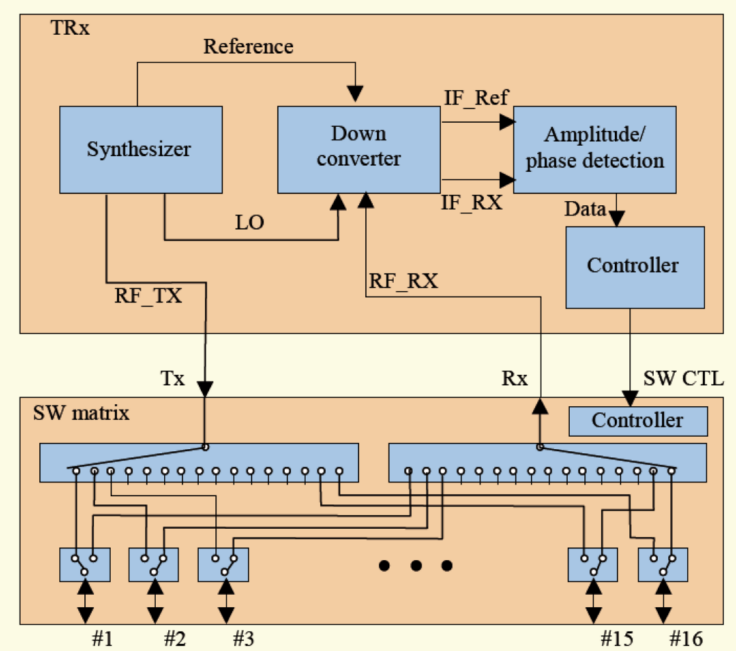


Figure 2.8: Diagram of the system devised by Son et al [47].

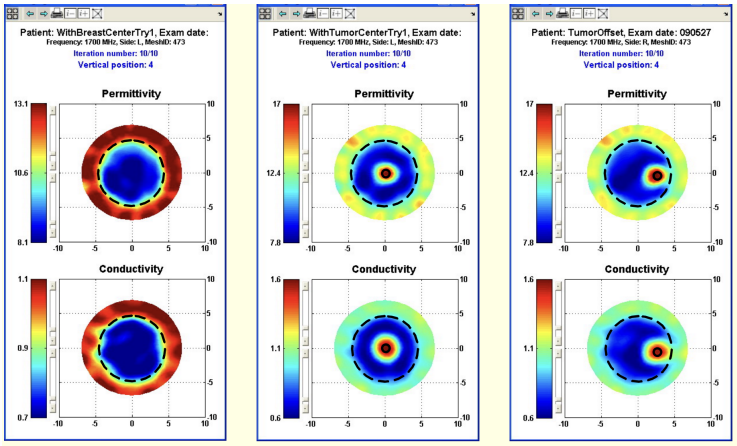


Figure 2.9: Images of a breast model with a 10 mm cylindrical tumor at 1,700 MHz: (a) without a tumor, (b) tumor at the center, and (c) tumor 30 mm right of center. Circles mark actual breast and tumor boundaries [47].

overall imaging approach using back-scattered signals, beam-forming refers specifically to the signal processing techniques used to spatially focus or interpret those signals. These methods encompass various radar setups utilizing elements of an antenna array to transmit or receive microwave signals into or from the breast. Beam-forming algorithms are crucial for reconstructing images from the reflected signals. Here, we will explore a selection of proposed methods and techniques outlined in the literature.

A breast cancer detection system named the Three-Dimensional Ultra-Wideband Tissue Sensing Adaptive Radar (TSAR) was introduced by Fear et al. in a passive configuration. This system involved the use of a patient interface that utilized a cushioned table with an opening through which the breast was lowered into a cylindrical container, as displayed in Fig. 2.10 and Fig. 2.11. The data collection process employed a mono-static technique, and a filtering circuit was integrated to diminish reflections from the skin tissues. The system underwent testing on eight volunteers ranging in age from 32 to 47 years [49]. Notably, the system demonstrated successful detection of breast tumors as small as 5 millimeters in diameter, as illustrated in Fig. 2.12.

In Fig. 2.12, the tumor is located in the lower-left quadrant of the radar-based image. This corresponds to the dominant response with the highest signal-to-clutter ratio (SCR) of 5.43 dB. Clinically, the malignant lesion was identified via mammography at the 4 o'clock position of the right breast and by MRI at 5 o'clock, with post-surgical pathology confirming it as a grade II/III metaplastic carcinoma. Given the imaging orientation (transverse slice, viewed from the top), the lower-left region of the image spatially corresponds to the 4–5 o'clock region of the right breast. Therefore, the bright localized feature in that quadrant of the radar image is consistent with the confirmed tumor site. Additional responses observed near 7 o'clock and 11 o'clock (with SCRs of 3.97 dB and 3.93 dB, respectively) correspond to a suspected benign lesion and glandular tissue, respectively.

An experimental multi-static radar-based time-domain Medical Imaging (MI) system for breast cancer detection was introduced by Porter et al., as illustrated in Fig. 2.13 [50]. The system comprised a radome, serving as the interface between the system and the positioned breast, a 16-element antenna array, a commercial pulse generator, an oscilloscope, a switch matrix, and a computer (Fig. 2.14). Time-domain measurements were utilized by the system. A proof-of-concept involved demonstrating the imaging of breast tumors within realistically-shaped breast phantoms. As depicted in Fig. 2.15 [50], the system successfully identified a spherical tumor with a radius of less than 1 cm inserted into a realistically-shaped breast phantom.

Radar-based MI techniques encompass five different approaches: confocal microwave (CM), tissue sensing adaptive radar (TSAR), MI via space-time (MIST), multi-static adap-



Figure 2.10: The TSAR prototype, a radar-driven Medical Imaging (MI) system designed by Fear et al., is engineered for detecting breast cancer through tissue sensing [49].

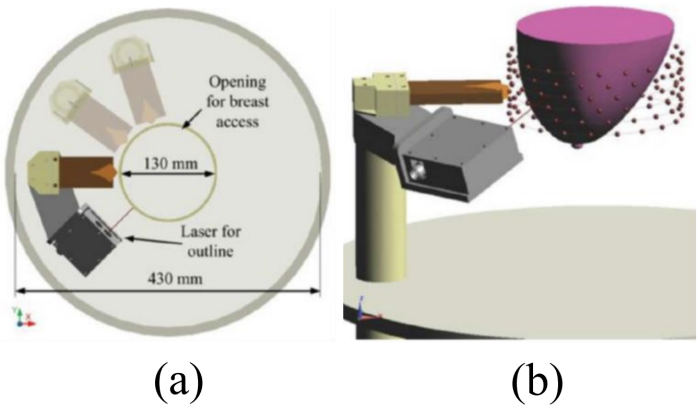


Figure 2.11: (a) Depicts an aerial view of the antenna and laser setup. (b) Presents the breast holder assembly, featuring a tank, laser, and antennas [49].

tive (MSA), and time-domain data adaptive (TDDA). The beam-forming algorithms used for breast tumor detection can be categorized into various imaging algorithms. These include delay and sum logarithm (DAS), time reversal (TR), artefact removal (AR), time-of-arrival (TOA), skin subtraction (SSA), inverse scattering (ISA), Gauss–Newton iterative (GNIA), matched-filtering (MFA), generalized likelihood ratio test (GLRT), con-

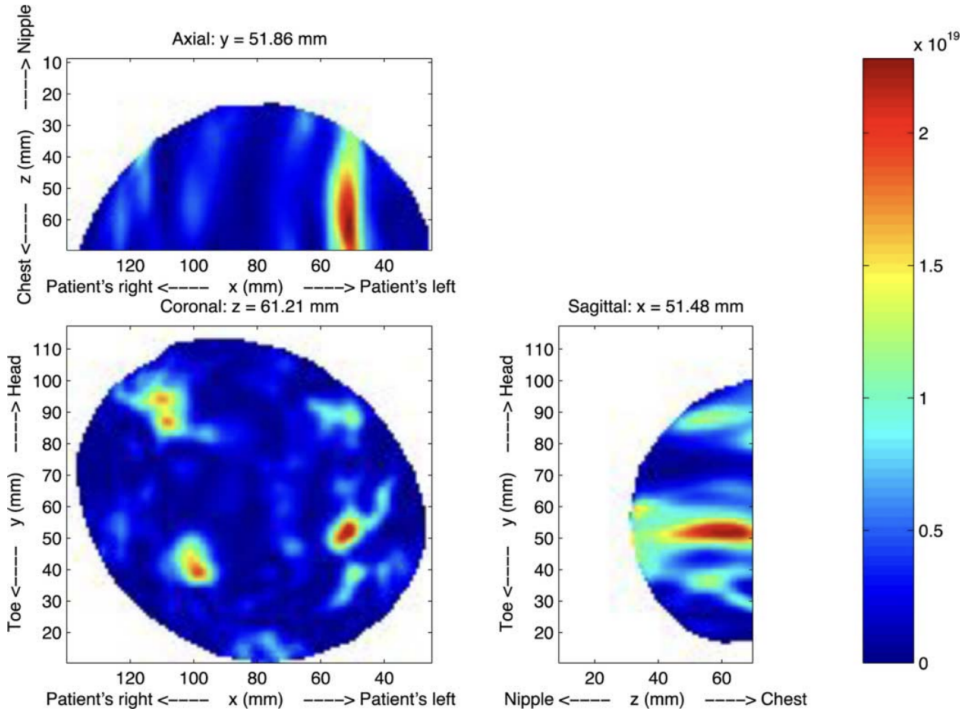


Figure 2.12: Images reconstructed by the TSAR system developed by Fear et al [49].

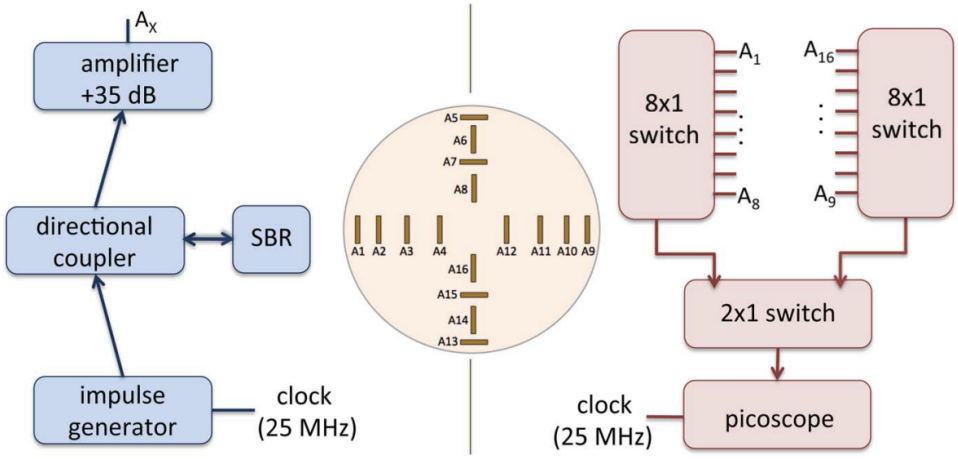


Figure 2.13: System configuration developed by Porter et al [50].

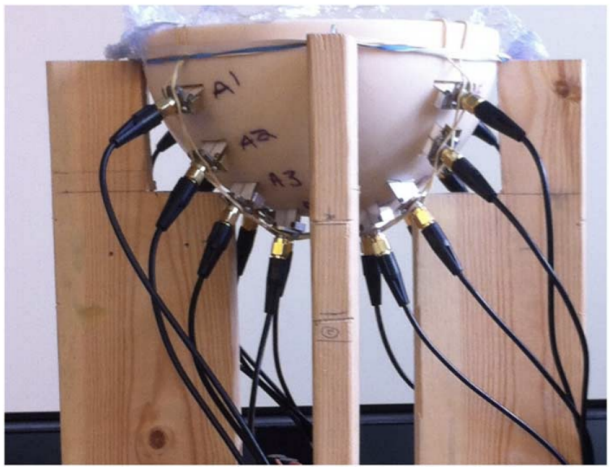


Figure 2.14: A breast cancer detection system utilizing an antenna array equipped with a radome [50].

strained robust Capon (CRC), inverse fast Fourier transform (IFFT), local discriminant basis (LDB), forward-backward time-stepping (FBTS), time-shift-and-add (TSAA), linear constraint minimum variance (LCMV), genetic algorithm (GA), filtered delay-and-sum (FDAS), skin reflection removal (SRR), double constrained robust Capon beamforming (DCRCB), norm constrained Capon beamforming (NCCB), empirical mode decomposition (EMD), modified delay-and-sum (MDAS), delay-multiply-and-sum (DMAS), and robust and artefact resistant (RAR). The table. 2.3 presents a comparative analysis of the suggested techniques.

Recent advancements in radar-based microwave imaging have significantly challenged the traditional classification of radar techniques as solely qualitative. Historically, radar-based or direct-inversion techniques were distinguished from tomographic approaches by their lower spatial resolution and limited capacity to quantitatively reconstruct dielectric properties of biological tissues. However, this distinction has become increasingly outdated with the emergence of innovative real-time imaging methods that combine computational efficiency with quantitative capability.

Specifically, two direct inversion approaches—quantitative microwave holography and scattered power mapping—have demonstrated the ability to quantitatively image dielectric profiles in near-field biomedical scenarios without the need for iterative solvers or forward simulations. Tajik et al. (2018) showcased real-time quantitative imaging of compressed breast phantoms using planar scanning in under two seconds, providing clear dielectric contrast reconstructions that support diagnostic inference in clinical contexts [51]. In sub-

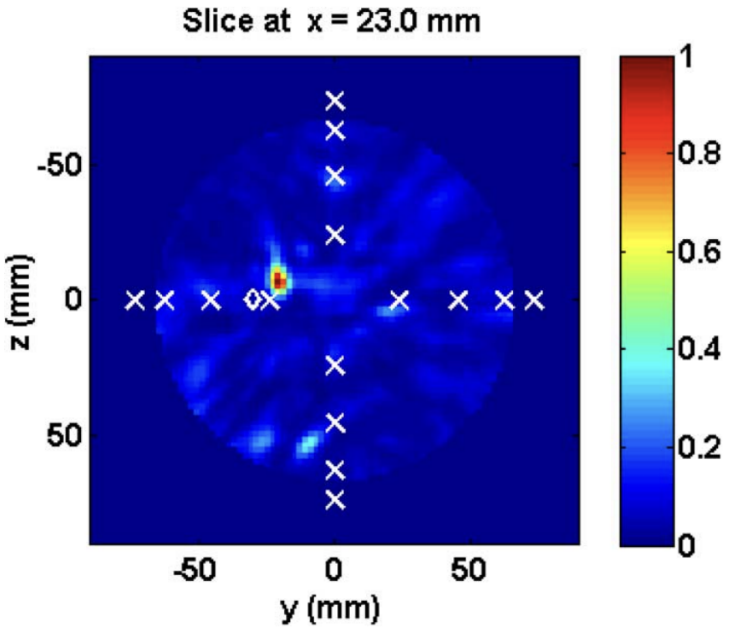


Figure 2.15: Image reconstruction from the breast phantom detection system developed by Porter et al. The tumor is highlighted by a red spot; the "x" markers indicate antenna positions, while the diamond markers represent the actual tumor center locations [50].

sequent studies, simultaneous application of both Born and Rytov approximations further enhanced the robustness and accuracy of quantitative holography, demonstrating superior image fidelity while maintaining real-time performance [52]. This hybrid approximation approach allows improved modeling of electromagnetic scattering in complex tissues while preserving the speed necessary for clinical viability.

Complementary to holography, the technique of scattered power mapping has also enabled non-iterative quantitative reconstructions. Kazemivala et al. (2022) demonstrated that Fourier-space mapping of scattered power distributions can accurately recover both location and dielectric strength of inclusions within breast-like media [53]. More recently, a synthetic aperture radar (SAR) framework incorporating random spatial sampling with power mapping has shown promise for low-complexity, real-time imaging applications, further extending the domain of quantitative radar-based microwave imaging to dynamic and sparse acquisition setups [54].

These developments firmly establish that modern radar-based techniques are no longer limited to qualitative image generation. They can provide fast, reliable, and quantitatively

meaningful images suitable for biomedical diagnostics, particularly breast cancer detection. As such, the earlier classification of radar methods as inherently qualitative must be revised in light of this growing body of work, which demonstrates that direct inversion techniques can now offer performance comparable to or complementing that of more computationally intensive tomographic approaches.

2.6 New modalities in Microwave Imaging

2.6.1 Low-frequency Computerized Tomography

The article [55] presents a novel imaging method that employs highly localized radiators or small antennas to create images using frequencies near the lower range of the microwave spectrum. The technique operates on the idea that if the size of the "OUT" (electrically small element) is significantly smaller than the wavelength of the radiating source, the impression created by a localized source impacting the "OUT" will closely resemble an impression generated by a ray-like source. Essentially, the receiver closest to the source will primarily capture information about the object along the direct path between the transmitter and the receiver. This means the interaction of microwaves with the examined medium is akin to the way X-rays interact with a medium, leaving an impression on the receiver directly dependent on the tissues in the path traversed by the X-rays between the source and a point on the receiver. This unique field behavior is crucial to the method, allowing the reconstruction approach to mirror the principles used in computerized tomography (CT), employing the Radon transform and X-ray illumination [44], [45]. Simulation and experimental results are provided to confirm this behavior of the fields. The focus of our proposed method lies in reconstructing the shape of the "OUT" and particularly the contrast within its interior, therefore being categorized as a qualitative approach. Throughout this work, only the magnitude of transmission coefficients is utilized.

Figure. 2.16 depicts the scanning arrangement, comprising the transmitter, receiver, OUT, two 50-Ω cables, positioner, and the vector network analyzer. Both the transmitter and receiver are aligned along the z-axis.

In Fig. 2.17 (a), a cylindrical structure consisting of two Plexiglas shells is shown. The outer shell has an outer radius of 1.6 cm and an inner radius of 1.4 cm, while the inner shell has an outer radius of 0.95 cm and an inner radius of 0.85 cm. The region between these shells is filled with a mix of sand and water, containing 20% volumetric moisture (mv), while the space inside the inner shell is air. Positioned in the scanning setup, the transmitter and receiver remain fixed at a distance of 1 mm away from the cylinder.

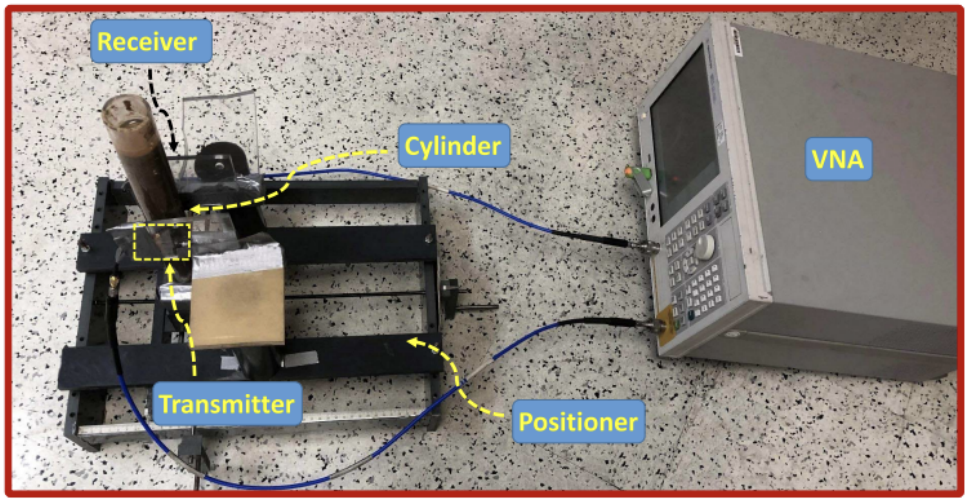


Figure 2.16: Configured setup for analyzing the OUT as illustrated in Figure 15: featuring the transmitter, receiver, OUT, 50 Ω - cables, positioner, and vector network analyzer [55].

The scanning of the OUT ranges from -5 to 5 cm, producing the $|S21|$ profile illustrated in Fig. 2.17 (b). The projection profile demonstrates a relatively consistent value up to -2.2 cm, indicating the absence of objects detected between the transmitter and the receiver. At approximately -2.1 cm, a distinct change is observed, signaling the transition from the outer shell to the sand-water medium, which exhibits absorptive properties, causing energy absorption. Another significant change occurs at -1.9 cm, representing the shift from the sand-water medium to the inner Plexiglas shell. Finally, a notable increase is observed from -0.5 cm to 0 cm, signifying the shift from the inner Plexiglas to the air medium.

In Fig. 2.18, the reconstructed image displays significant changes highlighted with red circles. These distinctions signify the boundaries marking transitions from air to Plexiglas, Plexiglas to sand-water, sand-water to Plexiglas, and Plexiglas to the inner area containing air. Notably, these substantial alterations occur around the radius of the shells, demonstrating the antennas' capacity to detect extremely minute changes, smaller than $\lambda/50$, occurring within the cylinder. This observation provides evidence supporting the ray-like behavior of fields generated by the electrically small radiator.

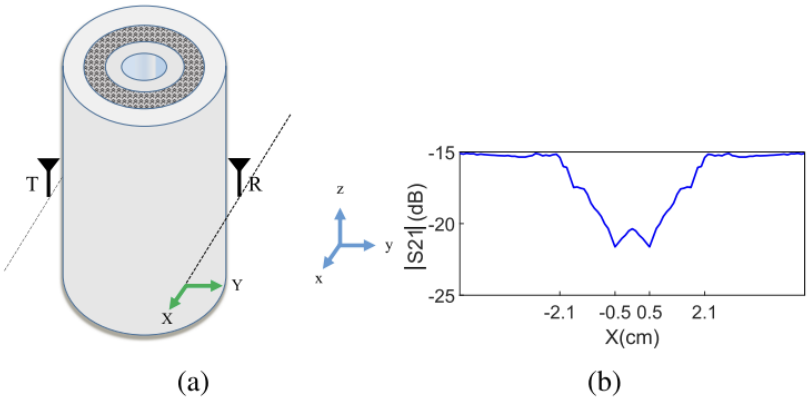


Figure 2.17: Analysis of a four-layer cylinder and its projection profiles: (a) placement between transmitter and receiver. (b) receiver's collection of magnitude transmission coefficient profile, $|S21|$, relative to location [55].

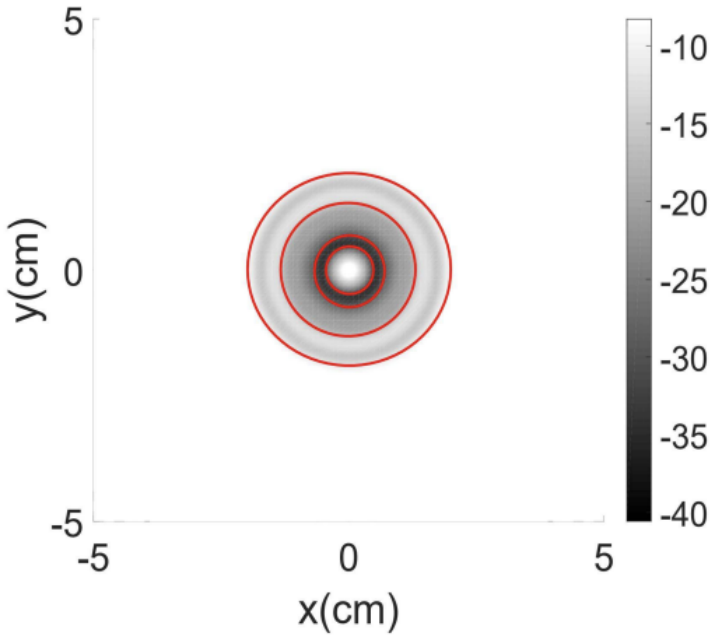


Figure 2.18: Reconstructed image of one slice of the OUT shown in Fig. 2.17 (a) [55].

2.6.2 Microwave Film

In [2], a microwave-based system is introduced for the detection of breast tumors. Unlike previous MWI techniques or general imaging methods that provide an image of the breast's internal tissue (i.e., a slice or cut through the breast), the technique proposed in [2] provides an impression of the breast tissue. This impression, similar in principle to the impression captured by an X-ray film, is recorded by a metasurface, which consists of an ensemble of electrically small resonators. The strength of the incident power impacting each cell is recorded by the metasurface.

The metasurface may be seen as analogous to a low-frequency scaling of the X-ray film. It receives the transmitted energy through the breast, resembling the approach of mammography. While mammography encounters challenges in detecting tumors in dense breasts, the proposed metasurface utilizes a low-frequency radiation source, allowing for higher penetration through dense breast tissue. The detection capability is then enhanced by the involvement of a convolution neural network (CNN) to characterize the tumor's location and size.

The Electric-LC (ELC) cell is positioned on top of a 3.175-mm-thick Rogers TMM10i dielectric substrate, characterized by a dielectric constant (ϵr) of 9.8 and a loss tangent (tan δ) of 0.002, as depicted in Fig. 2.19 (a). The choice of substrate aimed to minimize dielectric loss in the absorbed electromagnetic power within the unit cell, thereby ensuring maximum energy absorption within the resistive load of the unit cell. To prevent interference with objects situated beneath the surface, the substrate is backed by a metallic plane.

The design and optimization of the ELC aimed for resonance at 1.9 GHz, resulting in specific dimensions for the ELC: L = 10 mm, W1 = 1.4 mm, W2 = 0.6 mm, g = 0.5 mm, s1 = 0.5 mm, s2 = 1 mm, and a thickness (t) of 3.175 mm, with a copper thickness of t = 35 μm, as shown in Fig. 2.19 (a). It is important to note that the selection of this frequency was not due to empirical-based optimization but rather aligned with the aforementioned considerations. The inherent narrowband nature of electrically small resonators, like the ELC unit cell used here, underscores the significance of illuminating the field with a narrowband signal.

The determined optimal resistance value of 100 ohms matched the impedance of the ELC observed from the load. Consequently, each unit cell was terminated by a 100-ohm resistance, resulting in maximum power dissipation across the terminated load at 1.9 GHz, illustrated in Fig. 2.19 (b).

During plane wave radiation, a uniform surface current distribution was observed across the metasurface at the resonance frequency, as depicted in Fig. 2.19 (c). However, due to

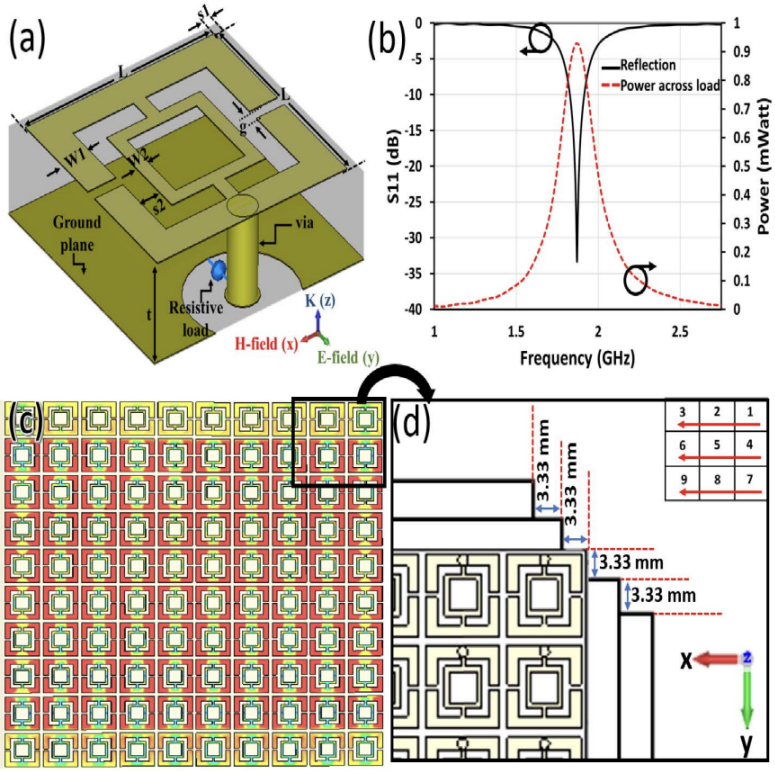


Figure 2.19: (a) Schematic depiction of the designed ELC unit cell. (b) Simulation outcomes of the unit cell featuring the reflection coefficient S11 and the power dissipation in the resistive load at the resonance frequency of 1.9 GHz. (c) Surface current distribution on the ELCs at the resonance frequency. The visualization uses a color gradient where red indicates the highest intensity at 112 A/m, and blue denotes the lowest intensity at 0 A/m. The uneven current distribution near the edge of the metasurface arises from the lack of periodicity in those particular unit cells. (d) Metasurface scanning procedure demonstrating the length and direction of the scan steps. The inset illustrates the sequence of scanning steps [2].

the variation in the input impedance of the ELC at the upper and lower edges in the y-direction of the metasurface, it is anticipated that the surface current and power in the resistive loads of the ELC cells along those edges will differ from the rest of the unit cells. The discrepancy in surface currents along the edges in the x-direction was less noticeable due to the specific polarization of the excitation field.

The metasurface array, sized at 10 cells × 10 cells, provides a resolution of 100 pixels, which might be inadequate. To increase resolution, the entire metasurface was shifted in the x-y plane by a fraction of a unit cell. Three initial scan steps moved in 3.33 mm increments in the x-direction. The metasurface returned to the starting position (x = 0, y = 0) and then shifted by one step in the y-direction by 3.33 mm. By doing so, each unitcell would capture 9 positions instead of 1 position in the x-y plane, thereby increasing the metasurface resolution from 100 pixels to 900 pixels (see Fig. 2.19(d)).

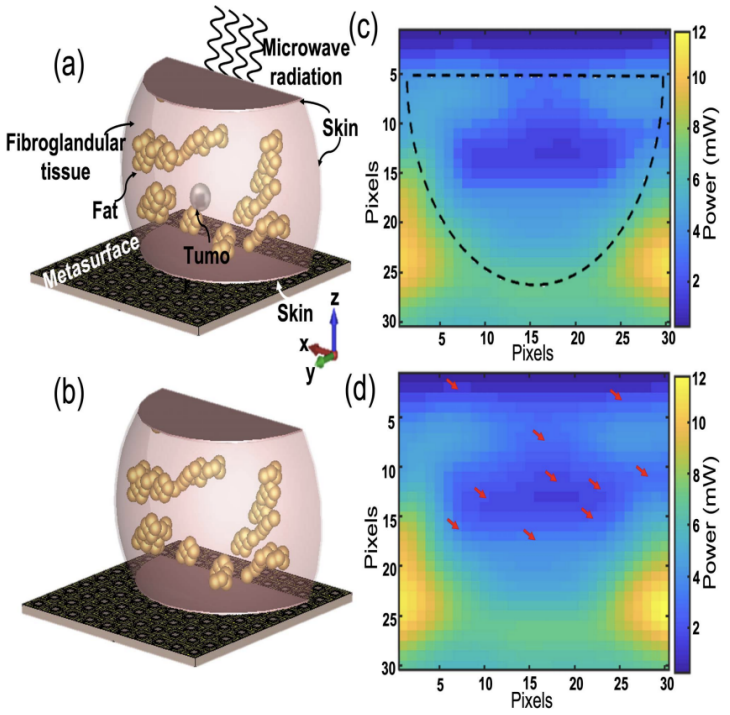


Figure 2.20: Models depicting an extremely dense breast: (a) featuring a 5-mm tumor and (b) without a tumor. Power pattern recordings on the metasurface film for various breast models: (c) displaying a breast with a cancerous tumor and (d) without a tumor. The red arrows highlight specific areas of differentiation compared to (c) [2].

Two identical and highly dense breast models were created, both containing a tumor with electrical conductivity and relative permittivity greater than that of fibroglandular tissue, with a diameter measuring 10 mm, as depicted in Fig. 2.20 (a) and (b). These breast models were exposed to a plane wave with an electric field intensity of 150 v/m. The power impressions captured by the metasurface for breasts with and without tumors

are illustrated in Fig. 2.20 (c) and (d). A noticeable distinction is observed between the recorded power impressions for the normal breast and the breast with a tumor. The tumor was positioned approximately 25 mm away from the metasurface film in the z-direction.

Clinical Studies Overview and Critique

Sani et al. (2021) evaluated the MammoWave microwave breast imaging system in a study involving 58 women divided into two age groups: 20–49 and 50–80 years. The study analyzed empirical image parameters without employing a classification algorithm. Results showed a sensitivity of 74% and a specificity of 62%, demonstrating moderate accuracy in distinguishing breasts with lesions from those without [56]. *Critique:* The study's reliance on empirical features without algorithmic classification limits clinical robustness. The small sample size and lack of biopsy-confirmed diagnosis reduce diagnostic validity. Specificity is moderate, indicating a risk of false positives.

Sánchez-Bayuela et al. (2023) performed a multicentric prospective trial including 353 women and stratified participants by breast density. Using AI-based classification, the MammoWave system achieved an overall sensitivity of 82.3% and a specificity of 50%. Performance was higher in dense breasts [57]. *Critique:* Despite the improved sensitivity and use of machine learning, the low specificity raises concern about false positives. Lack of histological validation and moderate diagnostic confidence suggest a need for further algorithmic and system refinement.

Moloney et al. (2021) investigated the Wavelia microwave imaging system in 24 patients with palpable breast lumps. The study highlighted the ability to visualize tumor-specific features in microwave images but did not report quantitative performance metrics like sensitivity or specificity [58]. *Critique:* Limited to a small high-risk cohort, the findings cannot be generalized to screening populations. The lack of numerical diagnostic indicators limits the evaluation of performance, making it more of a feasibility study than clinical validation.

Shere et al. (2019) evaluated the MARIA (Micrima) system in a multicenter study involving 225 symptomatic patients aged 16–89. The system demonstrated a sensitivity of 76% using radar-based microwave imaging for lesion detection [59]. *Critique:* While notable for its larger sample, the study lacks specificity reporting. The inclusion of only symptomatic cases restricts its utility in a general screening context. Comprehensive metrics are needed for broader clinical applicability.

Janjic et al. (2021) introduced the SAFE system and conducted a clinical evaluation in 115 women, reporting a sensitivity of 63%. The study emphasized its non-ionizing and

affordable design but did not report specificity [60]. *Critique:* The relatively low sensitivity and absence of specificity data hinder robust evaluation. Without histopathological confirmation, diagnostic accuracy remains uncertain. It holds potential for adjunctive screening, but not as a standalone tool yet.

Kemp Jacobsen et al. (2015) analyzed over 2.8 million mammography exams in the U.S. and Denmark. For women aged 50–69, film and digital mammography achieved a sensitivity of 82.3% and specificity of 83.2%, establishing these methods as benchmarks for population-level screening [61]. *Critique:* Highly robust and well-designed, the study offers a strong benchmark. However, variability across national practices and limited insights for younger age groups or dense breast tissue may influence generalizability.

Zeeshan et al. (2018) assessed digital mammography in 122 women over the age of 30. They reported a high sensitivity of 97% and specificity of 64.5%, confirming its value in early breast cancer detection [62]. *Critique:* Although the sensitivity is excellent, the lower specificity points to a notable false positive rate. The study's small scale and single-center nature may limit its broader clinical applicability.

Table 2.2: Summary of clinical investigations of microwave and conventional breast imaging systems

System	**Cohort**	**Age**	**Sensitivity**	**Specificity**
MammoWave[56]	58	20–49 (27), 50–80	74%	62%
MammoWave[57]	353	(31)	82.3%	50%
Wavelia[58]	24 (all with palpable cancer lumps)	35–83	not reported	not reported
Maria[59]	225	mean 52.1, min. 16, max. 89	76%	not reported
SAFE[60]	115	not reported	63%	not reported
Film & Digital Screening Mammography (initial screening only)[61]	USA only: 2,872,791	50–69	82.3%	83.2%
Digital Screening Mammography (initial screening only)[62]	122	>30	97%	64.5%

Table 2.3: Summary of different MI methods and algorithms

Author's reference	Operating frequency	Number of antennas	Method	Tumor size (diameter)	Image reconstruction algorithm
Bridges [48]	15 GHz	1	2D-CMI	2 mm	NA
Hagness et al. [63]	6 GHz	17	3D-FDTD-CMI	2 mm	NA
Fear et al. [64]	10 GHz	2	2/3D-FDTD-CMI	1.2 cm	ISA
Shannon et al. [65]	6 GHz	17	2D-FDTD-TSAR	NA	NA
Nilavalan et al. [66]	6.5 GHz	16	2D-FDTD-CMI	2 mm	SSA
Kosmas et al. [67]	5 GHz	23	2D-FDTD	3 mm	TR
Chen et al. [68]	8 GHz	7	2D-FDTD	4 mm	TR
Klemm et al. [69]	6 GHz	16	3D-FDTD	4 mm	DAS and RCB
Teo et al. [70]	6 GHz	5	2D-FDTD	5 mm	GNIA
Klemm et al. [71]	2 GHz	60	3D-FDTD	NA	NA
Mohan et al. [72]	3.5 GHz	21	3D-FDTD-CMI	NA	TR MUSIC
Kurrant et al. [73]	3.8 GHz	2	2D-FDTD	NA	TOF
Elahi et al. [74]	6 GHz	50	3D-FDTD-CMI	8mm	AR

Chapter 3

Using Low-Frequency Electromagnetic Fields for Breast Cancer Detection

This chapter is based on the following published work:

H. Akbari-Chelaresi, D. Alsaedi, S. H. Mirjahanmardi, M. Badawe, A. Albishi, V. Nayyeri, and O. Ramahi, "Mammography using low-frequency electromagnetic fields with deep learning," *Scientific Reports*, vol. 13, p. 13253, Aug. 2023.

3.1 Introduction

The absence of reliable, non-invasive, and high-resolution technologies to detect breast malignancies at early stages has resulted in increased morbidity and poor quality of life for many women. Current technologies have been facing critical challenges that are associated with health-related issues, scanning time, and affordability. Considering the fact that breast cancer is the most common cancer amongst women, proposing new techniques for breast cancer detection, which can eliminate the aforementioned challenges and improve the diagnosis resolution, is of significant importance[75]. Such techniques can lead to early-stage detection, thereby increasing the chance of full recovery[76].

One of the traditional methods for cancer detection is X-ray mammography. Although this technology is relatively inexpensive and suitable for detecting malignant tissues in low-density breasts, it has a potentially harmful effect due to ionizing radiation. For

high-density breasts, diagnosis of cancerous tumors is challenging owing to a high overlap between fat and malignant tissues[77, 78]. Magnetic resonance imaging (MRI) is used as a complementary diagnosing tool, providing higher accuracy than X-ray mammography, especially for high-density breasts. However, being costly, MRI cannot be used for regular screening, particularly in low-income communities[79]. Ultrasound is also used for breast-cancer diagnoses; however, its accuracy in detecting tumors depends on the radiologist's expertise[80].

In recent years, breast cancer detection techniques based on microwave imaging (MWI) have been introduced as an alternative to the aforementioned traditional methods[3, 31, 81–84]. MWI uses non-ionizing electromagnetic (EM) waves instead of potentially hazardous ionizing waves. In addition, low-frequency electromagnetic excitation allows for deeper penetration, thereby increasing the ability to diagnose anomalies buried deep inside denser breasts[85, 86]. Furthermore, MWI takes advantage of low-cost system integration. The main components of any MWI-based system are transmitters (antennas) to emit EM waves and receivers (detectors) to capture the data in the form of the EM field distribution, which is correlated to the permittivity of tissues[32, 87]. The collected data is then sent to a computer for image construction.

Generally, technologies based on MWI can be categorized as radar-based imaging technology and microwave tomography[88]. The radar-based imaging technique constructs images using reflected waves from the objects under examination[89], whereas microwave tomography techniques are mainly founded on inverse scattering algorithms to construct an image of the object[36]. Nevertheless, all current technologies based on MWI have been facing critical challenges such as the complexity of the system (due to using multiple antennas), the need for impedance-matching liquid between the breast and antennas in a wide variety of cases, the complication of the image construction using experimental data, and low accuracy and resolution owing to the coupling between the antennas (detectors)[82, 85]. Microwave-based systems have also been introduced for breast cancer detection without the need for full breast imaging[29, 30].

In a recent work, we introduced a new microwaves-based modality for breast cancer detection, which is identical in concept to X-ray mammography but using microwaves[2]. The key concept behind this new and simple modality is achieving an impression of the female breast that correlates to the constituents of the breast. This impression is captured using a metasurface consisting of an ensemble of electrically-small resonators stitched to achieve good electromagnetic energy absorbance. Then, artificial intelligence is used to train the system to provide a conclusion as to the probability of the existence of a tumor within the breast. The developed system in [2] has two fundamental limitations. The first is due to the metasurface used to capture the impressions. This metasurface is constrained

by its unitcell size, which directly relates to the frequency at which the system can operate. To achieve higher impression resolution, the metasurface needs to have a higher number of smaller cells (which resemble pixels). However, smaller cells typically resonate at higher frequencies, limiting the penetration of the electromagnetic field into the breast. The second challenge relates to the non-highly accurate impressions achieved. Since a relatively high frequency was used in [2] (around 2.0 GHz), the achieved impressions could not give a robust correlation to all the constituents of the breast, again, for the simple reason that at 2.0 GHz, the penetration into the breast is shallow and does not cover the entire volume of the breast [90].

Deep neural networks have shown remarkable performances across various medical imaging domains, performing tasks such as classification, detection, segmentation, and reconstruction. Artificial neural networks (ANNs) require a large amount of high-quality data for efficient training and to achieve reliable outputs. Hence, part of their successes is indebted to the abundant data collected from widely used imaging modalities, including MRI, computerized tomography (CT), ultrasound, and pathology. While the implementation of ANNs in the microwave domain dates to more than two decades ago by training shallow networks (containing one fully connected hidden layer) [91], only recently attempts were reported to use deep networks [92, 93]. One of the underlying reasons is due to data scarcity of microwave images. The recent works proposed a conventional convolutional neural network (CNN) to enhance the microwave imaging resolution, while the earlier works used an auto-encoder followed by a secondary CNN for image reconstruction purposes.

Deep learning (DL) algorithms are conventionally categorized into supervised learning, weakly supervised learning, and unsupervised learning. In supervised learning, a set of M training samples $\{(x_i, y_i)\}_{i=1}^{M}$ exist where for each input x_i an annotated label, y_i is available. The objective is to train the network $g_\theta : x \rightarrow y$ based on minimizing a loss function $\mathcal{L}$ that predicts the most accurate label for an unknown test image. Weakly supervised methods leverage only the coarse-grained annotations to deduce the fine-grained labels, while unsupervised learning requires no annotations and aims at recognizing patterns in the data.

Here, our main objective is to provide the majority of women who are under risk of breast cancer worldwide with a modality that can be used frequently. As discussed earlier, MRI modality is neither affordable nor convenient for frequent screening. Also, x-ray mammography can cause health issues for patients due to potentially ionizing radiation. Our proposed modality is most suitable for screening purposes, owing to its non-hazardous, low-cost, and easy-to-use features.

In this work, we present a design of a mammography system for detecting tumors using

low-frequency electromagnetic fields (LFEMF) that overcomes the challenges in our earlier work[2]. First, instead of using a plane wave excitation that requires a horn antenna placed in the far field of the breast under examination, a simple electrically-small dipole antenna is used in the near field of the breast to provide a rich source of excitation that includes EM energy, containing all field polarizations. This type of excitation is intended to excite all constituents of the breast, thereby creating an impression that is inclusive of most breast tissues. Second, to enable a much lower frequency excitation and, as a result, effectively increase the penetration and impression resolution, we have designed a metasurface made up of an ensemble of highly miniaturized unitcells that operate at 200 MHz (which is one order of magnitude reduction as compared to the earlier design[2]). Third, we employ a new technique in the image processing stage, which is based on the comparison between healthy and unhealthy breast models. In fact, after capturing the images, unlike the previous work [2], the dataset images will first be pre-processed and then fed into the neural network algorithm to train the introduced architecture in a supervised manner.

3.2 Unitcell Design

The metasurface functions similarly to the X-ray film in X-ray mammography. Essentially, it comprises a collection of small resonators, often called unit cells. When these unit cells are positioned closely together, they form a closely-packed array, causing each unit cell's input impedance to be significantly influenced by its neighboring cells. These unit cells can be crafted using various designs found in existing literature, such as electric-inductive-capacitive (ELC) resonators known for their high responsiveness to incoming electric fields[2, 94]. Such a unit cell is constructed using capacitors and inductors, achieved through gaps and conductive ring patterns. An important aspect of designing the metasurface for our specific purpose is to ensure minimal loss to maximize energy absorption at the terminals. Previous studies have demonstrated that a metasurface composed of ELC resonators can achieve nearly complete absorption but primarily for energy harvesting applications.

Given that our target frequency is approximately 200 MHz ($\lambda = 1.5$ m), the usual size of an ELC resonator would be relatively large compared to the size of the human female breast. This factor would eliminate the possibility of using the unit cell as a pixel to create an image of the breast. In essence, the quality of the image would be directly linked to the dimensions of the unit cell. To facilitate the necessary reduction in size of the unit cell to ensure that the metasurface could accommodate a substantial number of them for high-resolution imaging, we can enhance the equivalent capacitance and/or inductance.

Table 3.1: Design Parameters of the unitcell

Parameter	Value	Parameter	Value
$L_{1,2,3,4}$	100 nH	$R_{1,2}$	470Ω
w_1	1.4 mm	w_2	0.6 mm
$g_{1,2}$	1 mm	l	9.5 mm
s_1	0.5 mm	s_2	1 mm
$d_{1,2}$	1.3 mm	t	4 cm

By doing so, we would effectively decrease the frequency in line with Equation (3.1).

$$f_r = \frac{1}{2\pi\sqrt{LC}}, \tag{3.1}$$

The resonance frequency (f_r) depends on the equivalent capacitance (C) and inductance (L) of the ELC resonator. To enhance the capacitance, the space between the metallic sections of the resonator must be significantly reduced. While this is achievable in manufacturing, it would intensify fabrication tolerances and expenses. Therefore, our strategy involves increasing the inductance by incorporating lumped inductors into the inner and outer rings of the proposed ELC resonator. The idea of adjusting resonance frequencies using discrete elements like inductors, capacitors, and resistors to downsize electrically-small resonators has been explored in earlier studies, such as[95], and related references. Subsequently, the resonance frequency can be adjusted to optimize the S-parameters for maximal absorption.

The proposed unit cell, which represents a downscaled ELC resonator, is depicted in Fig. 3.1. To maintain symmetry in both the x and y directions, the splits were chosen to be at the midpoint of the rings, and the values of the inductors and resistors were made identical. Furthermore, rather than implementing a single via, two vias were utilized to maintain a level of symmetry concerning the incoming electromagnetic field [96]. To reduce losses, our design incorporates a low-loss Rogers substrate (TMM10i) featuring a relative permittivity of $\epsilon_r = 9.8$ and a loss tangent of $\tan(\delta) = 0.002$.

The unit cell was simulated using CST Microwave Studio[97]. Because the unit cell is meant to be positioned within a structure that infinitely repeats itself in both the x and y directions, a perfect magnetic conductor boundary condition (PMC boundary condition) was applied in the x-direction, and a perfect electric conductor boundary condition (PEC

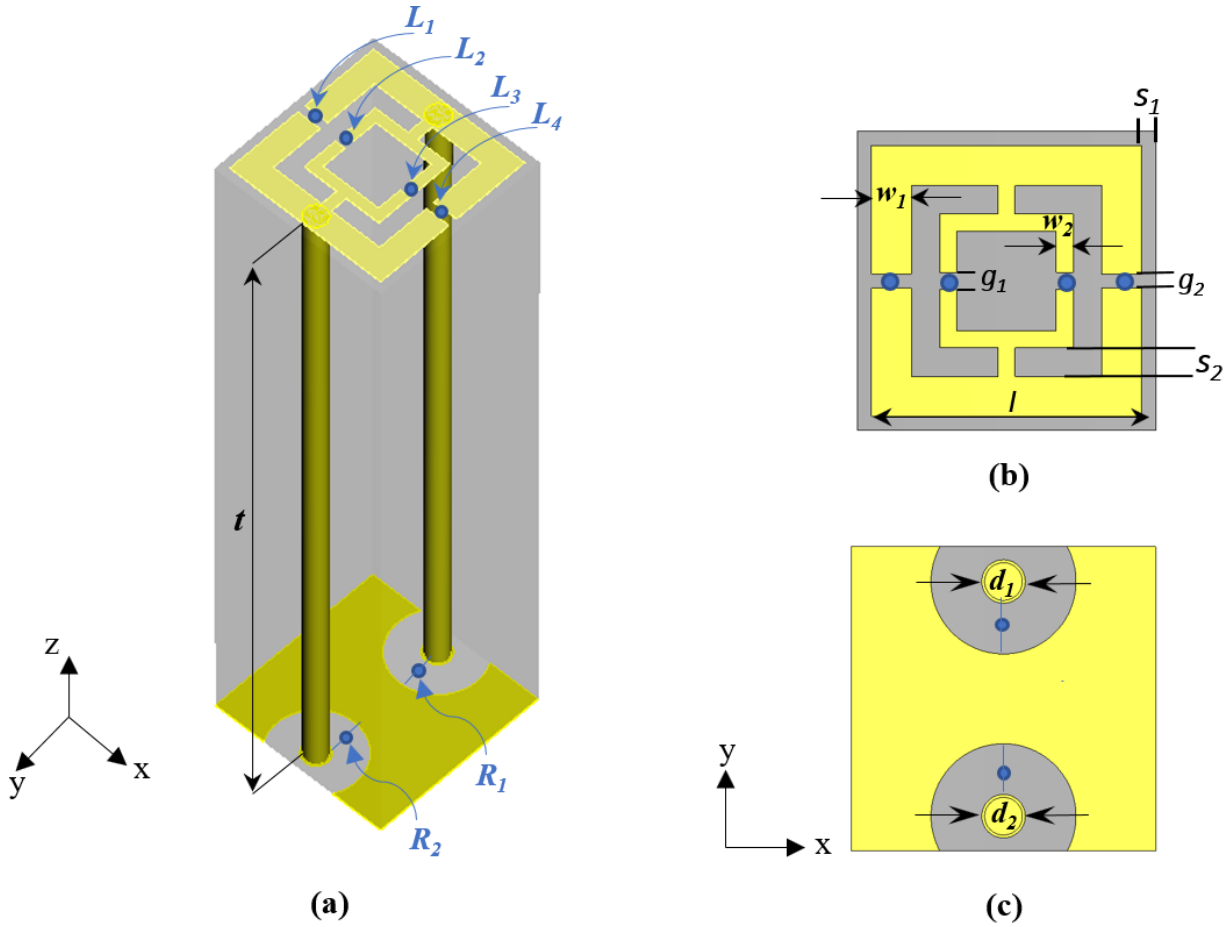


Figure 3.1: a) 3D view of the unitcell, (b) top view, and (c) bottom view.

boundary condition) was applied in the y-direction to account for the structure's periodicity in the modeling. The unit cell's performance was assessed by illuminating it using a plane wave port placed above the unitcell and subsequently recording the $|S_{11}|$ graph. It is important to note that the plane wave port is in the air.

The unit cell underwent optimization based on two primary objectives: achieving a minimum $|S_{11}|$ and maximizing the Q-factor. The optimized parameters for the unit cell are detailed in Table 3.1. This specific unit cell has dimensions of 10.5 mm $\times$ 10.5 mm with a thickness of 4.0 cm, which enables increased inductance due to the extended vias. Fig 3.2 illustrates the unit cell's response, exploring three key parameters: the substrate thickness t, the inductance values of the inductors ($L_1 = L_2 = L_3 = L_4 = L$), and the resistance

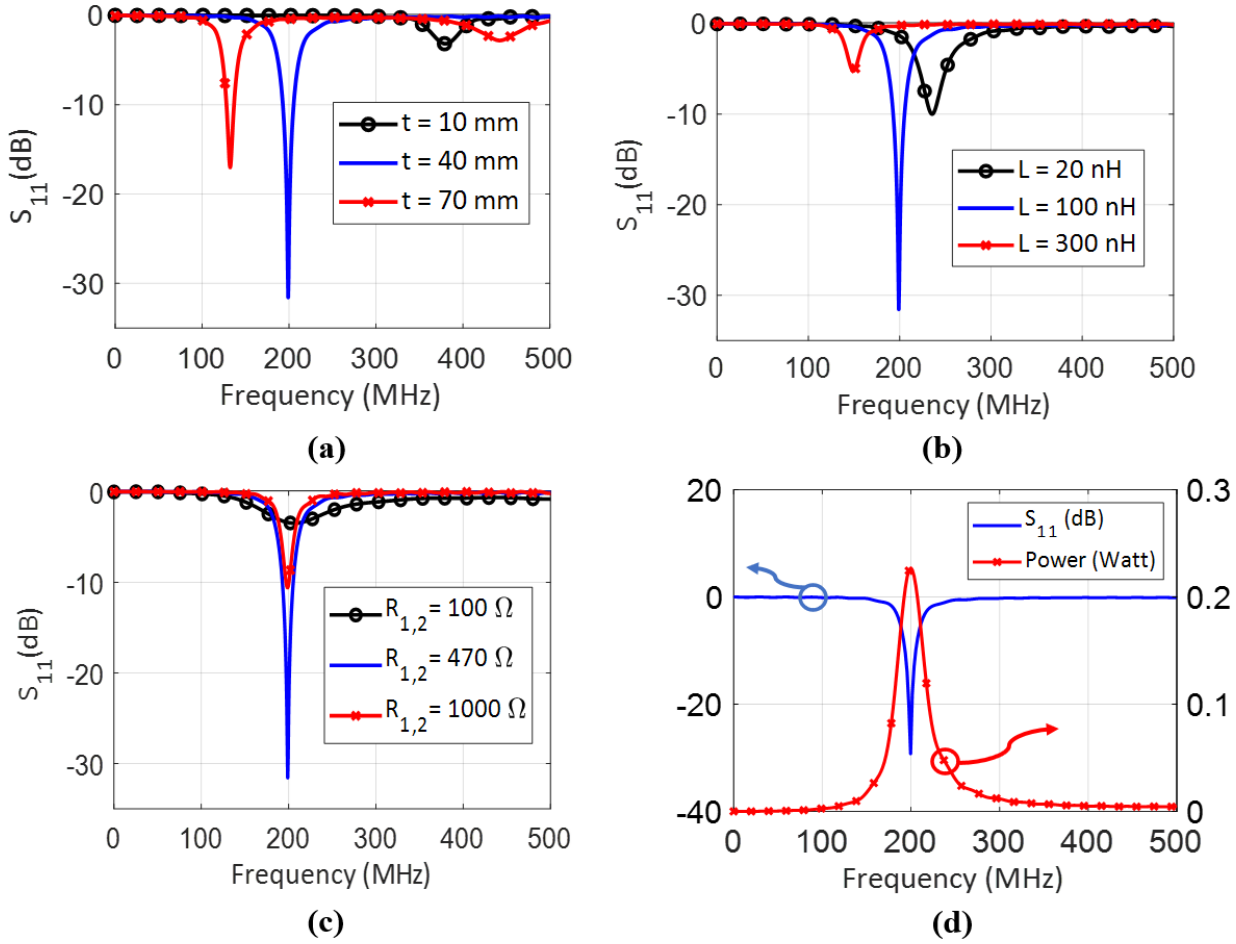


Figure 3.2: $|S_{11}|$ for different values of (a) t, (b) L, and (c) $R_1 = R_2$, where the non-variant parameters are set to L = 100nH, $R_1 = R_2 = 470\Omega$, and t = 40 mm. (d) $|S_{11}|$ and power delivered to the terminal resistors of the optimized unitcell, where the incident power is 0.5 Watts.

values of the terminations ($R_1 = R_2$) (refer to Fig. 3.1).

Figure. 3.2(b) demonstrates that the resonance frequency can be adjusted by modifying the inductance of the lumped inductors. Fig. 3.2(c) illustrates that the minimum of |S11| happens for the value of $R1, 2 = 470\Omega$ at the unit cell's resonance frequency, indicating ideal impedance matching between the free space and the cell.

Figures. 3.2(a),(b), and (c) show that the impedance matching is affected by the vias' length (t), the inductors' inductance L, and the termination resistors $R_1 = R_2$, respectively.

We further observe that for t = 40 mm, L = 100 nH, and $R_1 = R_2 = 470\ \Omega$, $|S_{11}|$ has a minimum value of lower than −30 dB, corresponding to a very strong impedance matching at 200 MHz, and a Q-factor of 16. This strong absorbance (matching) will not happen for other values of the parameters under study in Fig. 3.2.

Figure. 3.2 (d) shows the response of the optimized unitcell with the parameters given in TABLE 4.4. It can be seen that 0.46 Watts (92%) out of 0.5 Watts incident power is delivered to the termination resistors (0.23 Watt in each resistor), and 0.04 Watts (8%) is lost due to dielectric and ohmic loss.

3.3 LFEM Imaging System Design

A metasurface was constructed as a 10 × 10 array using the aforementioned unit cell. Fig. 3.3(a) and (b) present the top and bottom views of this metasurface. Each unit cell functions as a pixel, and its value will be determined by measuring the power dissipation at the respective termination resistors. Due to the symmetry in the unit cell, the received power will be evenly split between the resistors. Consequently, by measuring the dissipated power in one of the termination resistors of a unit cell and repeating this process for all unit cells, we will generate a two-dimensional power map. This power map effectively serves as an impression-image, where the position (xn,yn) of each unit cell and its termination power dissipation contribute to the construction of the image. This image reflects the power absorbed by the unit cells, essentially acting as pixels.

We have leveraged the technique proposed in [2] to record a 30 × 30 impression instead of a 10 × 10 impression. Considering that the length of the unitcell is Δx, in addition to the reference position, we recorded the impressions by shifting the whole metasurface with the value of Δx/3 and 2Δx/3 in both x and y directions. By doing so, nine different combinations of metasurface positions will provide us with nine pixels for each unitcell. Thus, using the whole array, with the same metasurface, an impression with 900 pixels, rather than 100 pixels, will be created (see Fig. 3.3 (c)).

In our prior research[55, 98, 99], it was demonstrated that within the near field, the resolution can significantly surpass the Abbe diffraction limit. When the radiation source is positioned very close to the breast, the electromagnetic field interacting with the breast encompasses all polarizations. Therefore, under such excitation—unlike plane wave excitation, where the impinging field is polarized in a single direction—the interaction between the impinging fields and the breast components generates a scattered or secondary field that carries richer and more comprehensive information.

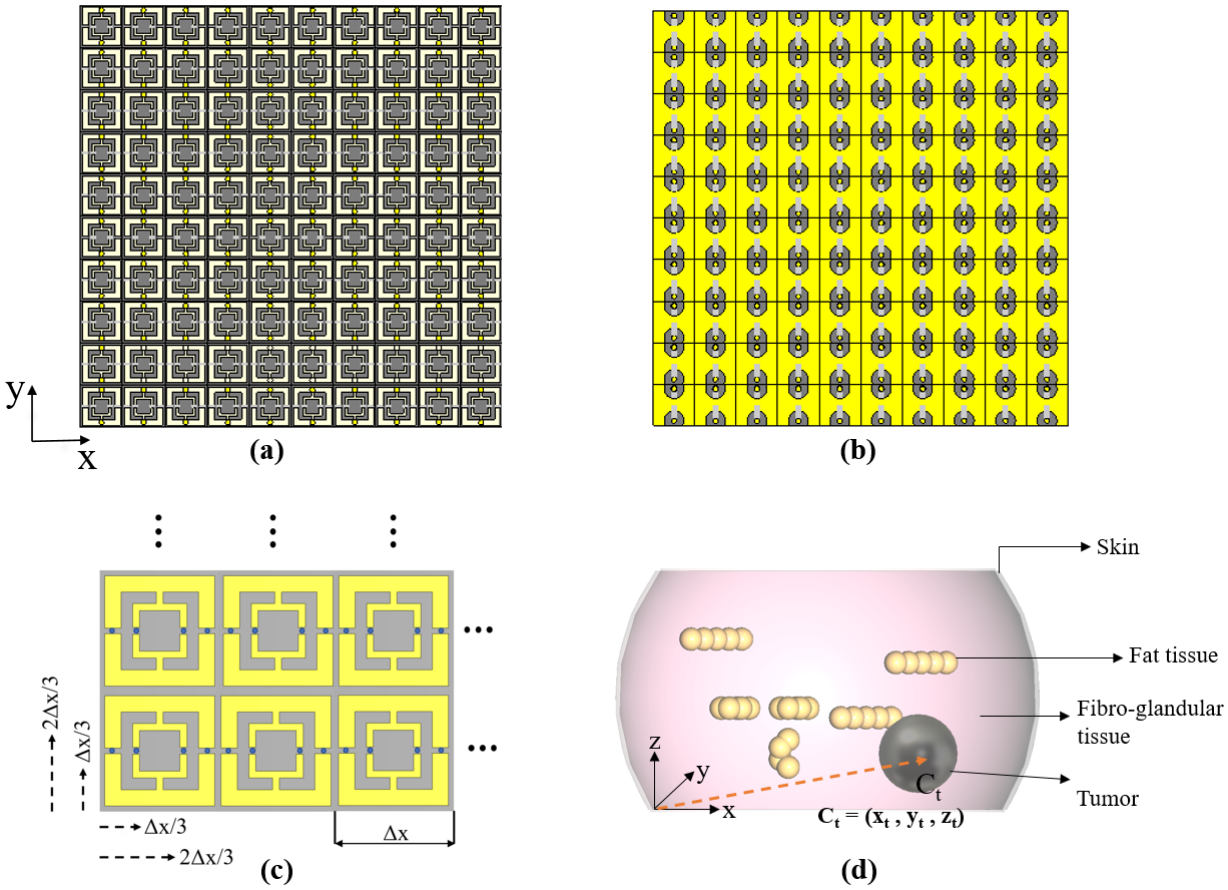


Figure 3.3: Metasurface array (10 cm × 10 cm): (a) top view and (b) bottom view, showing the two termination resistors (c) scanning technique for increasing the pixels of the impression, where $\Delta x = 1$ cm is the length of the square unitcell. The arrows show the directions of the displacements. (d) breast model, inclusing skin, fat tissues, fibro-glandular tissues, and a tumor positioned at C_t with the diameter of 10 cm.

Recalling the spring and mass model describing a molecule interacting with electromagnetic waves, the formation of dipole moments within the sample results in molecular polarization. The response of molecules inside the breast varies depending on the polarization of the incident field. Therefore, when different polarizations are generated by the radiation source, the molecules within healthy and cancerous tissues will respond differently. This leads to the creation of distinct impressions on the metasurface, offering independent information. For our setup, an electrically small dipole with a length of $\lambda/10$

and a diameter of $\lambda/1000$, positioned in very close proximity to the breast, was employed as the radiation source.

In the numerical simulations, various types of breast models were considered to cover the diversity found in the human female breast. The primary constituents of the breast are fibro-glandular and fat tissues[100]. The density of the breast model was categorized based on the concentration of the fibro-glandular tissues. Fig. 3.3 (d) demonstrates the breast model used in the CST simulation, including skin, fat tissue, fibro-glandular tissue, and a tumor. Four distinct categories of the breast model were examined:

1- Extremely dense breast (more than 75% fibro-glandular tissue)
2- Heterogeneously dense (50% to 75% fibro-glandular tissue)
3- Fibro-glandular scattered areas (25% to 50% fibro-glandular tissue)
4- Entirely fatty (less than 25%)[100, 101].

The percentage compositions of fat and fibro-glandular tissues can greatly vary among women.However, the mean composition of the fibroglandular tissues, including skin, varies from 13.7% to 25.6% with the overall mean of 19.3% [102]. This means that most of the women in the statistical population are classified under entirely fatty category, which makes MWD process less challenging. In fact, the contrast between the fibroglandular and tumorous tissues is not as significant as the contrast between the fat and tumorous tissues. Thus, the examination of extremely and heterogeneously dense breasts is more difficult than that of fibroglandular-scattered and entirely fatty breasts[103].

Table 3.2: various locations of the tumor

Descriptive location	Coordinate of the tumor's center
upper-left corner (C_{t1})	(70 mm, 15 mm, 15 mm)
upper-right corner (C_{t2})	(20 mm, 15 mm, 15 mm)
lower-left corner (C_{t3})	(70 mm, 35 mm, 15 mm)
lower-right corner (C_{t4})	(20 mm, 35 mm, 15 mm)

For the purpose of validating our concept, the breast is considered to be a hemisphere with a radius of 50 mm, covered with a layer of skin with a thickness of 2 mm. The internal composition of the breast consists of fibro-glandular and fat tissues. At the operating frequency of 200 MHz, the relative permittivity and electrical conductivity for the fibro-glandular tissue are close to 64 and 0.8 S/m, whereas for fat tissue, they are close to 5.6

and 0.03 S/m[104].The center C_t of the spherical tumor, modeled as a perfect conductor (PEC), has been placed at (x_t, y_t, z_t) with reference to the origin of the cartesian coordinate system shown in Fig. 3.3(d). This is a good preliminary electromagnetic model to guarantee sufficient contrast between the tumor and healthy tissues[105]. In TABLE 3.2, the locations of the tumor and their corresponding coordinates are listed. These locations were used to produce the dataset for the classification exercise.

3.4 Numerical Simulation, Results, and Discussion

The simulation setup is illustrated in Fig. 3.4. CST's time-domain solver was employed for this study, primarily due to its superior computational efficiency. Unlike frequency-domain solvers that solve Maxwell's equations at discrete frequency points, the time-domain solver computes the entire time evolution of the fields in a single run, which makes it significantly faster—especially when simulating multiple scenarios for dataset generation. The computational domain was discretized using a hexahedral mesh, which was automatically refined around critical regions such as the metasurface and the breast phantom to ensure numerical accuracy. The CAD model of a breast phantom was used in the simulation, with a dipole antenna positioned 1 cm above its surface to serve as the source of illumination. The metasurface was placed directly beneath the phantom, with an approximate stand-off distance of 1 cm between the phantom and the metasurface. To generate the imaging data, the power dissipated in the resistive elements of each metasurface unit cell was recorded. These values were then spatially mapped and visualized using MATLAB to reconstruct the internal profile of the phantom.

Fig. 3.5 illustrates the impression of a healthy breast model and that of a breast with a 10 mm tumor placed at the upper-left corner (C_{t_1}, see TABLE 3.2) of the breast model. Considering Fig. 3.5, we can see that the differences between the two impressions seem to be negligible to the naked eye. To enhance the resolution, and consequently the potential to increase the differentiation in the impression for the breast with and without the tumor, we subtract each impression of a tumorous breast from the impression of the same breast but without the tumor.

In the next step, we add a tumor sample with different dimensions in various locations. At first, a spherical tumor sample made of PEC with a radius of 10 mm is placed at four different locations: the upper-left corner (C_{t_1}), the upper-right corner (C_{t_2}), the lower-left corner (C_{t_3}), and the lower-right corner (C_{t_4}) of the breast (see TABLE 3.2 and Fig. 3.6(a)-(d)). We have selected these locations to show the quality of the impressions and their

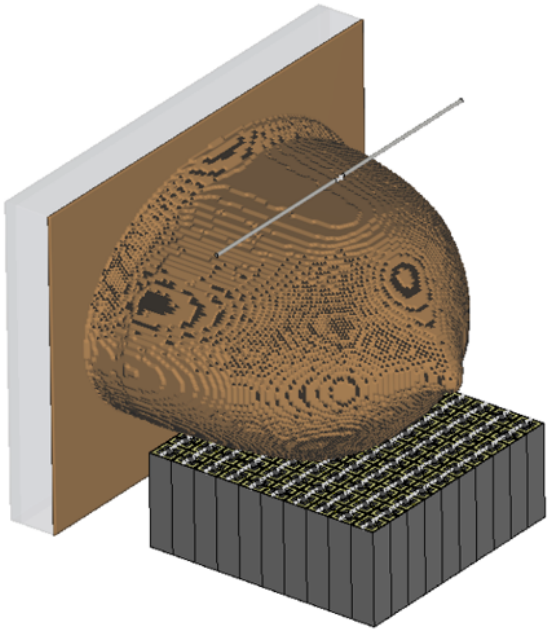


Figure 3.4: Simulation setup

.

ability to detect the locations of the tumors and to better observe subtle dissimilitudes between different impressions.

The effectiveness of the subtraction technique presented in this work is based on the assumption that the left and right breasts are identical for the vast majority of women. Statistically, the magnitude of relative BV (breast volume) asymmetry between the two breasts has a median of 2.71%, and the magnitude of relative DV (dense volume) asymmetry has a median of 3.28% [106]. By applying the subtraction technique mentioned above, we can observe in Fig. 3.6(e)-(h) that the most pronounced differences were around the tumor's location. In Fig. 3.6(e), (f), and (h), we observe that a strong correlation exists between the impressions and the locations of the tumors. However, in Fig. 3.6(g), the lightest pixels are somewhere different from the tumor's location, although we can see dimmer differences around the location of the tumor. Next, we analyze the results of the simulations for four different locations of a tumor with a radius of 7.5 mm. The tumor was placed in one of the four positions given in TABLE 3.2 (C_{t_1}, C_{t_2}, C_{t_3}, and C_{t_4}) as depicted in Fig. 3.7(a)-(d)). Fig. 3.7(e)-(h) show the impressions of the above-mentioned tumorous breast models after subtracting from the impression of the healthy breast. We observe that the most pronounced difference is close to the locations of the tumors. We

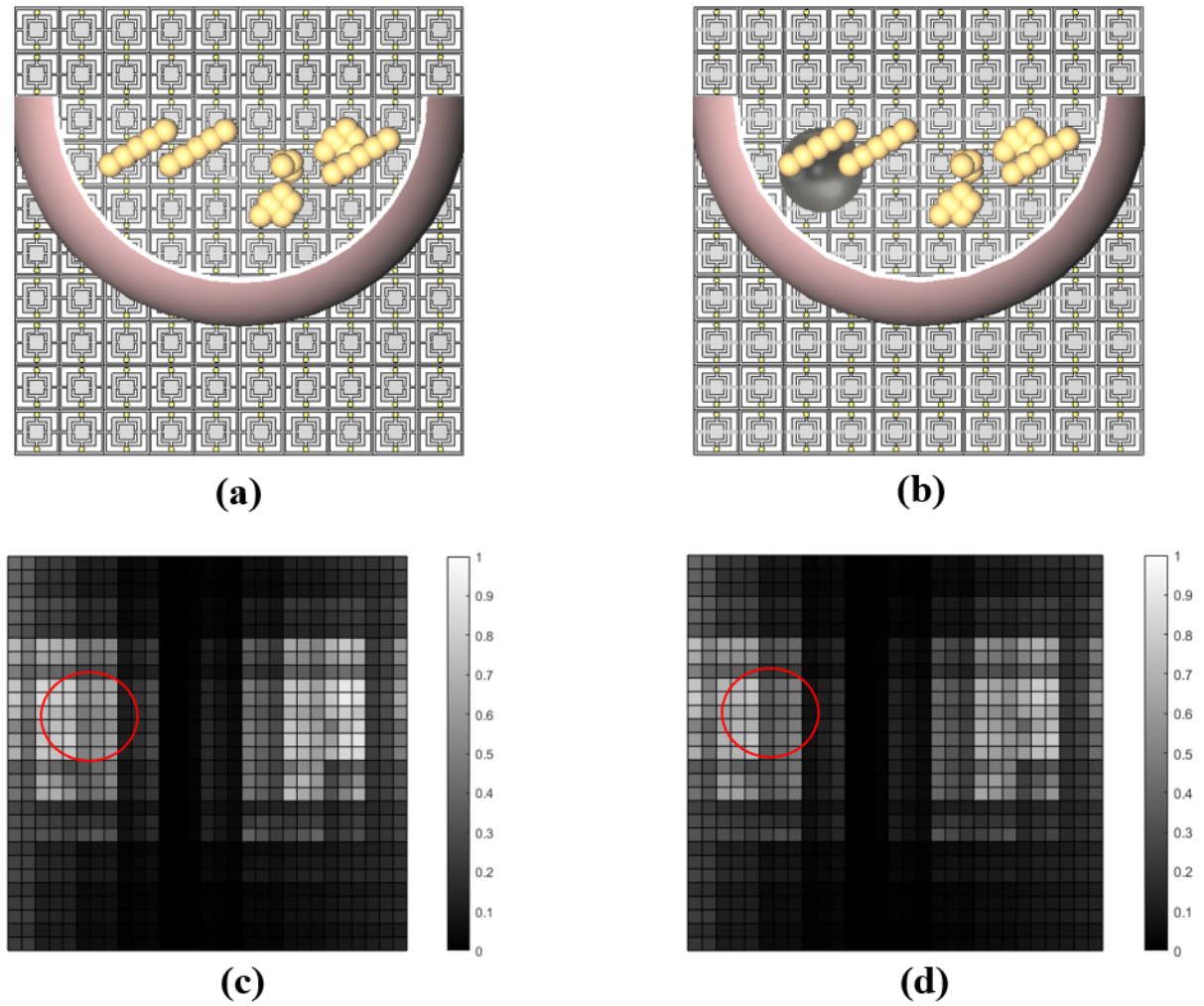


Figure 3.5: (a) Simulation model of the healthy breast (b) simulation model of the tumorous breast (c) recorded impression of the healthy breast (d) recorded impression of the tumorous breast, where the red circles indicate the border of the tumor with a radius of 10 mm and location of C_{t_1} (see TABLE 3.2).

.

also observe that the impressions cannot show the location of the tumors as accurately as those shown in Fig. 3.6(e)-(h). The reason is due to the smaller size of the tumors, which makes them more challenging to be recognized from the corresponding impressions. Another noteworthy point here is that the difference in magnitude has been reduced, in

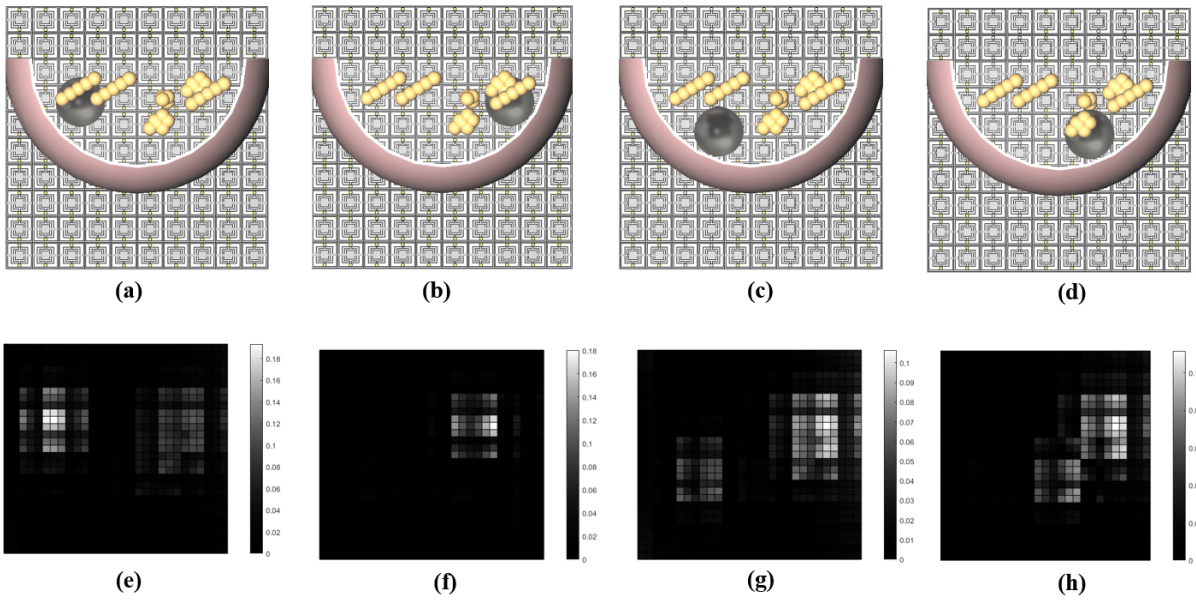


Figure 3.6: Model of the tumorous breast with a 10 mm tumor placed in: (a) upper-left corner, (b) upper-right corner, (c) lower-left corner, and (d) lower-right corner with the corresponding impressions shown in (e)-(h), respectively.

the sense that the maximum contrast of the impressions has decreased from 0.18 to 0.08 for 10 mm and 7.5 mm tumor sizes, respectively (see the color bars of Fig. 3.6(e)-(h) and Fig. 3.7(e)-(h)).

Finally, we investigate the results of the simulations for four different locations of a tumor with a radius of 5 mm. The tumor was placed in the same positions (see Fig. 3.8(a)-(d)). Fig. 3.8(e)-(h) show the impressions of the corresponding tumorous breast models after applying the subtraction method.

If the contrast in the achieved impressions is more than a DV asymmetry of 3.28%, there should exist some anomalies in the female breast. From the simulations, a contrast of more than 3.28% for 7.5 mm and 10 mm tumor sizes, was obtained, which confirms the effectiveness of the proposed modality in identifying an anomaly with such dimensions. However, the impressions for a tumor with 5 mm radius do not show the same level of dissimilarity, thus making it more difficult to identify tumors having a radius less than 5 mm (see the color bars of Fig. 3.8(e)-(h)).

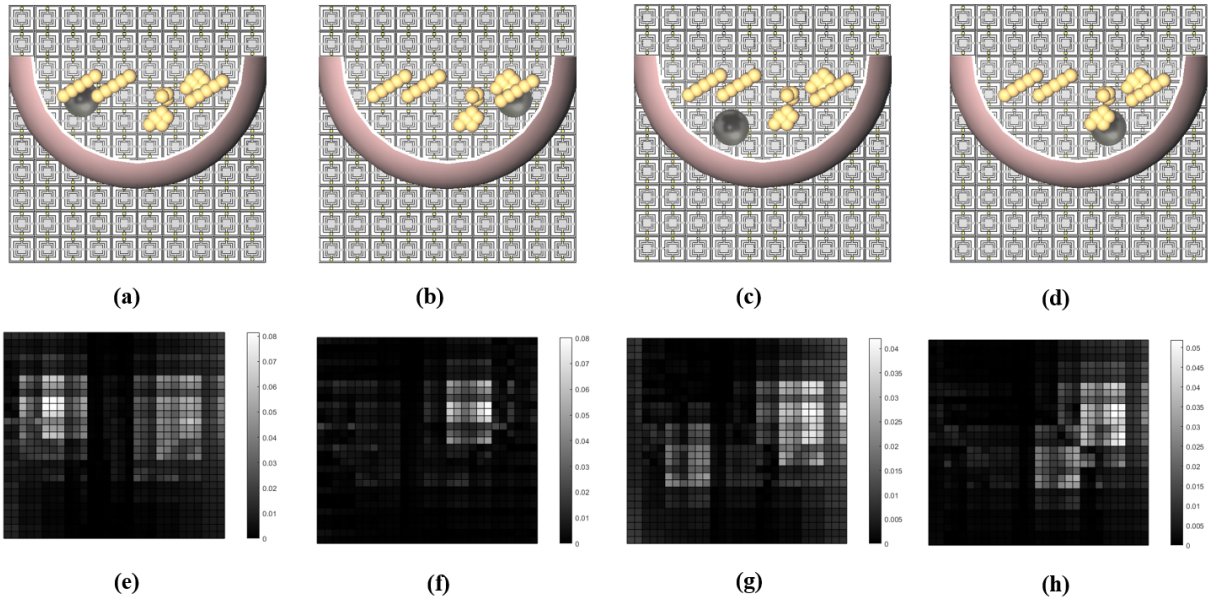


Figure 3.7: Model of the tumorous breast with a 7.5 mm tumor placed at: (a) upper-left corner, (b) upper-right corner, (c) lower-left corner, and (d) lower-right corner with the corresponding impressions shown in (e)-(h), respectively.

3.5 Deep learning classifications

Considering the last section, where we investigated different scenarios of tumor sizes and locations, we conclude that by simply using the subtraction method, we cannot achieve highly reliable results in terms of a strong correlation between the tumor presence and the corresponding impression. Increasing the number of classes for different tumor sizes and locations will make distinguishing the impressions from each other more complex. Therefore, to provide better tumor detectability, in the next section, we apply a deep learning (DL) method to classify different impressions and separate them from each other.

Since our objective is to detect the location and size of the tumors (not their shapes or numbers), for simplicity, we have chosen to do the simulations with spherical tumors and with different radii. The 12 breast models that we used in our dataset are different in their fat constituents. We started from an extremely dense breast model and gradually added fat tissues into the breast in order to make it fattier (see Fig. 3.9).

We have developed a deep learning architecture to classify the impressions recorded from the simulations. Fig. 3.10 (a) illustrates the complete architecture of the DL classifier. The

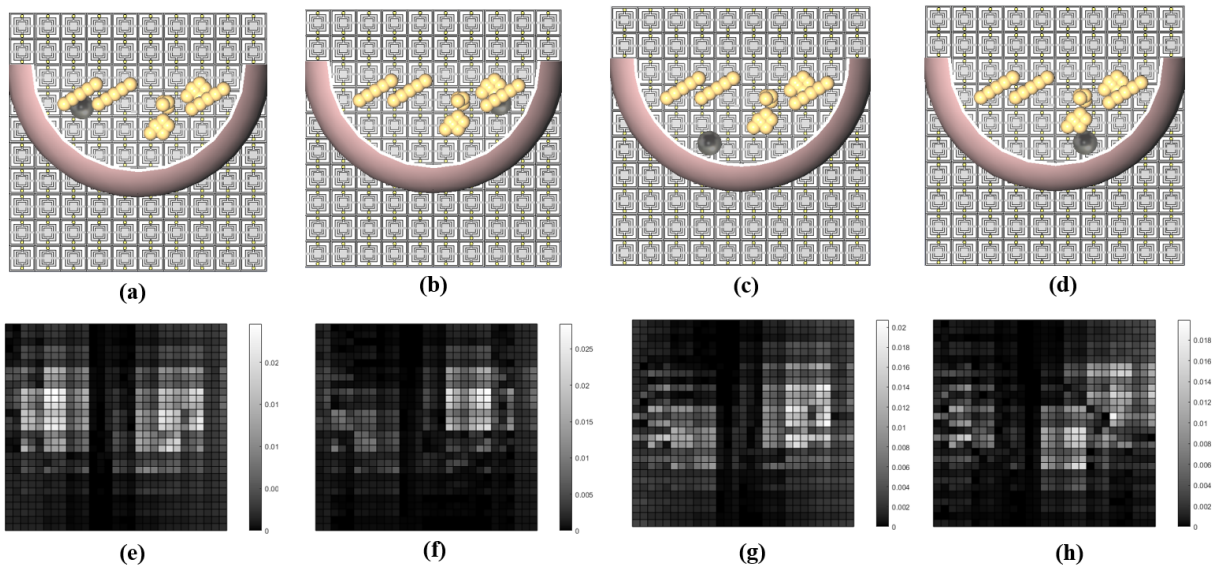


Figure 3.8: Model of the tumorous breast with a 5 mm tumor placed at: (a) upper-left corner, (b) upper-right corner, (c) lower-left corner, and (d) lower-right corner with the corresponding impressions shown in (e)-(h), respectively.

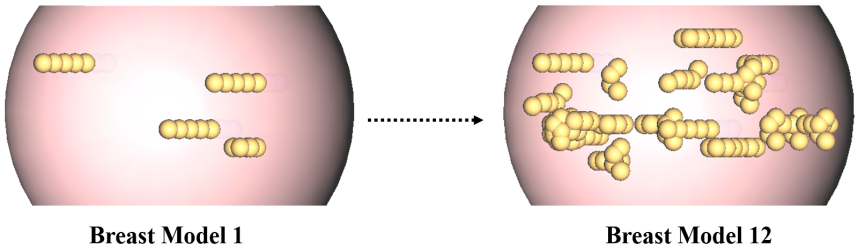
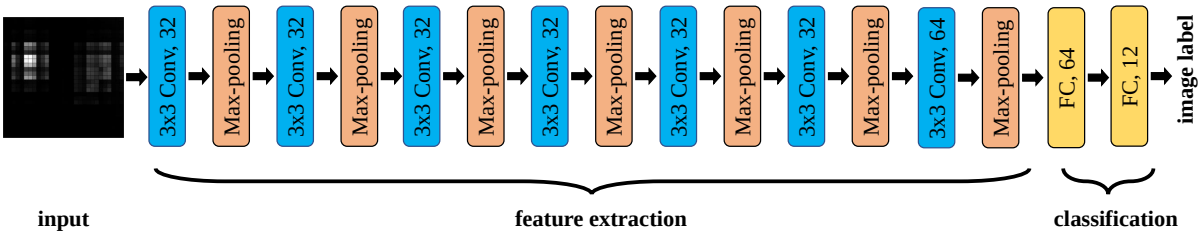


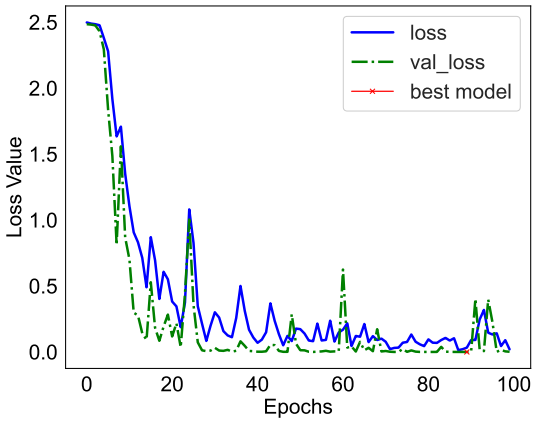
Figure 3.9: Increment of the fat tissues in the dataset breast models

.

input impression is a grayscale of dimensions 30 × 30. Seven 3×3 convolutional neural network blocks, each followed by a rectified linear unit (ReLU) and a 2 × 2 max pooling with stride 1 for downsampling compose the feature extraction part of the classifier. The last convolutional layer applies 64 filters, while other layers use 32 filters. No padding was used in this architecture. The features are then flattened and passed to fully connected layers with 64 nodes. A dropout with a rate of 0.5 is applied for regularization. We finally added the last fully connected layer with 12 nodes, which represent the number of classes,



(a)



(b)

Figure 3.10: (a) Deep learning architecture composed of seven convolutional neural networks and two fully connected layers. (b) Graph of loss function's values for training and validation sets over 100 epochs. The model with the least validation loss is marked with x and used for testing purposes.

followed by a softmax activation function to predict image labels.

We ran 144 simulation scenarios and obtained impressions from different models having different tumor sizes and locations. By changing the percentage of the fat tissue inside the breast model, we simulated different breast models ranging from extremely dense to fatty. In this work, we have used 12 different models, wherein tumor samples of three different dimensions were placed in four distinct locations inside the diverse breast models. Then, impressions obtained by each simulation scenario generated a dataset containing twelve classes, as shown in TABLE 3.3. The data was divided into training (66%), validation (17%), and test (17%). A total number of 100 epochs with a batch size of four was run to

Table 3.3: Size and location of the tumors for different classes

Class Name	Size	Location
Class A	10 mm	C_{t_1}
Class B	10 mm	C_{t_2}
Class C	10 mm	C_{t_3}
Class D	10 mm	C_{t_4}
Class E	7.5 mm	C_{t_1}
Class F	7.5 mm	C_{t_2}
Class G	7.5 mm	C_{t_3}
Class H	7.5 mm	C_{t_4}
Class I	5 mm	C_{t_1}
Class J	5 mm	C_{t_2}
Class K	5 mm	C_{t_3}
Class L	5 mm	C_{t_4}

train the architecture. The model's loss function on the training and validation cohorts are illustrated in Fig. 3.10(b), where the best model was saved based on the validation loss and used for testing purposes. We used an Adam optimizer with a learning rate of 10^{-3} and a categorical cross entropy as the cost function. Sheer, zoom and rotational augmentations were used to enhance the model's generalizability. We used a t-SNE dimensionality reduction to visualize different classes in two dimensions only. Fig. 3.11(a) shows the results of the training data. It is seen that all of the twelve classes are distinctly separated from each other, indicating that the model successfully captured the critical features in the images based on their classes. The obtained F1-score and confusion matrix additionally resulted in 100% accuracy for all twelve classes, thereby confirming that our introduced model successfully distinguishes between classes. We further employed a decision tree model to compare its accuracy with that of our deep learning model. For this purpose, a histogram of gradients (HOG) approach with 12 bins as orientations is employed to extract the im-

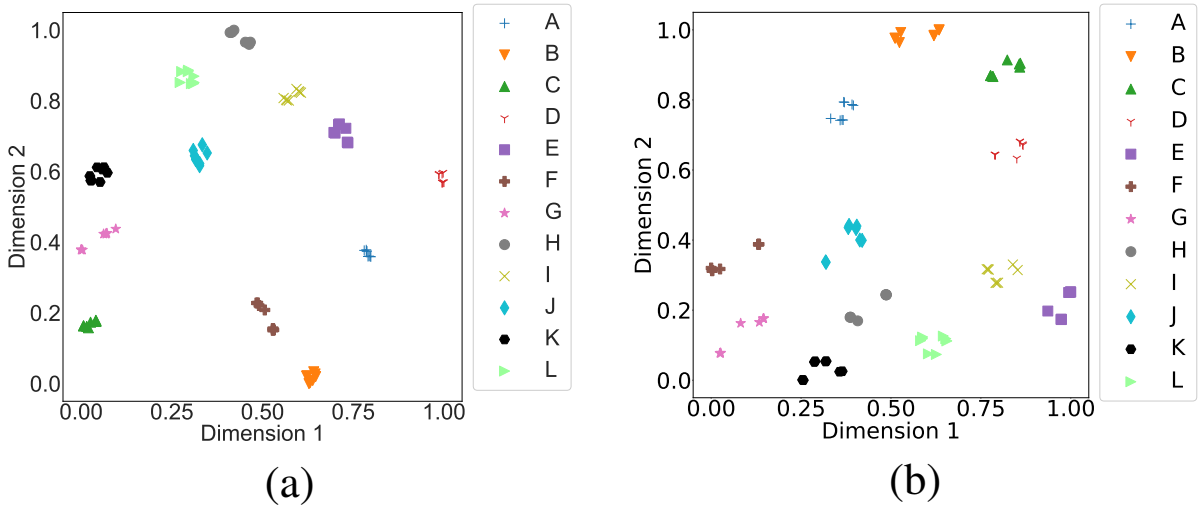


Figure 3.11: t-SNE visualization of the training data for twelve classes shown in TABLE 3.3. (a) Based on the features extracted from the deep learning architecture (b) Based on the HOG features.

ages' features. The accuracy achieved amounts to 75%, as opposed to the perfect accuracy acquired by the deep learning algorithm. The t-SNE visualization of the extracted features using HOG is illustrated in Fig. 3.11(b). It is evident that the t-SNE visualization of features generated by the deep learning implementation demonstrates a remarkable level of proximity among features belonging to different classes. This proximity suggests that the deep CNN effectively encodes essential patterns and distinctive characteristics, enabling it to return similar features for nearly all classes. On the contrary, the t-SNE representation of features obtained from the HOG algorithm exhibits a noticeable difference. The points corresponding to a specific class are notably more dispersed. This dispersion indicates that the HOG-based features may not be as effective in capturing and preserving the inherent relationships between samples belonging to the same class.

Removing the need for manual labels generated by human experts, we employed a convolutional autoencoder that learns a low-dimensional representation of input images acquired from microwave impressions by reconstruction of it. Such an algorithm requires no human supervision, hence referred to as an unsupervised process. Fig. 3.12a shows the entire designed DL architecture. The network is composed of the encoder, latent space, and decoder sections. The encoder part takes the mammogram images in RGB format, each with a 30×30 dimension, and passes them through eight convolutional layers, the first

three layers with 16 filters each, followed by another five layers with 32 filters each. The latent space applies a convolutional layer with 32 filters. Ultimately, the decoder processes the results obtained from the latent space through five successive layers of transposed convolutional (each containing 32 filters), followed by another three transposed convolutional layers (each with 16 filters). All layers are accompanied by a rectified linear unit (RLU) and "Same" padding. We trained the network by running a total number of 1000 epochs with a batch size of 4, the mean squared error as the cost function, and using Adam optimizer with a learning rate of 10^{-4}.

3.6 Deep Feature Learning for Microwave Mammography With Convolutional Autoencoders

Removing the need for manual labels generated by human experts, we employed a convolutional autoencoder that learns a low-dimensional representation of input images acquired from microwave impressions by reconstruction of it. Such an algorithm requires no human supervision, hence referred to as an unsupervised process. Fig. 3.12a shows the entire designed DL architecture. The network is composed of the encoder, latent space, and decoder sections. The encoder part takes the mammogram images in RGB format, each with a 30×30 dimension, and passes them through eight convolutional layers, the first three layers with 16 filters each, followed by another five layers with 32 filters each. The latent space applies a convolutional layer with 32 filters. Ultimately, the decoder processes the results obtained from the latent space through five successive layers of transposed convolutional (each containing 32 filters), followed by another three transposed convolutional layers (each with 16 filters). All layers are accompanied by a rectified linear unit (RLU) and "Same" padding. We trained the network by running a total number of 1000 epochs with a batch size of 4, the mean squared error as the cost function, and using Adam optimizer with a learning rate of 10^{-4}.

Fig. 3.12 shows an example of the input image followed by its reconstructed pair. It is visually seen that the network has performed successfully in creating an output, Fig. 3.12c, similar to the input, Fig. 3.12b. To evaluate the model's accuracy quantitatively, we flattened the latent space output and used the acquired vector to categorize images using a Gaussian Mixture Model (GMM). The GMM with 12 components has an ARS, a metric to measure clusters' similarities, of 91.18%. Fig. 3.13 reveals the model's output on a UMAP two-dimensional space, where each point represents an image. It is seen that the images are distinctly classified into two 12 groups. While nine images of class 0 are mixed with

those of class 9, all other images were correctly grouped by the model, each containing images of the same class.

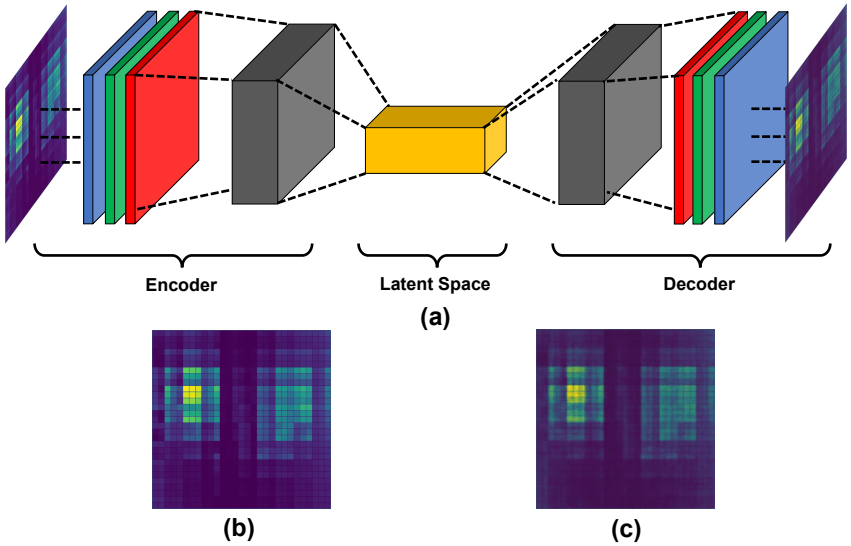


Figure 3.12: Auto-encoder network composed of encoder, latent space, and decoder sections. (a) Complete network schematic, (b) Input image, (v) Reconstructed output obtained by the designed auto-encoder model.

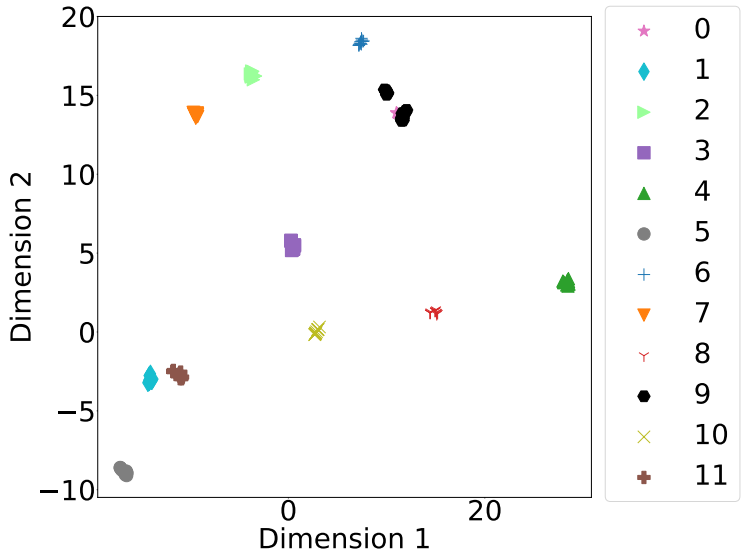


Figure 3.13: UMAP visualization of the training data for all twelve classes belonging to various tumor sizes and locations

3.7 The Proposed Prototype Implementation

Fig. 3.14 shows our full proposed mammography system setup in clinical investigations. The electrically small antenna (ESA) is fed by a CW signal at the desired frequency (200 MHz). Because ESAs are very inefficient radiators, only a small portion of the power from the signal generator will be radiated. The radiated power can be increased by employing a power amplifier. The radiated low-frequency electromagnetic waves will penetrate into the female breast, and after interaction with the female breast constituents, the power incident on the metasurface will be recorded using a spectrum analyzer or a power meter. By recording the power from each unitcell, an impression (or power map) will be obtained for the breast.

To validate the concept, the metasurface will be built using a 10×10 array of unitcells, where each unit cell is 1 cm $\times$ 1 cm. The metasurface should incorporate sufficient number of unitcells (pixels) to provide sufficient resolution to capture small anomalies inside the female breast. It is also possible that we use a smaller array size (i.e. 5×5) to reduce the complexity of the circuit, but then, we need to fully scan the lower side of the breast by moving the metasurface, which adds the mechanical complexity of the system.

The size of the metasurface array is adjustable and can be scaled to accommodate variations in breast size. While a 10 cm $\times$ 10 cm array was used in this work, larger arrays can be designed to match the average cross-sectional dimensions of the uncompressed breast, typically ranging from 11 cm to 14 cm. Increasing the number of unit cells not only allows for full coverage but also improves the approximation of an infinite periodic boundary, which enhances the electromagnetic response of the metasurface.

It is also important to recognize that the unit cells located near the edges of the metasurface may not perform as effectively as those near the center due to edge effects and weaker coupling. For this reason, these peripheral cells are typically excluded from the final imaging process to maintain reconstruction accuracy.

Given the substantial thickness of the intended metasurface (4 cm), fabricating it poses some challenges. The CNC machines available in the market are typically designed for thinner materials (usually up to 6 mm). To overcome this limitation, our proposed method involves stacking boards and assembling the top and bottom layouts on their respective sides.

For the initial trials, our plan involves utilizing artificial models, like a gel containing an inclusion with varying permittivity, to serve as the object under examination. However, regarding the female breast positioning in real-world clinical setup, the upper and lower sides of the breast will be slightly pressed (see Fig. 3.3 (d)). Thus, in the z coordinate, we

will not encounter any challenge in adjusting the position. In the x and y directions, it is important that the left and right breasts are positioned identically with respect to their corresponding coordinate system reference. This can be possible by having the woman under test to lie in prone position (see Fig. 3.14).

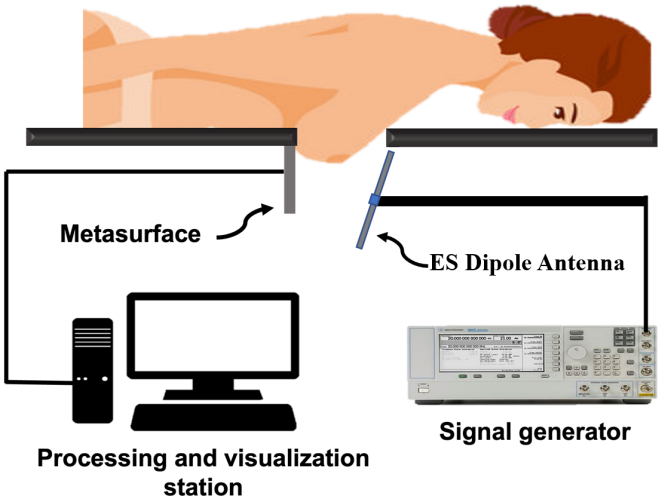


Figure 3.14: Mammography system setup

Chapter 4

Source Optimization for Enhanced Imaging Performance in LFEMF Modality

4.1 Introduction

In Chapter 4, we examine how the choice of electromagnetic source influences the imaging performance of the proposed Low-Frequency Electromagnetic Microwave Frequency (LFEMF) modality. This analysis focuses on assessing different types of radiating sources and their respective impacts on key imaging metrics such as spatial resolution, field penetration, and sensitivity to dielectric contrasts within biological tissue. The primary electromagnetic sources evaluated are electric dipole antennas and magnetic dipole antennas, each offering distinct electromagnetic field distributions and interaction characteristics with tissue.

Our simulations and experimental studies consistently show that magnetic dipole antennas—due to their ability to generate concentrated magnetic fields—deliver superior performance in detecting subsurface anomalies, particularly in complex breast tissue environments. These antennas provide better depth penetration and enhanced contrast in areas with dielectric variation, making them more effective for early-stage breast cancer detection.

Building on these findings, we introduce a loop-array transmitter specifically designed to capitalize on the strengths of magnetic field excitation. This transmitter consists of a

structured array of conductive loops, carefully positioned to generate a spatially uniform magnetic field across the imaging region. The design ensures efficient coupling of magnetic energy into the tissue, which enhances sensitivity and improves the consistency of the imaging data.

We fabricate and integrate the loop-array transmitter into the LFEMF imaging system and validate its performance through a series of controlled laboratory experiments. These include phantom studies that replicate tissue properties and initial tests on biological samples. The experimental results confirm the effectiveness of the loop-array approach, demonstrating improved image uniformity and anomaly detectability, and highlighting its potential as a core component of a clinically viable LFEMF-based breast imaging system.

4.2 Investigation of Fundamental Electromagnetic Excitation Sources

In this section, we employ low-frequency electromagnetic energy to probe deep into body tissues, leveraging its strong penetration capabilities to achieve high contrast in the interior regions of the breast. This enhanced contrast is critical for identifying subtle dielectric variations associated with potential tumors or anomalies that may not be detectable with higher-frequency imaging techniques.

The first near-field excitation source utilized in this study is an electrically small dipole antenna with a physical length of 150 mm. To ensure efficient operation at the desired frequency, we integrate a matching network consisting of a series-connected inductor. This network tunes the antenna to resonate at 200 MHz, a frequency selected for its favorable trade-off between penetration depth and antenna compactness. Electrically small antennas, due to their physical dimensions being much smaller than the wavelength of operation, generally suffer from low efficiency and limited radiation capability. This inherent inefficiency poses a challenge when evaluating or utilizing such antennas in practical scenarios. To compensate for their weak radiation characteristics and to obtain meaningful results during numerical simulations, one effective approach is to artificially increase the input power through computational means. This allows for a clearer analysis of the antenna's behavior under enhanced excitation conditions. Similarly, in experimental setups, the radiated power can be improved by incorporating a power amplifier between the signal generator and the antenna. This configuration amplifies the input signal before it reaches the antenna, thereby increasing the overall transmitted power and partially mitigating the limitations caused by the antenna's small size.

In the imaging setup, a dipole antenna is positioned at a distance of 5 mm from the surface of the breast phantom to serve as the source of electromagnetic excitation. On the opposite side of the phantom, a monitoring plate is placed to capture the resulting electric field distribution as the waves propagate through the tissue. This configuration enables the evaluation of field interaction within the phantom. The complete experimental arrangement, including the dipole antenna and the monitoring plate, is illustrated in Figure 4.1.

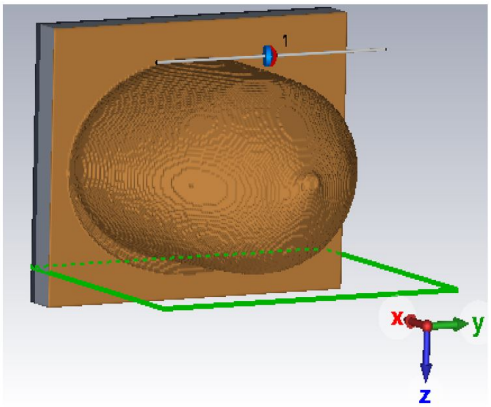


Figure 4.1: Schematic of the system setup featuring an electrically small dipole antenna.

As another fundamental excitation source, a circular loop antenna is employed to primarily generate a magnetic near-field, offering a magnetic-dominant near-field radiation, as we can consider a circular loop excitation source as a magnetic dipole. To ensure resonance at the desired frequency of 200 MHz—identical to that of the dipole configuration—a tuning capacitor is integrated into the feed structure of the loop. This frequency alignment allows for a direct and fair comparison between the two antenna types under consistent conditions. The loop antenna is placed 5 mm from the surface of the breast phantom, replicating the placement used in the dipole configuration. A monitoring plate is situated on the opposite side to record the resulting magnetic-dominant field distribution. The complete layout of this configuration, including both the loop antenna and the monitoring plate, is depicted in Fig. 4.2.

In the subsequent sections, a comparative analysis of the two excitation sources—the dipole and loop antennas—is conducted to evaluate their effectiveness in detecting breast tumors. By examining the spatial distribution of the electromagnetic fields and the resulting contrast levels produced by each configuration, we assess their respective capabilities in identifying localized dielectric anomalies within the breast phantom. This analysis provides

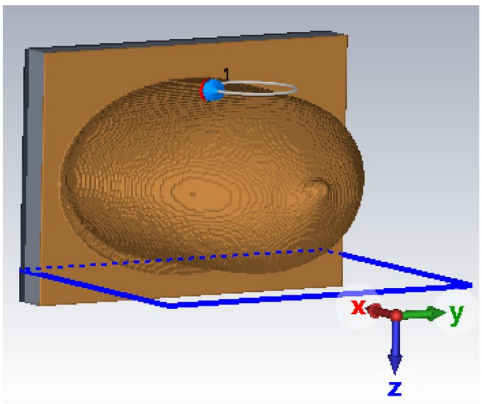


Figure 4.2: Schematic of the system setup featuring an electrically small circular loop antenna.

critical insight into the strengths and limitations of each approach, ultimately informing the selection of the most suitable excitation source for integration into low-frequency electromagnetic field (LFEMF)-based breast imaging systems.

To detect anomalies, both breasts are simultaneously stimulated, and the resulting electric or magnetic field amplitudes are recorded. Due to the natural symmetry between the left and right breasts, the data from one breast must be mirrored to align with the orientation of the other, as described in [107]. However, visually distinguishing healthy and tumorous tissues based solely on raw field images is challenging. To address this, a differentiation technique is employed: subtracting the field image of the tumorous breast from that of the healthy breast. This approach enhances contrast and emphasizes localized anomalies, thereby improving detectability.

We now present several examples involving tumors of varying positions, sizes, and material properties. First, a spherical Perfect Electric Conductor (PEC) tumor with an 8 mm radius is placed near the skin at the bottom of the breast. Fig. 4.3 shows the computed electric field amplitudes for both breasts when a dipole antenna is used as the excitation source. The subtraction method is applied to enhance contrast, and the resulting differential image is shown in Fig. 4.4. Similarly, Fig. 4.5 presents the magnetic field amplitudes obtained using a circular loop antenna, with the corresponding subtracted image shown in Fig. 4.6.

In a subsequent example, an 8 mm radius spherical tumor with realistic tissue properties—relative permittivity (ε_r) of 80 and conductivity (σ) of 3 S/m—is examined to

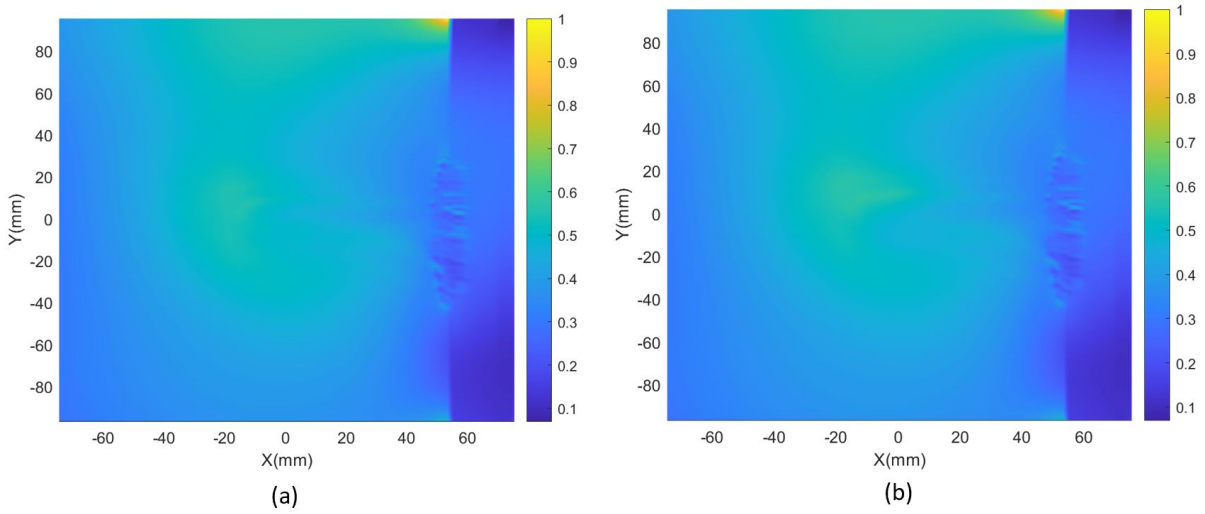


Figure 4.3: (a) Electric field amplitude calculated for (a) the healthy breast and (b) the breast with a tumor.

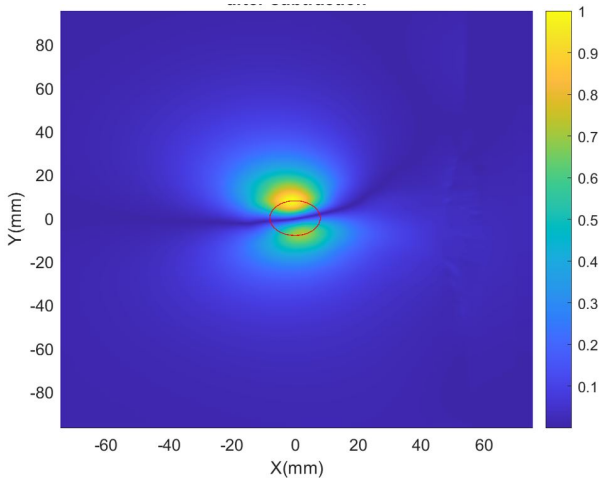


Figure 4.4: Captured image of a tumorous breast using electric field. Red circles indicating the borders of an 8 mm radius PEC tumor located at the bottom of the breast.

evaluate the system's performance under more biologically accurate conditions. The resulting subtracted images for both electric and magnetic field measurements are presented in Fig. 4.7.

Another case involves a smaller, 5 mm radius PEC tumor placed at the bottom of the

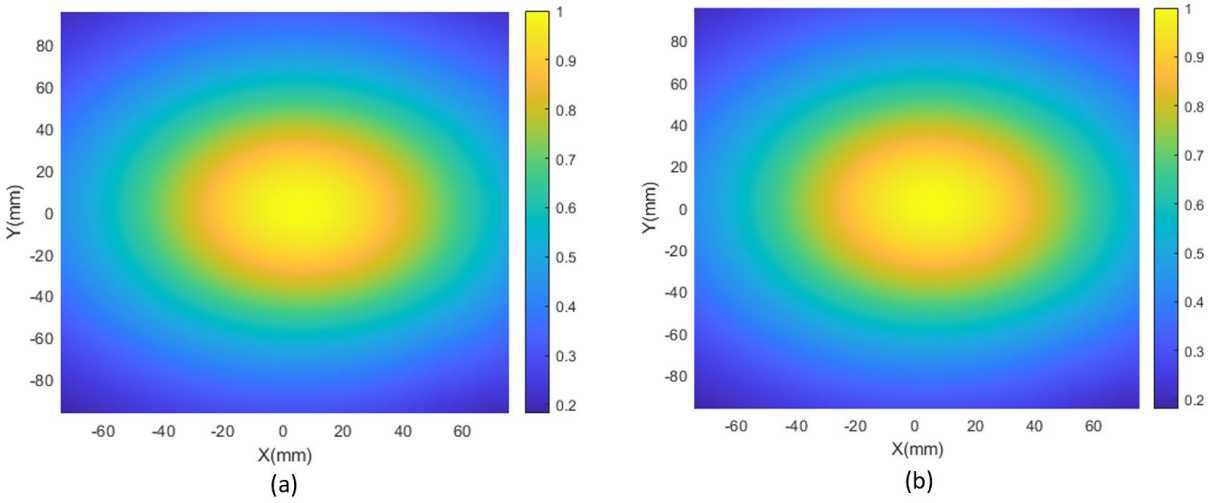


Figure 4.5: (a) Magnetic field amplitude calculated for the healthy breast and (b) magnetic field amplitude calculated for the breast with a tumor.

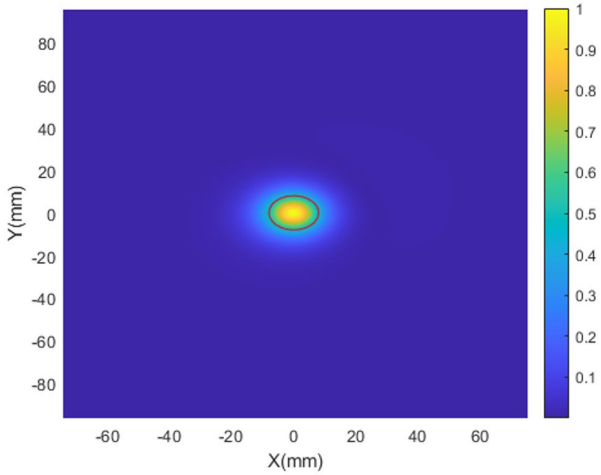


Figure 4.6: Captured image of a tumorous breast using magnetic fields. Red circles indicating the borders of an 8 mm radius PEC tumor located at the bottom of the breast.

breast near the skin. The outcome of the differential imaging for both field types is shown in Fig. 4.8.

Finally, we consider a scenario where a spherical PEC tumor with an 8 mm radius is located at the center of the breast tissue. Fig. 4.9 presents the differential images

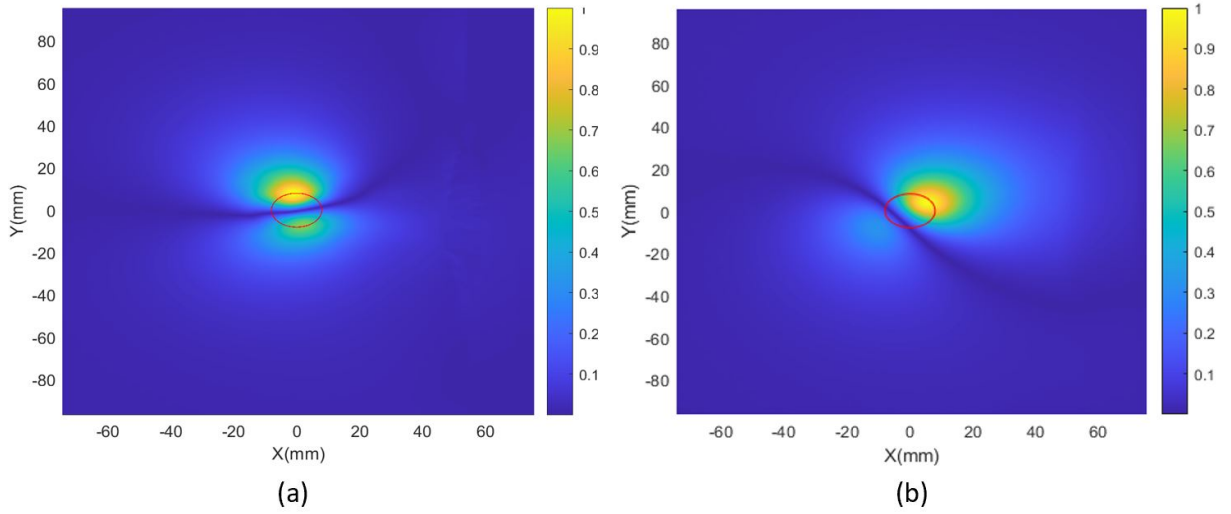


Figure 4.7: Captured images of a tumorous breast with red circles indicating the borders of an 8 mm radius spherical tumor with a permittivity of 80 and conductivity of 3, located at the bottom of the breast, using (a) the electric field and (b) the magnetic field.

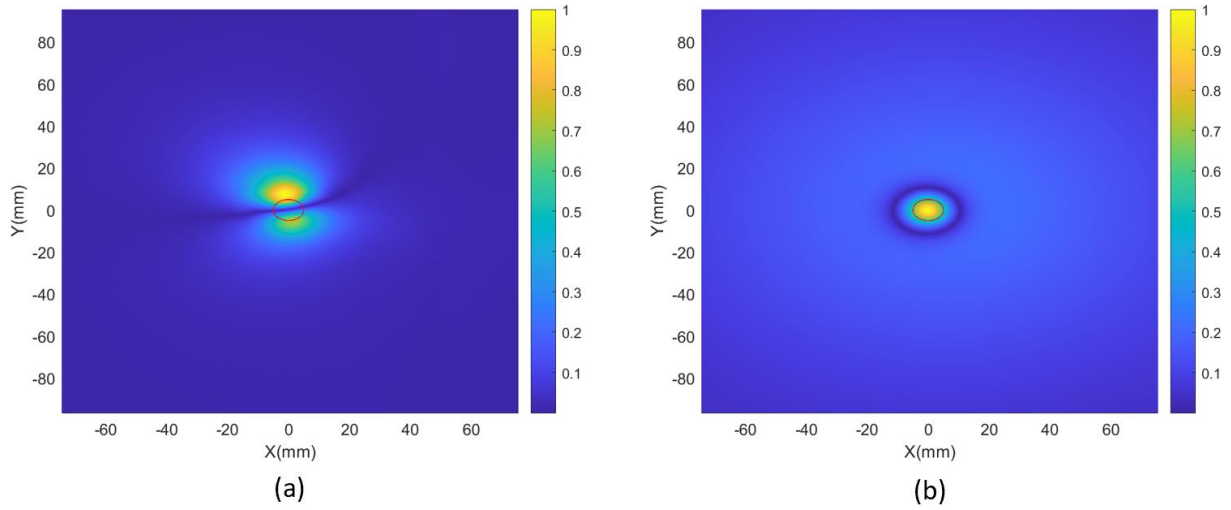


Figure 4.8: Captured images of a tumorous breast with red circles indicating the borders of an 5 mm radius spherical PEC tumor,located at the bottom of the breast, using (a) the electric field and (b) the magnetic field.

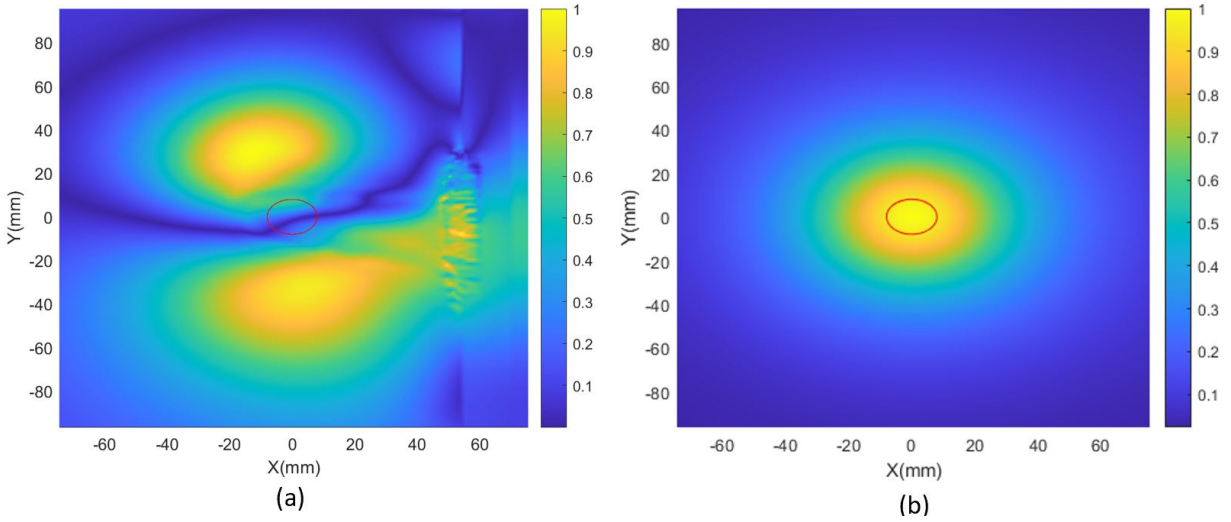


Figure 4.9: Captured images of a tumorous breast with red circles indicating the borders of an 8 mm radius spherical PEC tumor located in the middle of the breast using (a) the electric field and (b) the magnetic field.

derived from both electric and magnetic field data. It is evident from these results that while the magnetic field-based imaging effectively reveals the tumor's presence, the electric field-based approach fails to do so with comparable accuracy.

An important metric for evaluating the accuracy of tumor localization is the Positioning Error (PE), defined by equation 4.1. This parameter quantifies the spatial discrepancy between the reconstructed tumor center and its true location, providing a measure of the localization performance of the imaging system.

$$PE = ||P_{tumor} - P_{detected}|| \tag{4.1}$$

Here, P_{tumor} and $P_{detected}$ represent the actual and detected centers of the tumor, respectively. Table 1 illustrates this parameter for the analyzed examples, clearly showing that using the circular loop antenna and measuring the magnetic field yields more accurate tumor identification compared to using the dipole antenna and electric field measurements.

The field subtraction in this work was performed only on the magnitude of the field, not on the phase. This approach simplifies the imaging process and is sufficient for observing spatial anomalies in the electromagnetic response.

In the case of the electric dipole excitation, the minimum observed at the center of

Table 4.1: Comparison between the electric field generated by a dipole antenna and the magnetic field generated by a circular loop antenna.

Position, material and radius of tumor	Electric field (V/m)	Magnetic field strength (A/m)
Bottom, PEC, radius of 5	7.64	0.5
Bottom, PEC, radius of 8	8.63	0.5
Bottom, realistic, radius of 8	8.63	3.1
Middle, PEC, radius of 8	31.54	0.6

the tumor is a result of the interference patterns and scattering effects that occur in the near field. The strong interaction of the electric dipole's field with the high-permittivity anomaly can cause localized field cancellation, leading to the observed minimum in field magnitude.

Regarding the field distribution, Figure 4.3 shows the electric field amplitude generated by the electric dipole, while Figure 4.5 presents the magnetic field amplitude generated by the circular loop (magnetic dipole). These field patterns highlight how each type of excitation interacts differently with the tissue due to their distinct field structures and polarizations.

The healthy breast model used in the simulations is non-uniform (BI-RADS C), incorporating different layers and properties to better represent realistic biological tissues.

Finally, the appearance of a central minimum in Fig. 4.7 (b), which corresponds to magnetic excitation is attributed to positional inaccuracies caused by scattering effects. In magnetic field excitation, high-conductivity anomalies interact more strongly, and this increased interaction helps to reduce the positioning error compared to electric field excitation. Therefore, such positioning errors reflect complex wave-tissue interactions.

4.3 Design of Magnetic-field Dominant Excitation Source

A microstrip antenna consists of one or multiple metallic radiating elements mounted on the surface of a dielectric substrate, which itself is placed above a conductive ground plane. This configuration is engineered so that the electromagnetic waves radiate primarily in a direction perpendicular to the surface of the patch.

The radiating patch on the substrate can be designed in a variety of geometrical shapes, with square and rectangular configurations being the most common due to their simplicity.

However, depending on the design objectives—such as bandwidth enhancement, size reduction, or multi-band operation—other shapes like circular, elliptical, triangular, or custom contours may be used.

To deliver power to the radiating element and excite the antenna for radiation, several feeding techniques can be employed. These methods are selected based on factors such as ease of fabrication, impedance matching, and desired performance characteristics. The five primary feeding techniques are:

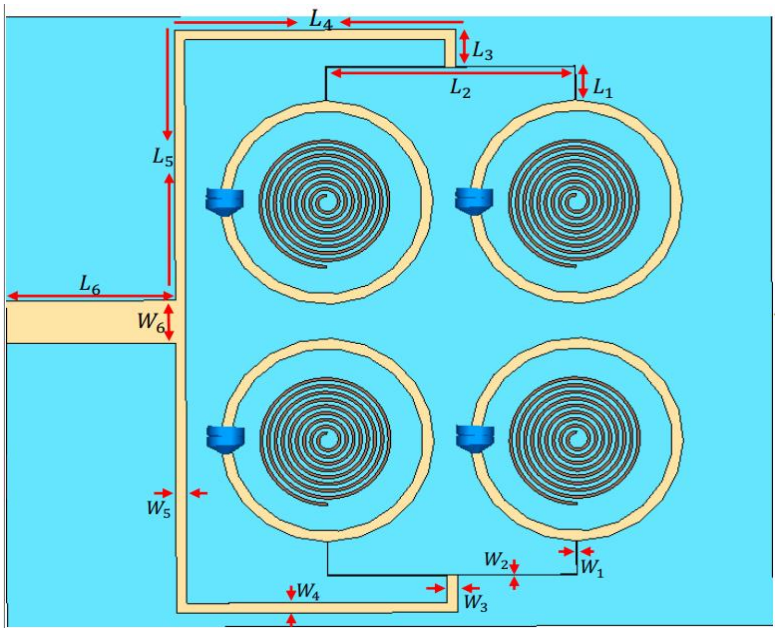
- Microstrip line feed, where a conducting strip on the same plane as the patch delivers energy directly;
- Inset feed, which adjusts the point of contact along the patch to improve impedance matching;
- Coaxial probe feed, where a coaxial cable penetrates the substrate to connect with the patch;
- Aperture-coupled feed, involving an opening in the ground plane to couple energy from a microstrip line located on the opposite side of the substrate;
- Proximity-coupled feed, which uses electromagnetic coupling between stacked dielectric layers for excitation without direct electrical contact.

Each feeding method offers its own advantages and trade-offs in terms of complexity, bandwidth, radiation efficiency, and manufacturing feasibility.

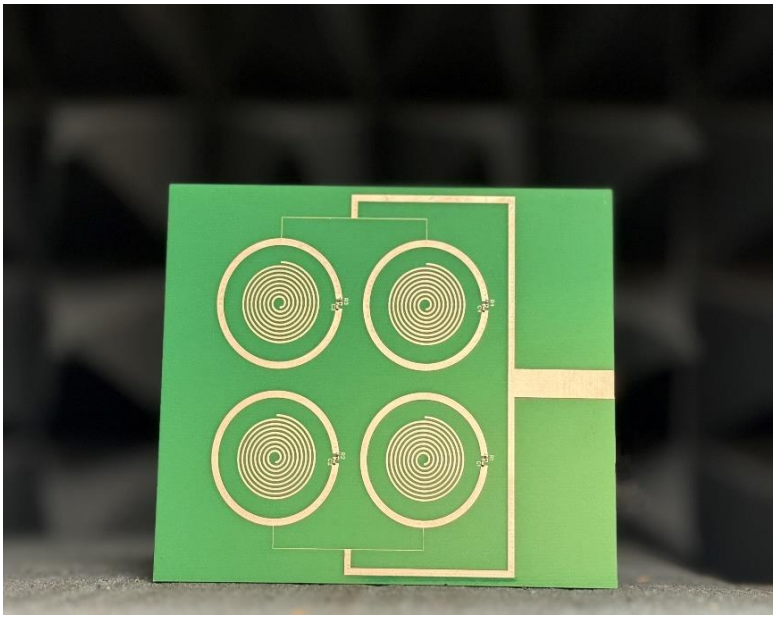
Table 4.2: Geometrical Features of Spiral Resonators

Parameter	**Value**
Inner diameter	1 mm
Strip spacing	1 mm
Strip thickness	0.035 mm
Strip width	0.4 mm
Number of turns	8

In this section, we go through the design process of a novel microstrip antenna intended to operate as a near-field electromagnetic transmitter. The antenna design is illustrated in Fig. 4.10(a). The core structural elements of the antenna, the ground plane, and the radiating elements are made of annealed copper to ensure excellent electrical conductivity and



(a)



(b)

Figure 4.10: (a) Design of the proposed transmitter antenna and (b) Photograph of the fabricated prototype of the transmitter antenna.

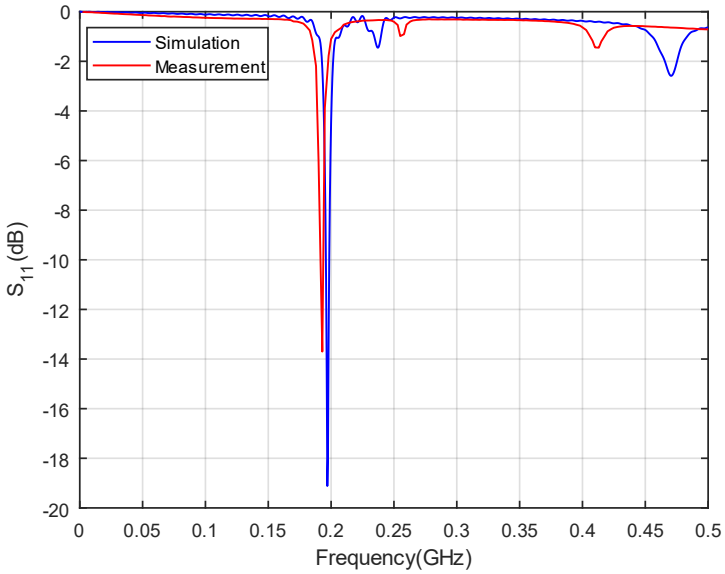


Figure 4.11: $|S_{11}|$ of the transmitter antenna.

minimize resistive losses. Between these copper layers is the substrate, which is composed of FR-4, a widely used dielectric material in printed circuit board technology. FR-4 has a relative permittivity of $\epsilon_r = 4.3$ and a loss tangent of $\tan(\delta) = 0.025$, making it a cost-effective choice that balances good performance and manufacturability. In fact, because of the low operating frequency, we do not require using low-loss, expensive materials such as Rogers boards.

The ground plane and the substrate have the same dimensions of 107.5 mm $\times$90 mm. The ground plane has a thickness of 35 μm, while the FR-4 substrate is significantly thicker at 3.2 mm. This relatively thick substrate helps maintain mechanical rigidity and supports effective near-field coupling.

The radiating component of the antenna consists of a 2×2 array of circular loop elements, each integrated with a spiral resonator. These loop resonator pairs are evenly spaced 35 mm apart to ensure consistent field distribution and minimize mutual interference. Each circular loop has an outer radius of 15 mm and an inner radius of 13.5 mm, with a copper trace thickness of 35 μm.

The primary function of circular loops is to serve as feed elements for the spiral resonators. Spiral resonators, while effective in concentrating electromagnetic energy at specific frequencies, require an efficient coupling mechanism to be viable for near-field imaging.

The circular loops fulfill this role by generating magnetic fields that are oriented perpendicular to the plane of the spiral resonators. This perpendicular-field alignment facilitates strong magnetic coupling, allowing the time-varying magnetic fields produced by the loops to induce currents within the conductors of the spiral resonators.

This electromagnetic interaction significantly improves the efficiency of energy transfer, thereby improving the overall performance of the antenna in imaging applications. By integrating the loops and resonators in this manner, the system is optimized to produce focused near-field patterns suitable for the detection of dielectric anomalies, such as breast tumors. The specific geometric parameters of the spiral resonators are summarized in Table 4.2.

The transmitter antenna is designed to operate at a resonant frequency of 200 MHz because it ensures deep penetration into breast tissue, as a result enabling the detection of anomalies located deeper within the tissue. To achieve the desired resonance frequency, a 13 pF capacitor and a 1Ω resistor are integrated into each loop antenna as part of the matching network. A microstrip line feed method is selected as the feeding network, designed to evenly distribute the signal to all resonating loop elements. The characteristic impedance of the microstrip line feed depends on several factors, including line width, substrate thickness, and the relative permittivity of the substrate material. By selecting a suitable characteristic impedance for the feeding network, optimal power transfer and minimal signal loss can be ensured. For a microstrip line, the characteristic impedance Z_0 can be approximated using the following equation:

$$Z_0 = \frac{60}{\sqrt{\epsilon_r}} ln(\frac{8h}{w} + \frac{w}{4h}), \tag{4.2}$$

where ϵ_r is the relative permittivity of the substrate material, h is the thickness of the dielectric substrate, and w is the width of the microstrip line line. The dimensions of the feeding network for the proposed transmitter antenna are listed in TABLE 4.3.

Overall, the proposed transmitter antenna is fed through a single feed point, which simplifies the design and reduces fabrication and system costs compared to more complex multi-antenna configurations. The integration of the circular loop array with spiral resonators enhances the generated magnetic field strength and spatial distribution, enabling effective electromagnetic coverage across the entire breast. This configuration improves detection sensitivity and eliminates the need for mechanical scanning, thereby increasing system efficiency and reducing operational complexity and cost.

The fabricated prototype of the proposed transmitter antenna is shown in Fig. 4.10(b). To characterize the antenna's performance, the magnitude of the reflection coefficient (S_{11})

Table 4.3: Design Parameters of the Feeding Network

Parameter	Value	Parameter	Value
L_1	5 mm	W_1	0.1 mm
L_2	35.10 mm	W_2	0.1 mm
L_3	4 mm	W_3	1.45 mm
L_4	39.45 mm	W_4	1.45 mm
L_5	39.80 mm	W_5	1.45 mm
L_6	23.78 mm	W_6	6.30 mm

was measured at the 50 Ω input terminal using an E5071C Vector Network Analyzer (VNA). A comparison of the simulated and measured $|S_{11}|$ values as a function of frequency is illustrated in Fig. 4.11.

While the simulated and experimental results are in close agreement, a slight discrepancy is observed in the resonant frequency. The simulation predicted a resonance at 200 MHz, whereas the fabricated antenna exhibited resonance at approximately 190 MHz. These deviations can be attributed to a range of practical factors, including manufacturing tolerances, slight variations in material properties (such as the dielectric constant and loss tangent of the substrate), and tolerances associated with the discrete components and assembly process. Collectively, these factors influence the observed performance and are typical in prototype development.

4.4 Metasurface Fabrication

The receiver metasurface antenna utilized in this chapter is based on the design introduced in the previous chapter, with several modifications implemented to enable experimental measurements using a spectrum analyzer. Specifically, an SMA connector has been integrated at the back of each unit cell to allow individual connection to the analyzer via a coaxial cable. This modification required replacing the original terminating resistor with the SMA connector. To preserve the intended load resistance, each SMA connector is terminated with a 470 Ω resistor, except for the one connected directly to the Vector Network Analyzer (VNA), which is left un-terminated to facilitate accurate signal acquisition. The proposed unit cell is shown Fig.4.12 with design parameters available in TABLE 4.4).

To simulate the infinite periodicity of the structure in the x and y directions, a perfect magnetic conductor (PMC) boundary condition was applied along the x-direction and a perfect electric conductor (PEC) boundary condition was applied along the y-direction.

The performance of the unit cell was evaluated by illuminating it and recording $|S_{11}|$ (see Fig.4.13), using a plane wave poert placed above the unitcell. Since the value of $|S_{11}|$ is below 10 dB at the resonance frequency, more than 90% of the incident power will be absorbed by the unit cell. Given that the low loss of the substrate material with a loss tangent of tan (δ) = 0.002, it ensures that the power is not lost due to dissipation.

By arranging the unit cells in a 10 $\times$ 10 configuration, a total of 100 pixels can be achieved in the final imaging system. The dimensions of the array layout, measuring 10.5 cm $\times$ 10.5 cm, were carefully chosen to correspond to the typical size of an average female breast (see Fig. 4.14).

To address the fabrication challenges posed by the 4 cm overall thickness of the designed metasurface—which exceeds the manufacturing limitations of standard PCB prototyping machines—the substrate was divided into eight individual layers. These include a top layout layer, a bottom layout layer, and six intermediate (middle) layers. The top and bottom layouts were fabricated using Rogers 4003C substrates, each with a thickness of 0.2 mm. The six middle layers were constructed using Rogers TMM 10i substrates, each with a thickness of 6.6 mm. In these layers, both the top and bottom copper surfaces were fully etched, and via locations were precisely drilled to accommodate the vertical interconnects. After preparation, all eight layers were carefully aligned and stacked with high precision to ensure consistent connectivity across the metasurface structure.

To establish vertical electrical connections, a total of 200 metallic rods were inserted through the pre-drilled vias across the stacked layers. The ends of these rods were polished to create flat, smooth surfaces, and then soldered to the via pads on the top and bottom layout layers, forming robust electrical joints. Following this, surface-mount (SMD) resistors were soldered to the bottom via pad of each unit cell to provide the necessary terminations. For the second via in each unit cell, an SMA connector was soldered, allowing connection to a spectrum analyzer for experimental measurements. Figure 4.15 presents perspective views of the fully assembled antenna structure of the metasurface.

4.5 System Evaluation

4.5.1 Realistic Numerical Phantom Models

In this section, we present a case study involving a realistic numerical breast phantom model. The selected model corresponds to an ACR Class 3 phantom, characterized by heterogeneously dense. This phantom was derived from MRI sagittal slices and imported

Table 4.4: Design Parameters of the unitcell

Parameter	Value	Parameter	Value
$L_{1,2,3,4}$	100 nH	R	470Ω
w_1	1.4 mm	w_2	0.6 mm
$g_{1,2}$	1 mm	l	9.5 mm
s_1	0.5 mm	s_2	1 mm
$d_{1,2}$	1.3 mm	t	4 cm

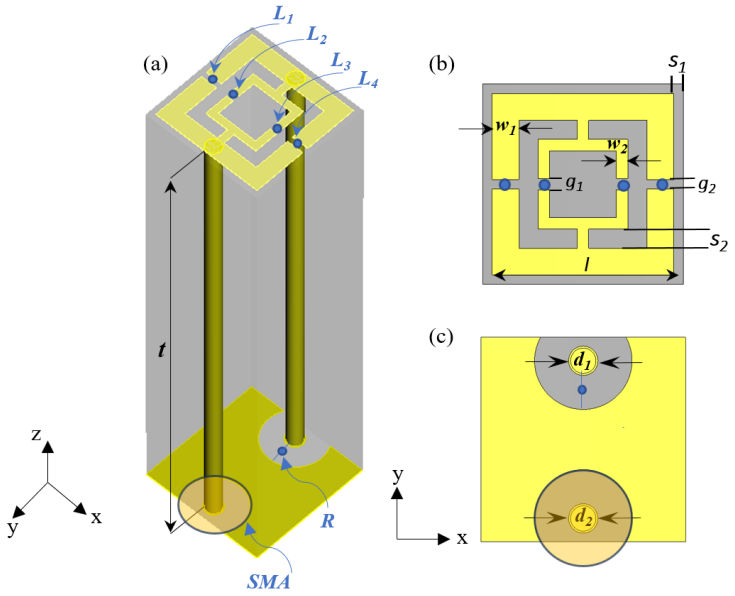


Figure 4.12: a) 3D view of the unitcell, (b) top view, and (c) bottom view.

into CST Microwave Studio, where it was reconstructed as a three-dimensional electromagnetic model. The phantom includes 100 distinct fibroglandular voxel configurations, each assigned specific electromagnetic properties based on tissue type. The model is validated for simulations in the frequency range of 0 to 20 GHz [108, 109].

The electromagnetic properties of the breast tissue components are characterized by their complex permittivity, specifically the dielectric constant ϵ_r. These properties are modeled using the single-pole Cole-Cole dispersion model, which is expressed by the following equation:

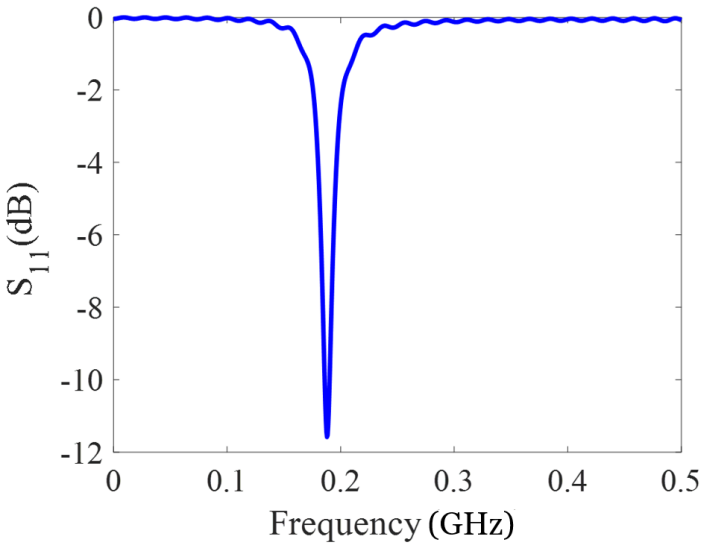


Figure 4.13: $|S_{11}|$ of the unitcell.

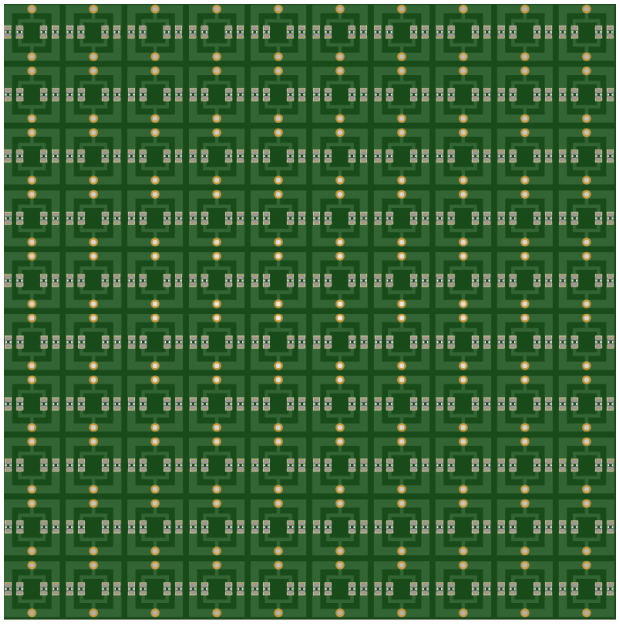
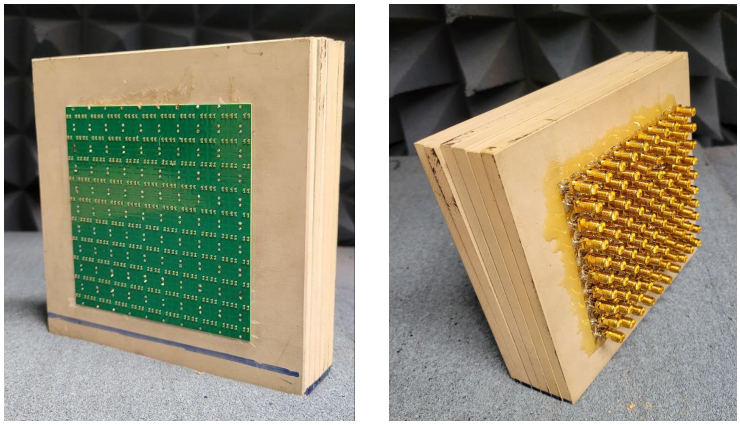


Figure 4.14: Top view (facing the breast) of the fabricated 10×10 unit cell array using FR-4.



(a) (b)

Figure 4.15: Photograph of the fabricated prototype of the metasurface: (a) the top view and (b) the back view.

$$\begin{aligned} \epsilon_c(\omega) &= \epsilon_c'(\omega) - j\epsilon_c''(\omega) \\ &= \epsilon_\infty + \frac{\Delta\epsilon_c}{1 + (j\omega\tau_c)^{1-\alpha}} + \frac{\sigma_s}{j\omega\epsilon_0} \end{aligned} \tag{4.3}$$

Table 4.5: Breast Tissue Parameter

Parameter\ Tissue	**Fibroglandular**	**Fat**
ϵ_∞	6.151	4.031
$\Delta\epsilon$	48.26	3.654
$\tau(ps)$	10.26	14.12
α	0.049	0.055
$\sigma_s(S/m)$	0.809	0.083

where ω is the angular frequency, $\epsilon_c'(\omega)$ represents the frequency-dependent real part of the dielectric constant, and $\epsilon_c''(\omega)$ denotes the frequency-dependent dielectric loss. This dielectric loss can be converted into the effective electrical conductivity using the relation $\sigma(\omega) = \omega\epsilon_0\epsilon_c''(\omega)$, where ϵ_0 is the permittivity of free space. The subscript c indicates the use of the Cole-Cole model, and ϵ_∞, $\Delta\epsilon_c$, σ_s, τ, and α are the empirical fitting parameters that characterize the dispersion behavior [110]. The values of these parameters for fibroglandular and fatty tissues are listed in Table 4.5.

At a frequency of 200 MHz, the relative permittivity and electrical conductivity of fibroglandular tissue were calculated using the Cole-Cole model (Equation 3) to be approximately 55 F/m and 0.82 S/m, respectively. For fatty tissue, the corresponding values were determined to be 7.68 F/m and 0.084 S/m. As noted in [105], the minimum dielectric contrast between tumorous and healthy tissue decreases to a ratio of approximately 2:1, highlighting the challenge of tumor detection in dense breast compositions.

The left and right breasts exhibit an enantiomorphic structure, which plays a crucial role in enhancing imaging sensitivity and reducing false-positive rates [107]. This anatomical symmetry allows one breast to serve as a reference for identifying abnormalities in the contralateral breast. Despite this overall symmetry, minor differences exist between the two breasts in terms of Breast Volume (BV) and Dense Volume (DV). The median relative asymmetry in BV and DV has been reported as 2.34% and 3.28%, respectively [106].

The probability of developing tumors simultaneously in both breasts is relatively low, estimated between 2% and 5%. Furthermore, the likelihood of tumors occurring at the same anatomical location in both breasts is exceedingly rare. These factors further support the use of one breast as a reliable reference when detecting and imaging abnormal tissue in the other breast.

As previously discussed, the anatomically accurate 3D numerical breast phantom models—derived from MRI sagittal slices and implemented in CST Microwave Studio—represent only a single breast (either left or right). However, due to the inherent enantiomorphic nature of the human breasts, it is possible to generate the contralateral (mirror) breast model for simulation and post-processing purposes by applying a reflection operation.

According to the method provided in [108, 109], each phantom model is accompanied by ASCII text files that contain two 3D arrays: $Mtype(i, j, k)$ and $Pval(i, j, k)$, both defined over a voxel grid of dimensions $[S_1, S_2, S_3]$. The array $Mtype(i, j, k)$ encodes the tissue type of each voxel, while $Pval(i, j, k)$ provides the corresponding dielectric property values.

To construct the enantiomer model, we perform a mirroring transformation along the second index (j), corresponding to the lateral axis of the phantom. Specifically, the columns of $Mtype$ are flipped as follows: $Mtype(:, 1, k)$ is exchanged with $Mtype(:, S_2, k)$, $Mtype(:, 2, k)$ is exchanged with $Mtype(:, S_2 - 1, k)$, and so on, until the midpoint $M = S_2/2$ is reached. This operation is applied across all slices k and all rows i of the 3D array. An identical transformation is performed on the $Pval$ array to maintain consistency in the dielectric properties.

Upon completion of the mirroring process, the modified arrays are converted into CST-compatible voxel files to enable electromagnetic simulation of the contralateral (mirrored) breast phantom.

The primary objective of the proposed detection method is to identify the presence and approximate location of tumors, rather than reconstructing their shapes, counting their number, or generating a detailed dielectric property map of the breast. A critical requirement for effective detection is the presence of a minimum contrast—particularly in terms of Dense Volume (DV) and Breast Volume (BV) asymmetry—between the anomalies and surrounding healthy tissue.

It is important to emphasize that this detection approach is applicable to anomalies with arbitrary configurations or shapes. Moreover, the method remains valid for a wide range of breast geometries with varying distributions of fibroglandular and fatty tissues, provided that the minimum dielectric contrast between tumorous and healthy constituents is preserved.

4.5.2 Simulation Results

To evaluate the effectiveness of the proposed detection setup in identifying breast tumors, a comprehensive simulation was conducted using CST Microwave Studio. The simulation incorporates the transmitter antenna, the metasurface, and a realistic numerical breast model. The selected breast model corresponds to a heterogeneously dense breast (ID: 080304, ACR classification: type C) [108, 109].

Figure 4.16 illustrates the complete simulation configuration, which integrates the transmitter antenna, metasurface, and the anatomically realistic breast phantom. The transmitter antenna is positioned in the near field of the breast model to ensure efficient delivery of electromagnetic energy into the tissue. Previous investigations [55] have demonstrated that operating in the near field can yield resolution surpassing the conventional Abbe diffraction limit. In such configurations, the electromagnetic field encompasses all polarization states, resulting in complex interactions with breast tissues and generating scattered fields enriched with diagnostic information.

The metasurface is placed on the opposite side of the breast and in close proximity, enabling it to capture the maximum scattered electromagnetic energy. Since the primary goal is to detect the presence and approximate location of tumors—rather than resolving their shapes or numbers—spherical tumor models with varying radii and positions were used in the simulation studies to systematically assess detection performance.

Figure 4.17(a) shows the numerical model of a healthy left breast, while Figure 4.17(b) presents the corresponding power absorbed by the metasurface. In contrast, Figure 4.18 illustrates the numerical model of a right breast with a spherical tumor composed of Perfect Electric Conductor (PEC), chosen to ensure a strong electromagnetic contrast with the

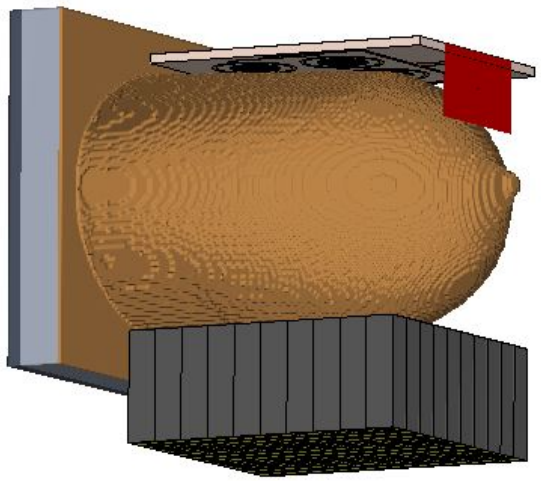


Figure 4.16: Simulation setup with the heterogeneously dense breast numerical phantom. The plate above the breast represents the antenna, while the bottom thick plate represents the metasurface.

surrounding healthy tissue. The tumor has a radius of 10 mm and is located near the lower region of the breast, in close proximity to the metasurface.

The electromagnetic power absorbed by the metasurface is recorded for both the left and right breasts of the same individual. It is important to note that female breasts exhibit enantiomeric symmetry; thus, their 2D electromagnetic impressions are spatially mirrored. To enable a direct comparison between the two sides, one of the absorbed power maps must be horizontally flipped.

The power absorption map of the tumorous breast, after applying the mirroring transformation, is shown in Figure 4.19. However, visual inspection alone is not sufficient to reliably identify the presence of a tumor when comparing the power distributions in Figure 4.19 and Figure 4.17(b), highlighting the need for automated differential analysis techniques.

To address the difficulty of identifying tumors based on the electromagnetic power distribution from a single breast scan, a differential subtraction technique is applied. This method involves subtracting the power absorption map of one breast from that of its enantiomer. Figure 4.20 displays the resulting image after applying this subtraction process. The location of the tumor is highlighted with a red circle, marking its boundary.

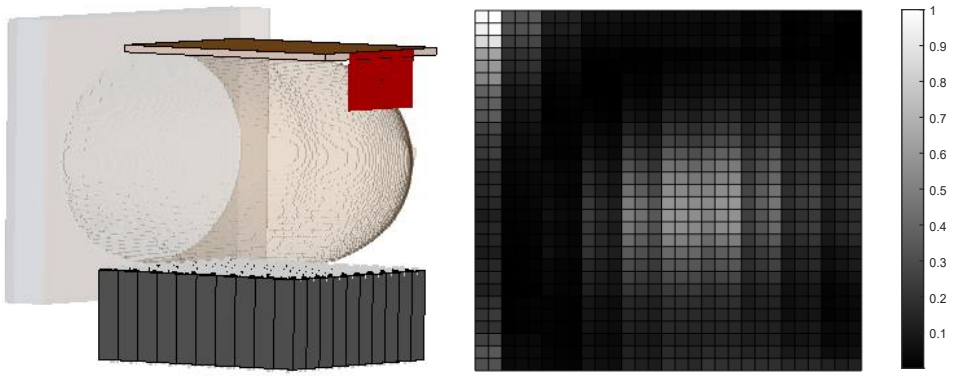


Figure 4.17: (a) Simulation model of the healthy breast and (b) recorded impression of the healthy breast.

The subtraction technique effectively suppresses common background features shared by both breasts, thereby enhancing the visibility of asymmetrical anomalies such as tumors. In this specific case, the detected contrast reaches a maximum of 0.4, which significantly exceeds the median relative asymmetries in Dense Volume (DV) and Breast Volume (BV)—2.34% and 3.28%, respectively. This notable contrast provides strong evidence confirming the presence of a tumor.

In the next phase of the study, the tumor location within the breast was varied to evaluate the robustness of the detection method. A spherical tumor with a radius of 10 mm, modeled as a Perfect Electric Conductor (PEC), was placed at four distinct positions. The centers of the tumors were located at coordinates (15 mm, −15 mm, 36 mm), (15 mm, 15 mm, 35 mm), (−15 mm, −15 mm, 35 mm), and (−15 mm, 15 mm, 36 mm), as shown in Figures 4.21(a)–(d).

The corresponding power distribution differences between the healthy and tumorous breasts for each tumor location are presented in Figures 4.21(e)–(h). These differential maps clearly demonstrate that the presence of the tumor results in localized power variations that exceed the median relative asymmetries in Breast Volume (BV) and Dense Volume (DV). This significant contrast confirms the effectiveness of the detection technique in identifying tumors across various locations within the breast.

To investigate the influence of tumor size on detection performance, a spherical PEC tumor was positioned at the bottom of the breast, in close proximity to the metasurface. While the tumor location was kept constant, four different tumor radii—8 mm, 7 mm, 6 mm, and 5 mm—were evaluated. The corresponding differences in power dissipation

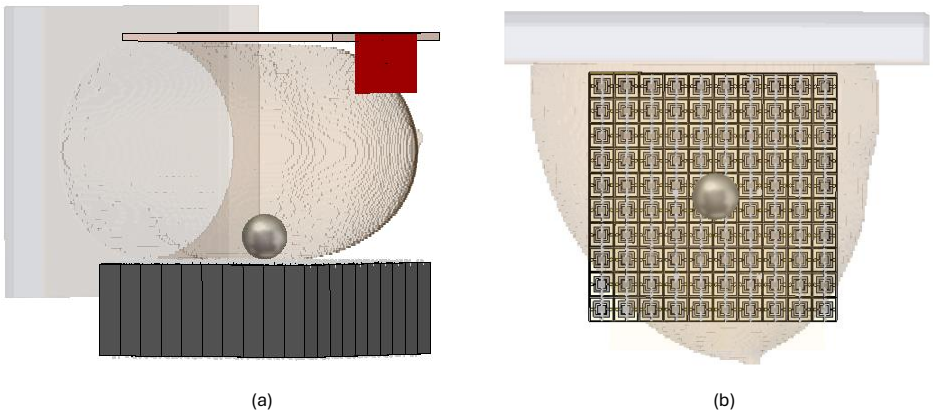


Figure 4.18: Simulation model of the tumorous breast: (a) the side view (b) the top view.

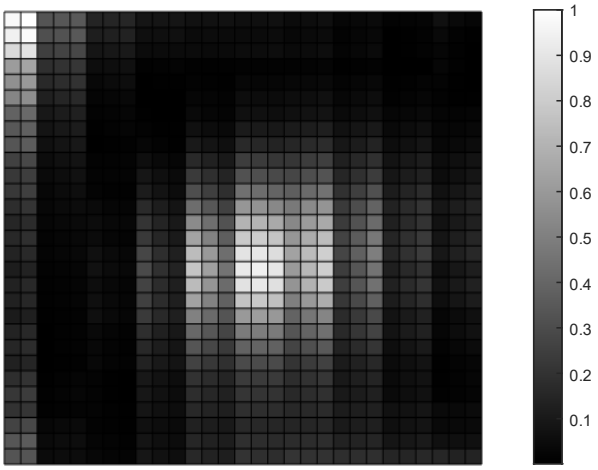


Figure 4.19: Recorded impression of the tumorous breast with a spherical PEC tumor of 10 mm radius.

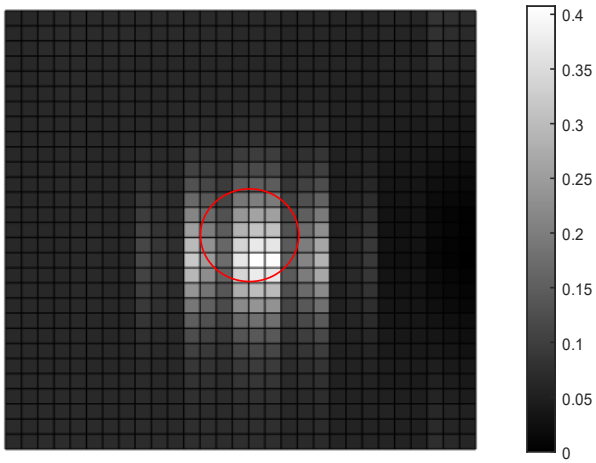


Figure 4.20: The difference in power distributions between the healthy and tumorous breast with a spherical PEC tumor of 10 mm radius.

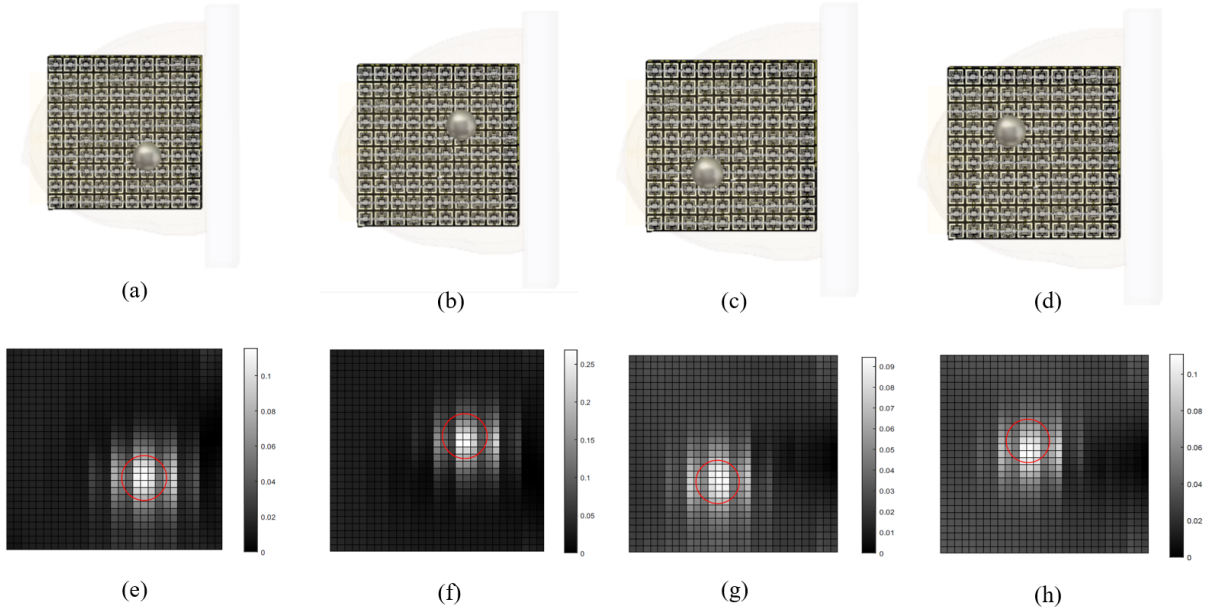


Figure 4.21: Tumorous breast model with a spherical PEC tumor (radius: 10 mm) positioned at four distinct coordinates: (a) (15 mm, -15 mm, 36 mm), (b) (15 mm, 15 mm, 35 mm), (c) (-15 mm, -15 mm, 35 mm), and (d) (-15 mm, 15 mm, 36 mm). The difference in power distributions between the healthy and tumorous breasts, corresponding to each tumor position, is shown in (e), (f), (g), and (h), respectively.

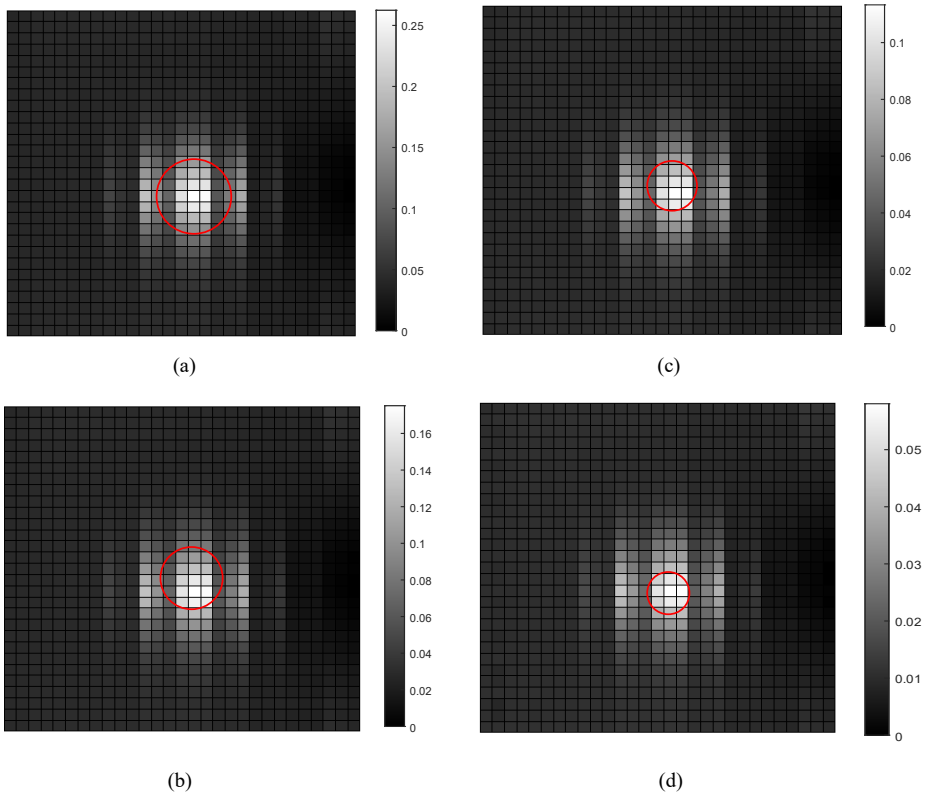


Figure 4.22: The difference in power distributions between the healthy and tumorous breasts with a spherical PEC tumor located at the bottom of the breast, with tumor radii of (a) 8 mm, (b) 7 mm, (c) 6 mm, and (d) 5 mm, respectively.

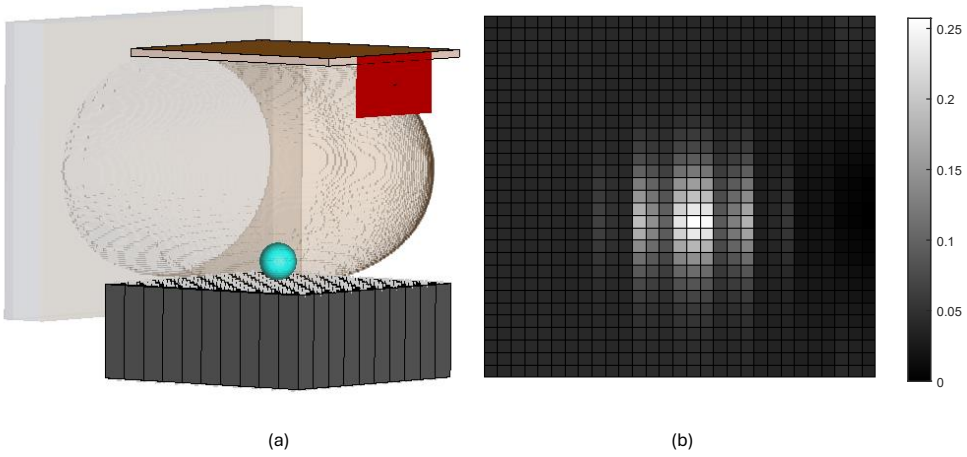


Figure 4.23: (a) Model of a tumorous breast with a tumor having a radius of 8mm, permittivity of 80, and conductivity of 3 S/m, and (b) the difference in power distributions between the healthy and tumorous breasts.

between healthy and tumorous breasts are illustrated in Figures 4.22(a)–(d).

As observed in Figure 4.22, the maximum contrast in each case surpasses the median asymmetry levels in both Breast Volume (BV) and Dense Volume (DV), effectively confirming the tumor's presence and location. Furthermore, the results indicate that the tumor with an 8 mm radius yields the highest contrast. The detected contrast progressively decreases with smaller tumor sizes, reflecting the diminishing impact on power dissipation as tumor volume is reduced.

In the final evaluation, the proposed detection modality was tested using a realistic tumor model. A spherical tumor with a radius of 8 mm, a permittivity of 80 F/m, and a conductivity of 3 S/m was positioned at the bottom of the breast, as shown in Figure 4.23(a).

The difference in power distributions between the healthy and tumorous breasts is presented in Figure 4.23(b). The maximum contrast observed was approximately 0.25, which exceeds the predefined detection threshold. This result confirms the presence of the tumor and demonstrates the effectiveness of the proposed detection setup in accurately identifying the tumor.

This setup is designed to test the system's ability to detect inclusions located deeper within the tissue, which is often more challenging due to greater electromagnetic attenuation. By positioning the anomaly farther from the source and receiver, the simulation

evaluates the system's effectiveness in deep tissue imaging.

4.5.3 Experimental Validation

Testing the proposed device on human female breasts is currently not feasible. Therefore, as a close alternative for validation purposes, non-human tissues were utilized. A 190 MHz signal (as described in Section 4.3) with a power level of 0 dBm was generated using a signal generator. This signal was fed to the microstrip antenna in series with an isolator and a 30 dB gain power amplifier. The isolator was used to prevent reflected signals from reaching the signal generator, while the power amplifier boosted the input power to the microstrip antenna from 0 dBm to 30 dBm.

The object under test (OUT) consisted of two slabs of beef meat, each 2 cm thick, compressed between two 2 mm thick silicon layers, which served to simulate the skin. The silicon material exhibits a relative permittivity of approximately 11.7 at low frequencies. This multilayered structure closely mimics the electromagnetic characteristics of breast tissue.

The OUT was placed between the microstrip antenna and the metasurface, as shown in Figure 4.24. The power absorbed by the metasurface unit cells was measured using a spectrum analyzer via a coaxial cable. One end of the cable was connected to the SMA connector on the metasurface, and the other end was connected to the spectrum analyzer (HP 8563E). This measurement process was repeated for all SMA connectors, and the collected power data was subsequently transferred to MATLAB for reconstructing the power distribution map.

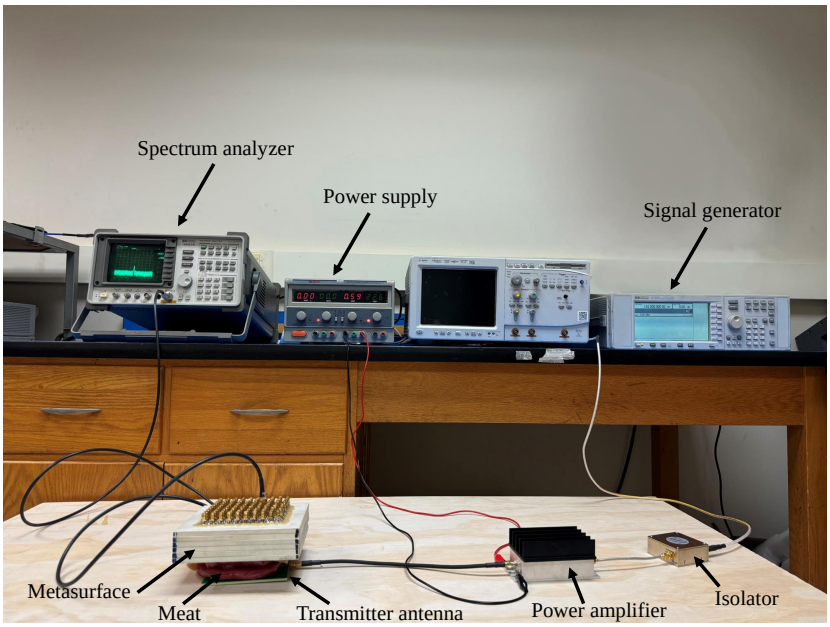
The experiments were conducted under two scenarios. In the first scenario, the power absorbed by each unit cell was measured without any inclusion in the OUT, representing the healthy model. In the second scenario, a metal inclusion with a diameter of 12 mm was placed in the OUT to simulate the presence of a tumor, and the power absorbed by each unit cell was measured. Throughout these experiments, all components of the setup, including the transmitter antenna, metasurface, and OUT, were maintained under identical conditions.

Assuming the center of the meat was positioned at the origin of the Cartesian coordinate system, the metal inclusion was located at $(0\text{ mm}, 0\text{ mm})$ in the x-y plane, situated at the top of the meat beneath the silicon layer. After measuring the power in both scenarios, the difference in power distribution was calculated by subtracting the power values obtained without the inclusion from those obtained with the inclusion. This differential power

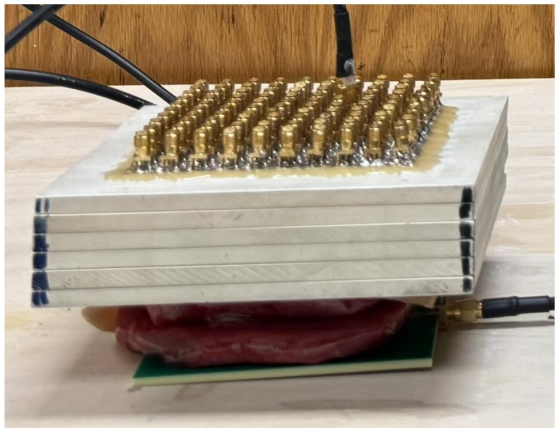
map was used to identify the location of the inclusion. The resulting power distribution differences are illustrated in Figure 4.25.

To further evaluate the system, the position of the embedded inclusion was varied within the x–y plane while still being located at the top of the meat beneath the silicon layer. The corresponding power distribution differences for these configurations are shown in Fig. 4.26. In both images (Figs. 4.25 and 4.26), the bright pixels represent the regions of maximum power difference, which correlate with the inclusion's location. This setup effectively detects both the presence and location of the inclusion. It is worth noting that similar experiments were performed with the inclusion placed at other locations, and the system consistently demonstrated its capability to detect both the presence and location of inclusions accurately.

While the work elaborated upon in the previous chapter validated our proposed concept, This chapter focused on creating a prototype to experimentally confirm our detection method's viability.



(a)



(b)

Figure 4.24: (a) Experimental setup for the detection modality. (b) OUT with the transmitter antenna and metasurface.

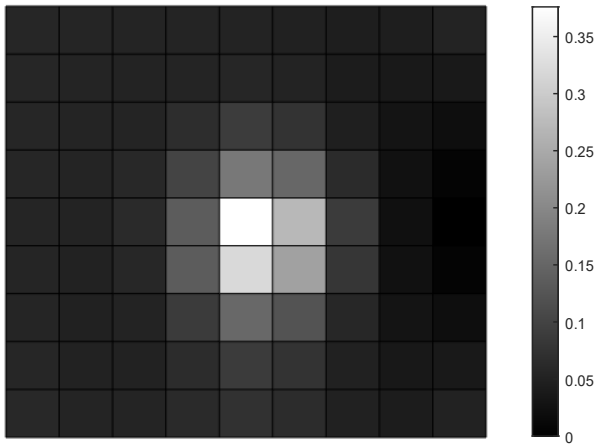


Figure 4.25: Difference in power distributions between the cases without the inclusion and with the inclusion positioned at (0 mm, 0 mm) in the x-y plane.

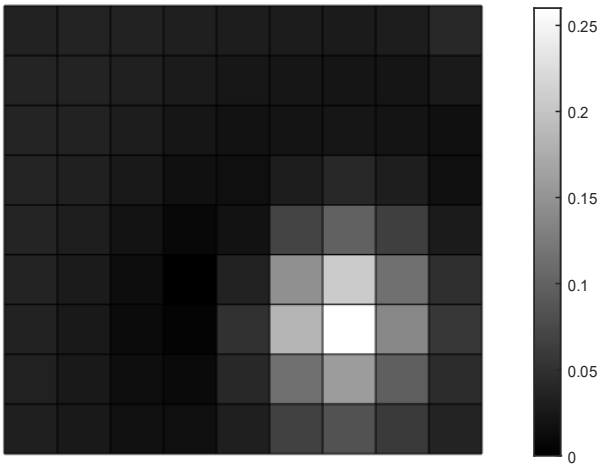


Figure 4.26: Difference in power distributions between the cases without the inclusion and with the inclusion positioned at the corner of the x-y plane.

Chapter 5

Design and Implementation of a Miniaturized Metasurface Receiver for Enhanced LFEMF Imaging

5.1 Introduction

In Chapter 5, we present the development and characterization of a novel metasurface-based sensor that demonstrates substantial advancements in pixel density, fabrication feasibility, measurement simplicity, and imaging performance. Specifically, the proposed design enables the integration of 900 pixels, a nine-fold increase compared to the 100 pixels achieved in the earlier design, all within the same compact 10 cm $\times$ 10 cm footprint. This enhancement in spatial resolution is particularly noteworthy, as it directly addresses the limitations of prior configurations constrained by coarse pixelation, thereby paving the way for higher-fidelity image reconstruction.

One of the key innovations in this metasurface antenna lies in the reduction of substrate thickness, which offers both performance and manufacturing advantages. The previous design relied on substrates that were several centimeters thick, primarily to support the electromagnetic resonance characteristics required for pixel functionality. However, such thicknesses introduce significant complications in the context of printed circuit board (PCB) fabrication, including high cost and incompatibility with production lines. In contrast, the proposed new design achieves equivalent or superior electromagnetic performance while utilizing a substrate that is only a few millimeters thick, aligning closely with industry-standard PCB materials. This shift not only facilitates easier and more scalable

manufacturing but also supports broader adoption and integration into practical imaging systems.

Moreover, the new design enables faster and more efficient data acquisition by addressing the limitations of the previous setup, which required repeatedly connecting and disconnecting SMA connectors to measure dissipated power. In contrast, the new approach involves simply measuring the voltage across the terminated components of each unit cell. This not only minimizes measurement errors, but also allows the entire data acquisition process to be automated and electronically controlled using a switching network and a microcontroller, greatly enhancing practicality and scalability of the imaging system setup.

5.2 Miniaturized Metasurface Design

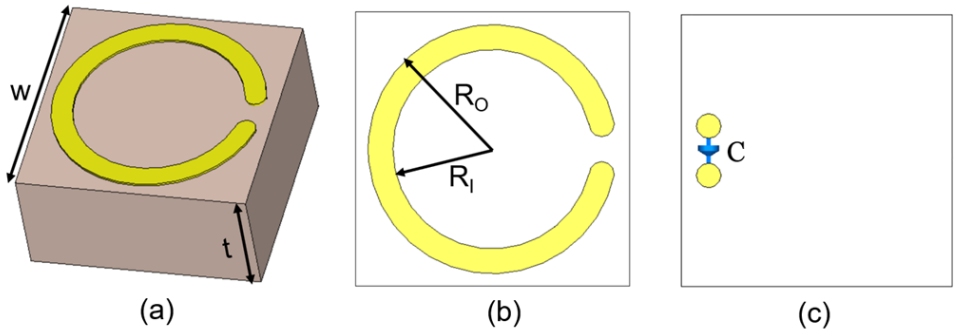


Figure 5.1: (a) Perspective view (b) top view, and (c) bottom view of the unitcell, where $w = 3.3$ mm, $t = 1.6$ mm, $R_O = 1.5$ mm, $R_I = 1.3$ mm, $C = 250$ pF.

.

The design of the metasurface film begins with the careful engineering of the unit cell, which functions as the fundamental building block of the entire electromagnetic structure. Each unit cell contributes to the film's overall electromagnetic response and imaging capability, and its dimensions directly impact both the resolution and practicality of the final system. A key objective in our design process is to minimize the physical size of each unit cell in order to maximize the number of cells per unit area. This approach allows us to significantly increase spatial resolution, which is essential for high-fidelity image reconstruction and precise localization of small features within a target.

However, this miniaturization task presents substantial challenges due to the low operating frequency of the system, which corresponds to a relatively long free-space wavelength

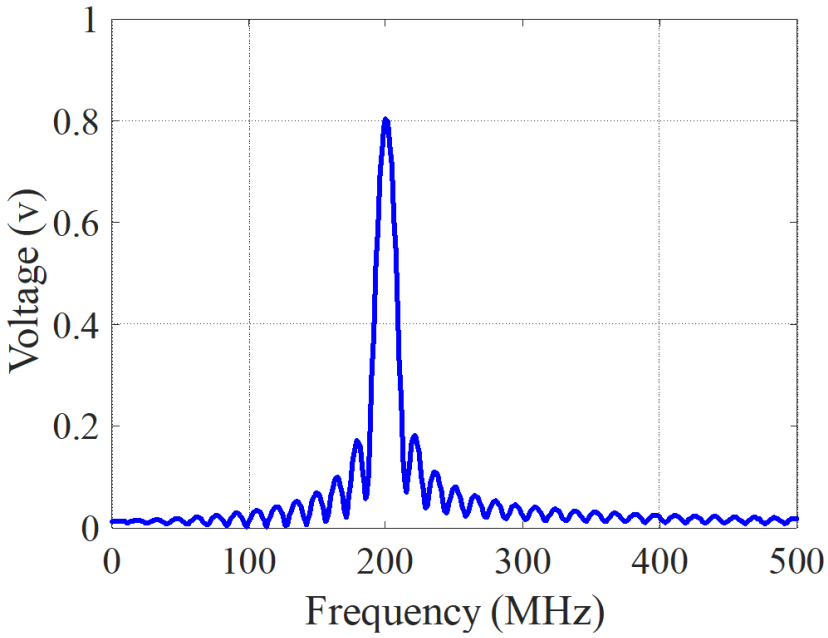


Figure 5.2: Voltage across the capacitor vs frequency graph

.

of approximately 1.5 meters. Under typical scaling rules for metamaterials and resonant structures, unit cell sizes are often designed as a fraction (e.g., 1/10 to 1/20) of the operational wavelength. Achieving sub-wavelength performance at such low frequencies within a compact physical area requires careful design optimization, material selection, and simulation.

Our target configuration consists of a 30×30 array of unit cells embedded within a $10\,\text{cm} \times 10\,\text{cm}$ metasurface film, resulting in an unit cell size of approximately 3.3 mm. Reaching this level of miniaturization is non-trivial, particularly when ensuring that each unit cell still maintains its intended electromagnetic behavior without significant coupling artifacts or parasitic losses.

The impact of this resolution is significant from an application standpoint. A spatial resolution of 3.3 mm implies the theoretical ability to detect anomalies—such as early-stage tumors—with a minimum characteristic size of around 3.3 mm. This capability is crucial for medical imaging applications, particularly in contexts such as breast cancer screening, where early detection of small, localized growths can dramatically improve patient outcomes. Moreover, achieving this resolution within such a compact and planar metasur-

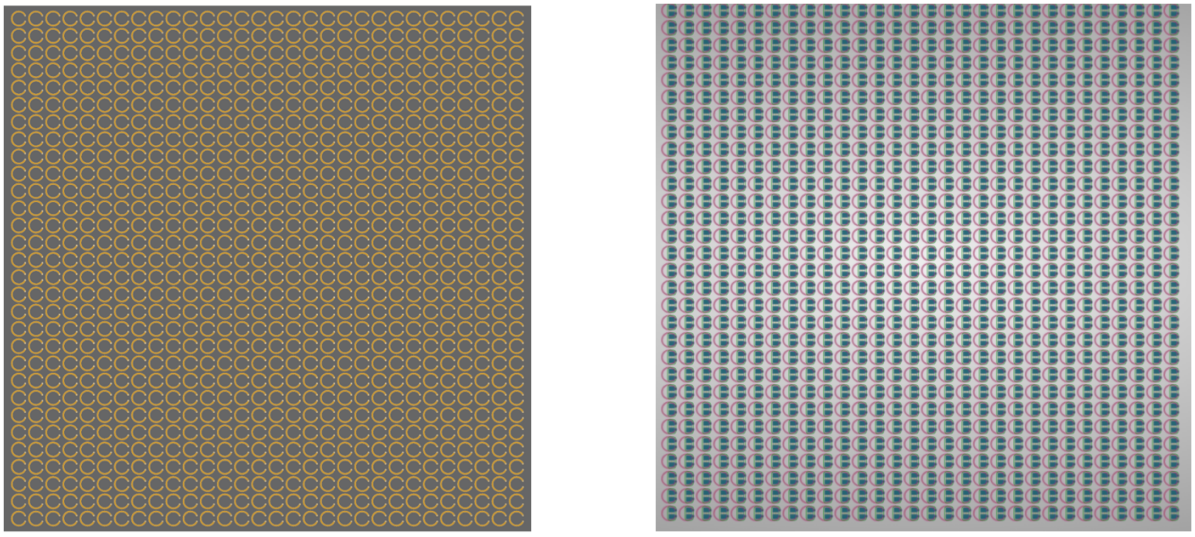


Figure 5.3: (a) Top view of the metasurface (b) bottom view of the metasurface
.

face design supports the development of portable, non-invasive, and potentially real-time imaging systems.

Minimizing the size of the unit cell inherently requires maximizing both the effective capacitance and inductance within the cell, as these parameters determine the unit cell's resonance frequency. To do so, we employed a split-ring resonator (SRR) structure on the top layer of the substrate to introduce inductance, while a capacitor pad was placed on the bottom layer. The capacitor pad is electrically connected to the split ring via two vertical interconnect accesses (vias), forming a compact and efficient two-layer LC resonator.

This multilayer configuration offers several advantages. First, it enables straightforward electrical access to the capacitor pads from the bottom layer during measurement and characterization, as illustrated in Fig. 5.1. Second, the inclusion of vias not only serves a mechanical connection purpose but also contributes additional inductance due to their vertical geometry and length. This increased inductance effectively lowers the resonance frequency of the unit cell, which is beneficial for maintaining compact geometry while operating at a low frequency.

The geometrical parameters of the unit cell were carefully optimized to balance miniaturization with performance. The outer and inner radii of the split ring were set to 1.5 mm

and 1.2 mm, respectively, ensuring that the ring remains symmetrically centered within the unit cell and providing sufficient trace width for current flow. The vias used to connect the layers were designed with a diameter of 0.3 mm, which matches the width of the metallic trace forming the ring to maintain impedance continuity and minimize current crowding.

The substrate material selected for this design was standard FR4, with a thickness of 1.6 mm—a common dimension readily available from commercial PCB fabrication services. While FR4 is known to exhibit relatively high dielectric loss at microwave and higher frequencies, its use in this context is justified by the low operational frequency of approximately 200 MHz, where dielectric losses are significantly less impactful. Consequently, FR4 provides a cost-effective and manufacturable solution without compromising performance in this frequency regime.

In summary, this carefully engineered two-layer unit cell design maximizes inductance and capacitance within a compact footprint, facilitates practical measurement access, and supports low-frequency operation with standard fabrication materials and methods.

To complete the resonant circuit within each unit cell, surface-mount device (SMD) capacitors with a nominal value of 250 pF were placed between the two vias located on the backside of the unit cell. These capacitors form the primary capacitive element in the LC resonator configuration, working in conjunction with the inductive split-ring structure on the top layer to establish the desired resonance behavior. The back surface of the substrate was entirely etched in the region surrounding the capacitor to allow magnetic flux to penetrate through the structure and induce an electromotive force (EMF) across the capacitor terminals. This configuration ensures efficient magnetic coupling and accurate voltage induction at the operating frequency.

The selection of the 250 pF capacitor value was the result of iterative tuning and simulation-based optimization, with the primary goal of achieving resonance at approximately 200 MHz. This value was found to provide the best trade-off between miniaturization, frequency stability, and component availability, while still supporting efficient energy transfer and maintaining a compact unit cell footprint.

To validate and optimize the electromagnetic behavior of the unit cell, full-wave simulations were conducted using CST Microwave Studio [97]. The simulation environment was carefully configured to reflect the periodic and infinite nature of the metasurface structure. Specifically, a *perfect magnetic conductor* (PMC) boundary condition was applied along the x-axis, and a *perfect electric conductor* (PEC) boundary condition was applied along the y-axis. This boundary setup mimics the behavior of an infinitely repeating array by enforcing field symmetry and periodicity, enabling accurate estimation of the unit cell's scattering parameters and resonance characteristics.

Once the unit cell design was finalized through simulation and experimental prototyping, the complete low-frequency electromagnetic film (LFEMF) was fabricated by assembling a two-dimensional array of the individual unit cells in a 30×30 grid (see Fig. 5.3). This tiling approach ensures consistent performance across the entire metasurface while preserving the sub-wavelength resolution necessary for high-fidelity imaging applications.

5.3 Simulation Results

In this section, we investigate the performance of the designed metasurface sensor through a series of numerical experiments. The simulation setup is illustrated in Fig. 5.4. It includes the transmitter antenna, a numerical phantom representing an ACR type-3 breast model (heterogeneously dense), and the receiver metasurface sensor. All components were placed within an open boundary condition to emulate a reflection-free, isolated medium that closely approximates free-space conditions and minimizes unwanted boundary reflections.

Following the completion of the simulation, the voltage across each capacitor located on the backside of the metasurface was recorded. These voltages were then assembled in MATLAB, with each value mapped to its corresponding spatial position on the metasurface. By arranging the data in this way, a two-dimensional image was reconstructed, representing the interaction between the electromagnetic waves and the internal constituents of the numerical phantom (voxels).

In Fig. 5.5, we present simulation results for two different scenarios. In the first scenario, we simulated the electromagnetic interaction with an ACR type-3 breast phantom (heterogeneously dense) to generate a reference image or baseline impression of the medium (see Fig. 5.5(a)). In the second scenario, we introduced a small inclusion into the same phantom and repeated the simulation under identical conditions to capture the new image impression (see Fig. 5.5(b)). The embedded anomaly is modeled as a perfect electric conductor (PEC) sphere with a radius of 10 mm.

Upon visual inspection, the difference between the two images is not readily apparent to the naked eye due to low contrast and subtle changes in the field distribution. To enhance the detectability of the anomaly, we performed a pixel-wise subtraction of the two images to highlight the spatial differences. The resulting differential image is shown in Fig. 5.6. As illustrated, the most significant changes between the two simulations are concentrated in the region surrounding the inclusion, which is marked with a circular indicator. This result demonstrates the system's sensitivity to localized anomalies and the effectiveness of image subtraction in improving contrast for anomaly detection.

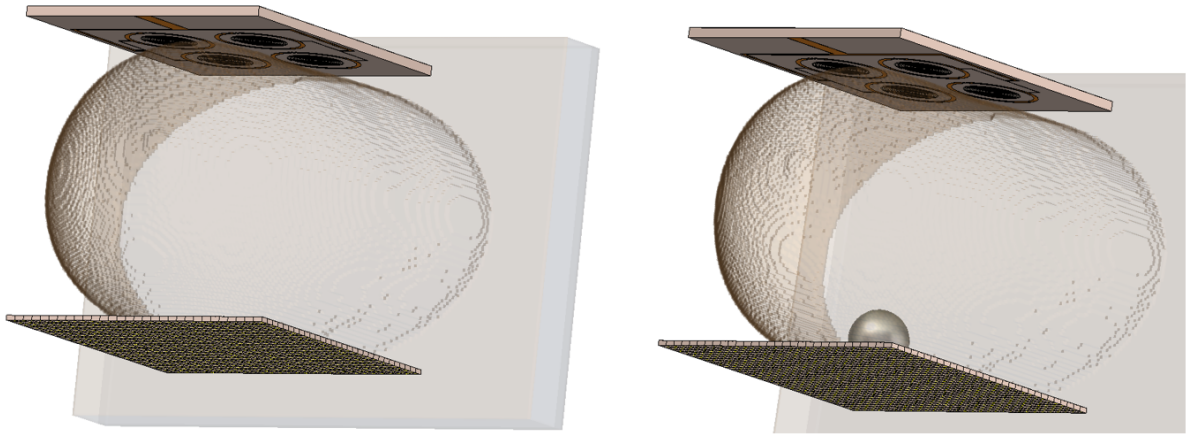


Figure 5.4: Simulation setup: (a) healthy phantom (b) phantom with inclusion

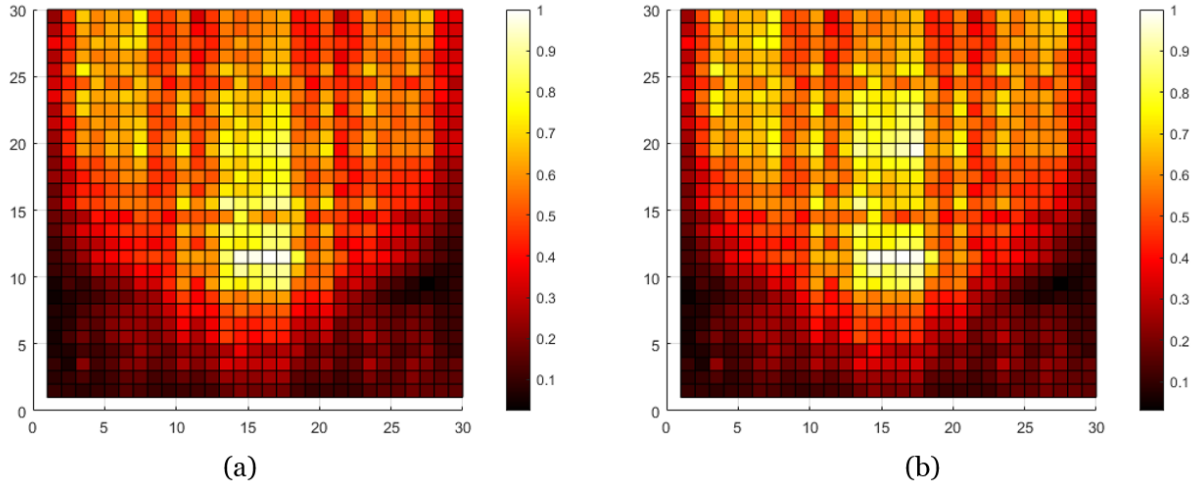


Figure 5.5: Obtained impressions for (a) healthy phantom (b) phantom with 10-mm radius PEC inclusion

To further evaluate the performance of the proposed system setup under more realistic conditions, we conducted a second numerical experiment using a less extreme and more representative anomaly model. In this scenario, instead of embedding a perfect electric conductor (PEC) sphere, we introduced a dielectric inclusion with a relative permittivity of 70, an electrical conductivity of 2 S/m, and a diameter of 5 mm. This inclusion better

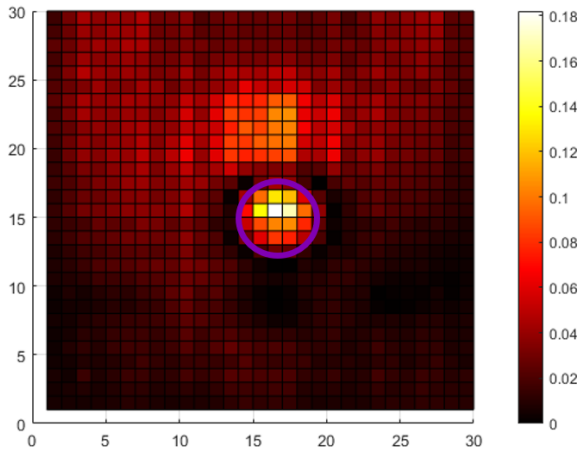


Figure 5.6: Subtracted impression, where the location of the inclusion has been illustrated by the circle.

approximates the electromagnetic properties of biological anomalies, such as malignant tissues. The updated simulation configuration is shown in Fig. 5.7.

As with the previous case, the raw impressions obtained from the simulations—with and without the inclusion—do not exhibit readily discernible differences to the naked eye, owing to the subtlety of the anomaly's impact on the overall field distribution. Therefore, we once again applied the image subtraction technique, performing a pixel-wise difference between the two sets of results. The resulting differential image revealed a distinct localized variation in the electromagnetic response, clearly identifying the region of the embedded inclusion.

For both scenarios—the PEC inclusion and the realistic dielectric inclusion—the resulting contrast in the subtracted images meets the Density Volume (DV) asymmetry criterion described in Chapter 3. This can be seen by comparing the color bar ranges in Fig. 5.6 and Fig. 5.8, which quantify the contrast levels achieved through the subtraction method. These results confirm the system's capability to detect both high-contrast and more subtle, biologically plausible anomalies.

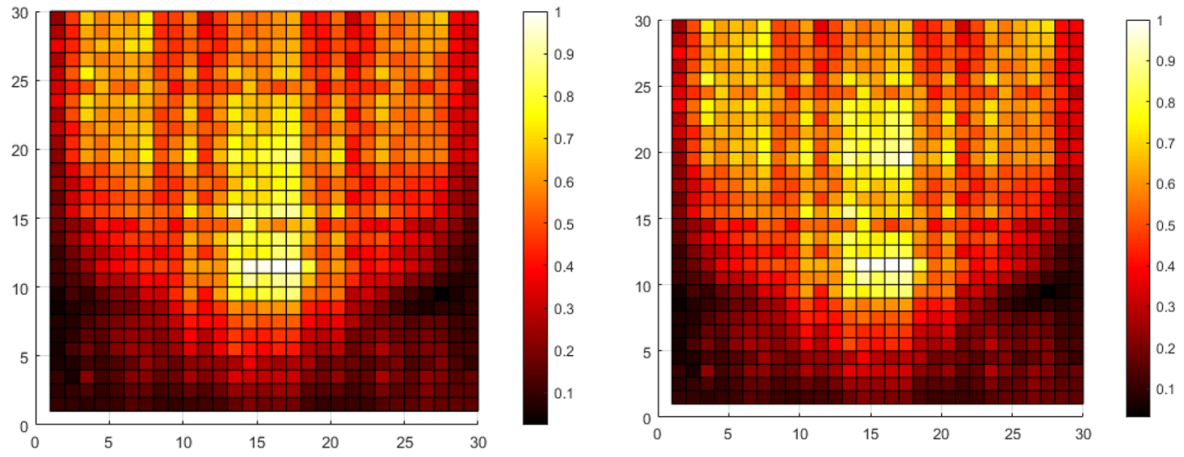


Figure 5.7: Obtained impressions for (a) healthy phantom (b) phantom with 5-mm radius realistic inclusion.

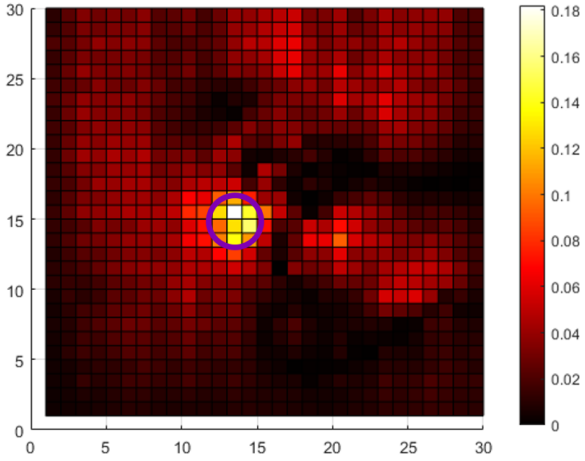


Figure 5.8: Subtracted impression, where the location of the inclusion has been illustrated by the circle

5.4 Experimental System Setup

As previously discussed, one strategy for achieving higher-resolution imaging involves mechanically shifting the metasurface and sequentially scanning different sections of the un-

derside of the breast model. While this method does enable coverage of a larger effective imaging area, it is not without significant drawbacks. First, it introduces additional mechanical complexity into the system, which may increase cost, weight, and susceptibility to mechanical failure. Second, it extends the overall scanning duration, thereby limiting the feasibility of the system for real-time or near-real-time imaging applications.

From a practical perspective, longer scanning times also raise concerns regarding data integrity and reliability. In particular, the extended duration increases the likelihood of acquiring noisy or corrupted measurements due to patient motion, such as breathing or involuntary muscle activity. These motion artifacts can degrade the quality of the reconstructed images and compromise the detection of small anomalies.

To circumvent these limitations, an alternative and more robust approach for improving image resolution is to reduce the size of each unit cell in the metasurface. By decreasing the dimensions of the unit cells while maintaining the overall physical size of the metasurface (e.g., $10\,\text{cm} \times 10\,\text{cm}$), the number of spatial sampling points—equivalently, the number of imaging pixels—increases significantly. This densification of the unit cell array enables finer spatial resolution without requiring mechanical movement.

For instance, a metasurface initially composed of 10×10 unit cells, each measuring $1\,\text{cm} \times 1\,\text{cm}$, yields a total of 100 pixels. By reducing the unit cell size to $3.3\,\text{mm} \times 3.3\,\text{mm}$, the same metasurface can accommodate a 30×30 array, resulting in 900 pixels. This enhancement translates to a theoretical minimum resolvable feature size as small as 3.3 mm, thereby increasing the sensitivity of the system to small anomalies such as early-stage tumors or microcalcifications.

In summary, optimizing the spatial resolution through unit cell miniaturization presents a non-mechanical and scalable pathway to higher-quality imaging. It reduces system complexity, shortens acquisition times, and mitigates the impact of patient motion—all of which are critical factors in clinical and practical deployment scenarios.

In the following experimental setups, which will be elaborated upon in the subsections of this section, we employ two different antenna configurations to evaluate the performance of the imaging system. These antennas were used to illuminate the object under test in two different scenarios.

The data acquisition process was conducted manually. For each unit cell within the metasurface array, we measured the voltage across the capacitor located on the backside of the structure. These measurements were performed using a digital oscilloscope, with probes carefully placed across the capacitor terminals to capture the voltage response.

To assess the system's sensitivity to inclusions, each measurement was repeated twice: first, for the baseline case where the object under test contained no internal inclusions

(serving as the reference), and second, for the scenario in which an inclusion was embedded within the object. This comparative measurement approach allows for direct analysis of the impact of the inclusion on the local electromagnetic response of the metasurface, and forms the basis for reconstructing spatial maps that highlight anomalous features.

While the data acquisition was performed manually in this phase of testing, the experimental results provide valuable insights into the feasibility of the proposed imaging approach and serve as a benchmark for the development of automated, electronically controlled acquisition systems in future iterations of the platform.

5.4.1 Using Dipole Antenna as the Source



Figure 5.9: (a) Transmitter antenna and (b) the stacked-up experimental setup, where the bottom of the layout is exposed

.

In this section, we describe the experiments performed using our custom experimental setup, which consists of three main components. The first component is the transmitter antenna, depicted in Fig. 5.9(a). This antenna is an electrically small dipole, meaning its physical dimensions are significantly smaller than the wavelength of the transmitted signal. It is connected to a signal generator via a coaxial cable.

Electrically small antennas are known to be inherently inefficient radiators, primarily due to challenges in achieving effective impedance matching with the signal source. Even when impedance matching is implemented using a lumped-element matching network, a considerable portion of the input power is still lost. This loss arises from parasitic resistances associated with the lumped elements used in the matching network, which dissipate energy as heat rather than contributing to radiation.

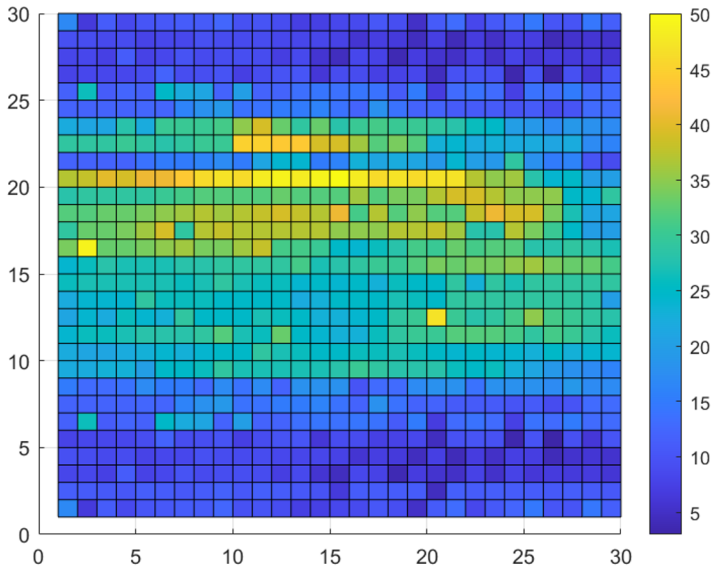


Figure 5.10: The image captured of the object under test

.

To compensate for these losses and improve the amount of power actually radiated by the antenna, we incorporated a radio-frequency power amplifier between the signal generator and the antenna. This amplifier boosts the signal generator's output, increasing the total input power to the antenna to 1 W. In fact, the maximum output power provided by the utilized power amplifier is 1 W.

Despite this high input power of the transmitter antenna, the antenna's low radiation efficiency significantly limits the power that is effectively radiated into space. Based on simulation results and assuming an antenna efficiency of approximately 1%, about 10 mW of the 1 W input is converted into radiated electromagnetic energy. The remaining power is largely dissipated in the matching network or reflected due to residual impedance mismatch. Without the use of the power amplifier, the signal generator alone would not provide sufficient output power, and the radiated power would be significantly lower—well below 1 mW—making it inadequate for our intended measurements.

Next, we mounted the transmitting antenna into its fixture, ensuring stable positioning. A flat plexiglass sheet was then placed over the antenna, serving as a mechanical support platform and reference surface for the placement of the object under test. The test object in this experiment was composed of two distinct layers of biological tissue, specifically slabs of beef. Each slab measured approximately 10 cm $\times$ 5 cm in lateral dimensions and was

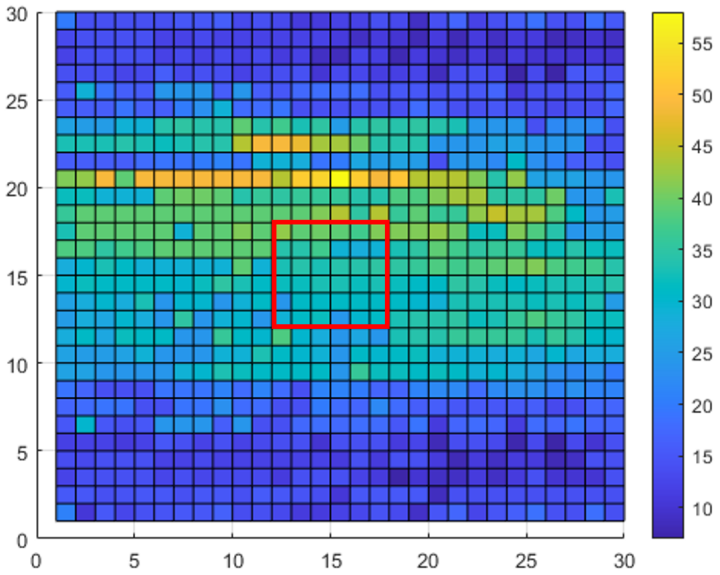


Figure 5.11: The image captured for the case that a metallic inclusion placed in the middle of the object under test

.

3 cm thick. The two slabs were carefully stacked on top of one another to form a multilayer test sample with a total thickness of 6 cm.

To stabilize the structure and maintain consistent contact between the layers, a second plexiglass sheet was placed directly on top of the stacked meat layers. This sheet also served to isolate the biological sample from the experimental components positioned above. Finally, the metasurface was placed on top of this upper plexiglass sheet, such that it was in close proximity to the object under test but mechanically decoupled from it. This layered arrangement not only ensured proper alignment and stability but also allowed unobstructed access to the backside of the metasurface for inspection, adjustment, or measurement purposes, as illustrated in Fig. 5.9(b).

Finally, we measured the voltage across each capacitor located at the backside of the metasurface using an RF power meter. By collecting the voltage data from all the capacitors—effectively sampling the response at each pixel—we constructed a two-dimensional map representing the spatial power distribution. This map serves as an image-like impression of the object under test. The resulting image is shown in Fig. 5.10, where the structure of the biological sample can be visualized.

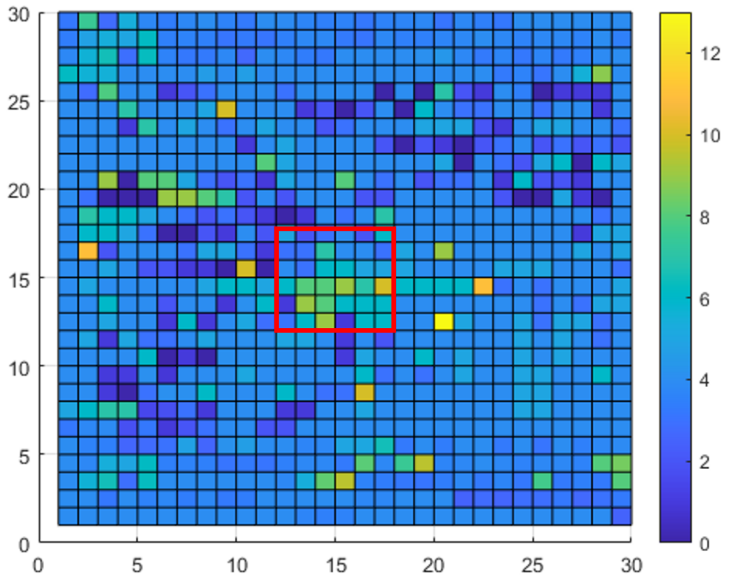


Figure 5.12: The image after subtracting the healthy model and the one with inclusion .

To evaluate the system's ability to detect internal inclusions, we introduced a metallic object into the setup. Specifically, a metallic cube with dimensions of 1.8 cm × 1.8 cm × 1.8 cm was embedded at the center of the biological sample, positioned between the two stacked layers of meat. The measurement process was then repeated in the same manner: voltages across each capacitor were recorded and compiled into an updated two-dimensional image representing the altered configuration of the test object. This second image, which includes the metallic inclusion, is presented in Fig. 5.11.

Subsequently, we performed a pixel-wise subtraction between the two image impressions—one corresponding to the object without the metallic inclusion, and the other with the inclusion present. The resulting differential image is displayed in Fig. 5.12. As expected, the most prominent differences appear in and around the region occupied by the metallic cube, indicating successful localization of the inclusion. However, several other regions also exhibited notable discrepancies. These deviations are likely due to minor inaccuracies in the experimental setup, such as small positional shifts or misalignments of the transmitting and receiving antennas between the two measurement sessions.

For the subtraction technique to be reliable and consistent, it is essential to eliminate such alignment errors prior to computing the differential image. To address this issue,

we are developing proprietary algorithms capable of correcting for source misalignment and system instability. The final stage of the image analysis will incorporate artificial intelligence (AI) methods to enhance robustness and improve detection sensitivity. Based on our prior work, AI-based post-processing has proven to be highly effective in refining image quality and isolating structural anomalies, and we anticipate similar benefits in this context.

5.4.2 Using Loop Array Antenna as the Source

In this section, we employ the magnetically enhanced antenna described in detail in Section 4.3 of this thesis as the excitation source, replacing the electrically small dipole antenna used in the previous section. We anticipate that this new source will yield more promising experimental results for several key reasons:

1. **Uniform Illumination:** The magnetically enhanced antenna is designed as an array, which enables it to provide a more spatially uniform electromagnetic illumination across the object under test. This uniformity improves image consistency and helps reduce artifacts arising from uneven field distributions.

2. **Enhanced Magnetic Field Dominance:** This antenna configuration enhances the magnetic component of the radiated electromagnetic field. As discussed earlier in Chapter 4, this is particularly advantageous for detecting high-conductivity anomalies, such as tumorous tissues. These anomalies tend to absorb water and consequently exhibit high electrical conductivity. Since conductive materials interact more strongly with magnetic fields than with electric fields, enhancing the magnetic field component increases the coupling between the electromagnetic wave and the anomalous regions, thereby improving detectability.

3. **Improved Efficiency:** Unlike the electrically small dipole antenna, which relied on lumped-element impedance matching (often unstable and lossy at high frequencies), the new antenna uses a microstrip impedance matching network. This design offers greater stability and lower insertion losses. As a result, the overall radiation efficiency of the antenna improves, allowing a larger fraction of the input power to be effectively radiated rather than dissipated in the matching components.

Overall, the magnetically enhanced antenna offers multiple advantages over the previously used electrically small dipole. Its array structure, magnetic field emphasis, and

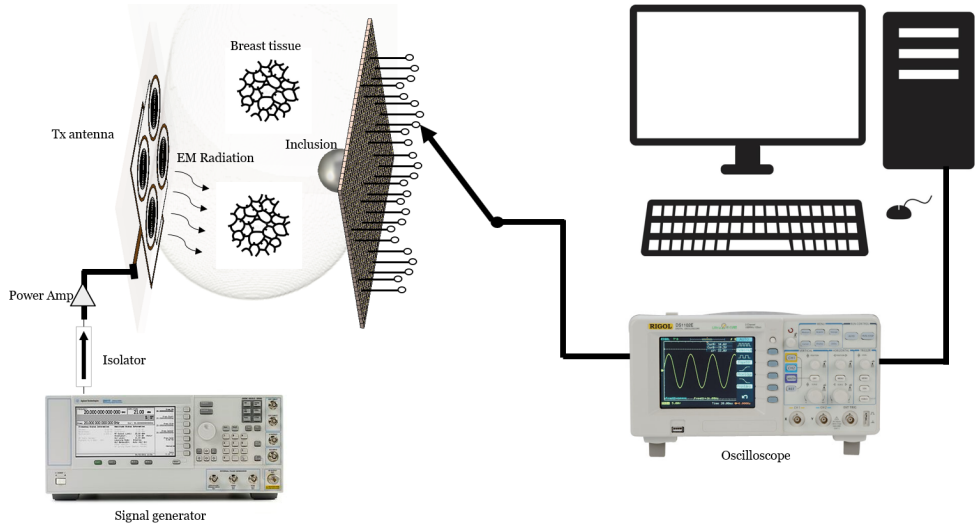


Figure 5.13: Imaging system setup, including the signal generator, power amplifier, isolator, transmitter antenna, metasurface antenna, oscilloscope, and PC.

.

improved matching network collectively contribute to better performance in imaging and anomaly detection tasks.

In this section, we present the results of experiments carried out using our experimental setup, as illustrated in Fig.5.13. In the proposed set-up schematic, instead of a breast, we have used two layers of meat, each measuring 10 cm $\times$ 8 cm area and 2 cm thick, stacked on top of one another. Subsequently, the meat layers were covered with silicon layers to simulate the skin, with a relative permittivity of $\epsilon_r = 11.7$ (see Fig.5.14).

Finally, we measured the voltage across each capacitor using an oscilloscope. By compiling the voltage values from all the cells, we created the final impression. Next, we placed a metallic cube, measuring 1 cm $\times$ 1 cm $\times$ 1 cm between the two layers of meat. We then repeated the measurement process, recording the voltage from each capacitor on the back side of the metasurface, and compiled the values to reconstruct the impression of the object with inclusion. The two captured impressions were then subtracted to give the impression showon in Fig.5.15.

As expected, the greatest differences between the two images after subtraction occurred around and within the metallic cube area. Some minor differences in other parts of the image were also observed, likely due to inaccuracies in the system setup, such as small misalignment and displacements of the transmitter and receiver antennas. For the subtraction

technique to yield accurate results, any source misalignment errors must be filtered out before performing the image subtraction. We are developing proprietary algorithms to address such misalignment errors, and AI will assist in the final stage of image analysis.

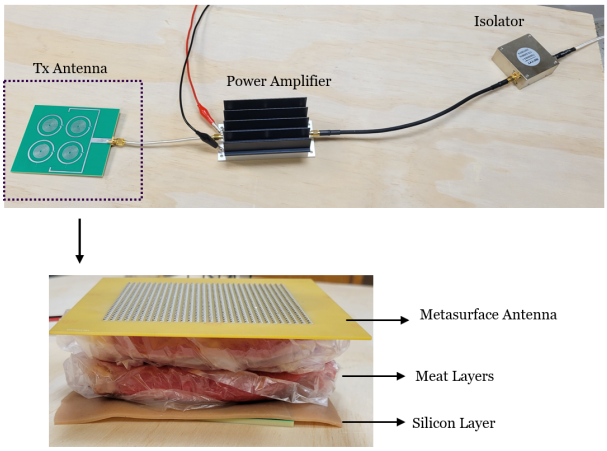


Figure 5.14: The photograph of the experimental system setup highlights the object under test, displaying the stacked-up layers integral to the configuration.

.

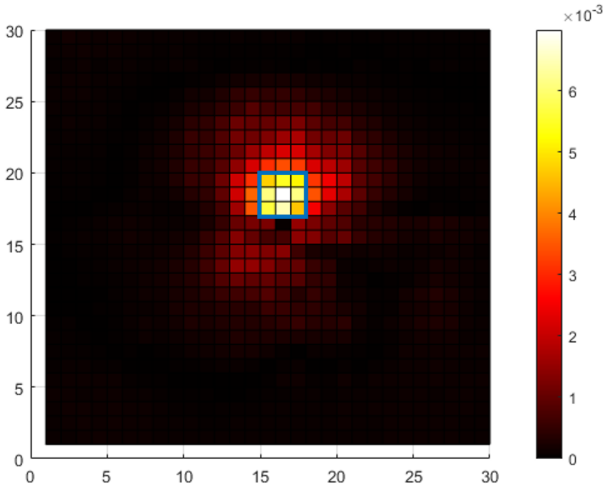


Figure 5.15: The obtained image highlights the anomaly, with its location distinctly marked by the blue box for clear identification.

5.5 Data Acquisition automatization

One of the key design considerations in our system setup was the method of data acquisition. In our initial prototype, we relied on SMA connectors to interface each unit cell with the measurement instruments. The power dissipated in each unit cell was determined by sequentially connecting and disconnecting coaxial cables to a spectrum analyzer—a highly time-consuming and inefficient process, especially when scaling up the number of unit cells.

To address these limitations, we transitioned to a more compact and efficient approach in our miniaturized metasurface design. Instead of measuring power using a spectrum analyzer, we adopted an oscilloscope-based voltage measurement method. This shift offered several advantages. First and foremost, it enabled significant miniaturization of the unit cells. While SMA connectors occupy considerable physical space, the use of SMD (surface-mount device) components with pads as small as 0.6 mm allowed us to reduce the unit cell size substantially, supporting higher spatial resolution and integration density.

Secondly, measuring the voltage directly across the SMD components using oscilloscope probes proved to be a much faster and more convenient method. This eliminated the repetitive task of attaching and detaching coaxial cables, which not only consumed time but also introduced the risk of mechanical disturbances. Such disturbances could potentially alter the measurement conditions or introduce additional noise, compromising the accuracy of the dissipated power readings. By contrast, the oscilloscope probe could be quickly and precisely placed across each component, improving both the speed and reliability of data acquisition.

In this section, our primary objective is to automate the data acquisition process, replacing the current manual approach. Automating this process is expected to significantly improve efficiency by drastically reducing the time required for data collection. Moreover, it minimizes human intervention, thereby lowering the risk of introducing measurement noise caused by physical disturbances or inconsistencies during manual probing. This enhancement not only accelerates the overall workflow but also improves the accuracy and repeatability of the measurements, leading to more reliable and robust experimental results.

To implement the automated data acquisition system, we designed and fabricated a custom multilayer PCB consisting of four layers. The top layer hosts the metasurface sensor array, while the bottom layer is dedicated to the surface-mount (SMD) components. The two internal layers are utilized for routing the switching network, which enables automated signal control and measurement across the array.

For the sake of clarity and visual simplicity, the illustrations provided in this section

depict a reduced 5×5 array. However, the finalized prototype we fabricated comprises a much larger 60×60 array, enabling high-resolution sensing and improved spatial coverage. This multilayer design plays a crucial role in integrating the sensing, switching, and measurement functionalities within a compact footprint, paving the way for scalable and efficient system performance.

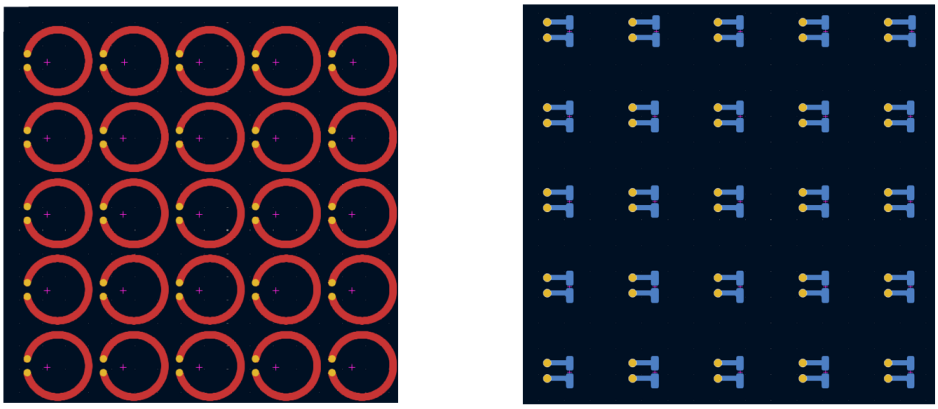


Figure 5.16: Schematic of the 4-layer PCB: (a) top layout (b) bottom layout

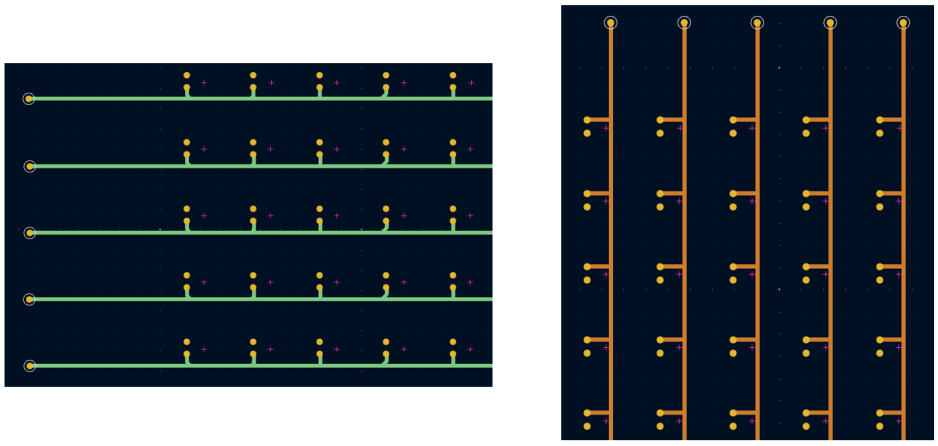


Figure 5.17: Schematic of the 4-layer PCB: (a) mechanical layer 1 (b) mechanical layer 2

Figure 5.16 illustrates the top and bottom layouts of the custom-designed 4-layer PCB, which serves as the core platform for the automated data acquisition system. The top layer contains the metasurface sensor array, while the bottom layer hosts the surface-mount components.

Figure 5.17 presents the internal mechanical layers of the PCB, which implement the switching network. Specifically, Mechanical Layer 1, shown in Fig. 5.17(a), contains the horizontal lines, and Mechanical Layer 2, shown in Fig. 5.17(b), contains the vertical lines. Together, these layers form a matrix-style switching network, enabling precise and programmable access to each unit cell of the array.

Each unit cell in the array is connected to two orthogonal lines—one horizontal and one vertical—forming part of the switching matrix. These lines are individually controlled through a combination of surface-mount components, including diodes, resistors, and capacitors, as well as integrated circuits such as register and MOSFET transistor (MIC 4127). The control circuitry is illustrated in Fig. 5.18, which highlights the configuration used to selectively activate or isolate each unit cell for measurement during automated data acquisition.

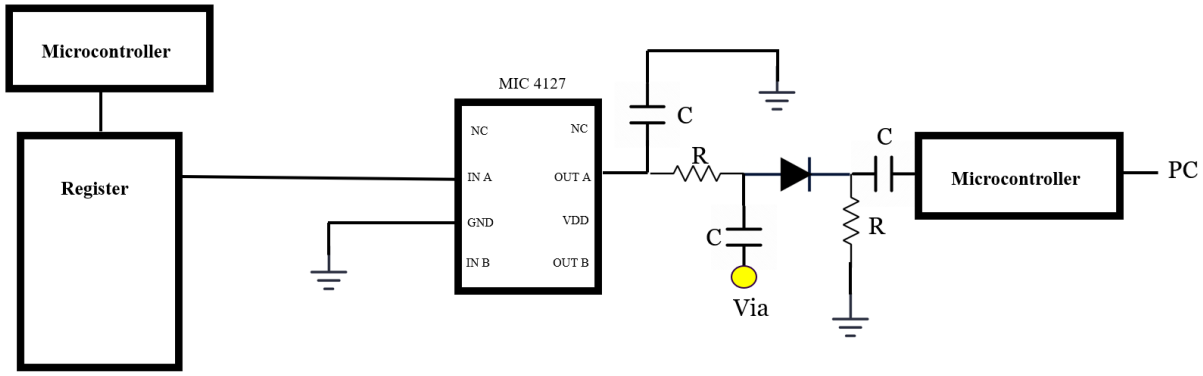


Figure 5.18: Controlling circuit of the switching network

By utilizing a uniform control circuit architecture across all 60×60 lines, we are able to individually address and control each unit cell in the array. To achieve this, we employed 8 horizontal shift registers—each capable of controlling 8 lines—allowing us to manage all 60 horizontal lines efficiently. In parallel, we integrated 60 MOSFET transistors along the horizontal direction to handle signal switching. These transistors are implemented

using MIC4127 dual-channel MOSFET driver ICs, meaning only 30 MIC4127 packages are required for horizontal control.

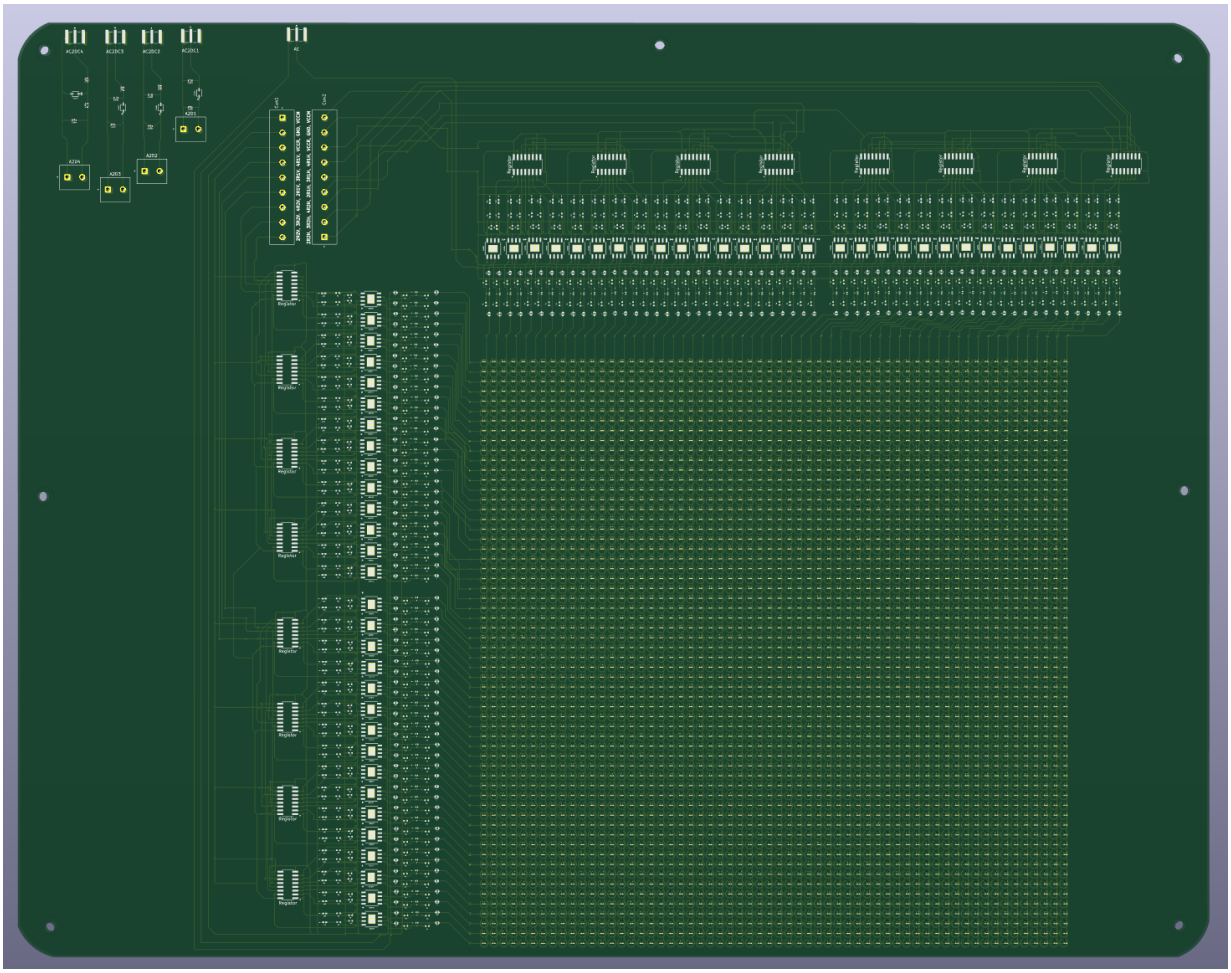


Figure 5.19: PCB design (back layout)

A symmetric configuration is used for the vertical lines: another set of 8 shift registers and 60 MOSFET transistors (30 MIC4127 packages) is employed to control the 60 vertical lines. This scalable and modular design enables precise and independent activation of each unit cell, forming the foundation of our fully automated data acquisition system.

The complete layout of the designed board is shown in Fig.5.19. At the center of the board, the SMD pads—corresponding to each unit cell—are clearly visible. The horizontal and vertical control circuits are positioned along the top and left edges of the array,

respectively, enabling systematic addressing of the entire 60×60 grid.

The board also includes two 10-pin connector packages, which serve multiple purposes: some pins provide power and ground connections, a few of them are used for data acquisition from the SMD pads, and some of them interface with the microcontroller for programming and control. These pin connectors are strategically placed to ensure organized routing and ease of integration with external systems.

Additionally, located in the upper-left corner of the board are four analog-to-digital converters (ADCs). These ADCs are responsible for digitizing the analog signals acquired from the sensor pads before transmitting the data to the microcontroller. This conversion step ensures reliable digital data representation, which is essential for accurate signal processing and automated data acquisition.

Chapter 6

Quasi-Electrostatic Computerized Tomography

6.1 Introduction

Microwave imaging (MWI) has emerged as a promising non-invasive diagnostic technique across various fields, including medical imaging, security screening, and subsurface sensing. However, a fundamental challenge in MWI lies in the reconstruction of accurate and meaningful images from the measured electromagnetic data. Unlike conventional imaging modalities, MWI does not benefit from a straightforward image processing framework, largely due to the complex, nonlinear, and ill-posed nature of the underlying inverse scattering problem [111, 112].

Image reconstruction methods in MWI are broadly classified into qualitative and quantitative approaches. Qualitative methods, often inspired by radar imaging techniques, aim to produce images that reveal the approximate shape, location, and contrast of the object under test (OUT) [38]. These methods typically rely on approximations such as the Born or Rytov models and are computationally efficient, making them suitable for real-time or large-scale imaging scenarios. However, they generally offer limited spatial resolution and do not provide explicit information about the electromagnetic properties of the OUT.

In contrast, quantitative methods strive to reconstruct detailed images that directly map the dielectric properties—specifically the permittivity and conductivity distributions—of the investigated object [113]. These methods involve solving nonlinear inverse problems, often requiring iterative algorithms and substantial computational resources. While they

offer higher fidelity and are capable of revealing the internal structure and material composition of the OUT, their complexity and sensitivity to noise present significant challenges.

Another intrinsic limitation of microwave imaging stems from the diffraction limit, a fundamental constraint dictated by wave physics. In the far-field, also known as the Fraunhofer region, the achievable spatial resolution is fundamentally limited to approximately half the operating wavelength. This constraint leads to inherently low-resolution images, which hampers the ability to resolve fine details within the object. Overcoming the diffraction limit has therefore been a central focus in MWI research. Numerous techniques have been proposed in the literature to enhance resolution beyond this limit, ranging from near-field imaging and synthetic aperture methods to advanced signal processing and machine learning-based approaches [114–118].

Recent advancements in our research have aimed to overcome the resolution limitations inherent in traditional microwave imaging by exploring novel system configurations and physical principles [55, 98, 99]. In particular, we have demonstrated the potential to generate high-resolution images of objects under test (OUT) by leveraging electrically small sources and detectors, effectively challenging the classical diffraction limit that constrains far-field imaging performance.

The core of our approach is an innovative imaging technique that utilizes highly localized radiators—or electrically small antennas—to operate at relatively low microwave frequencies while achieving enhanced spatial resolution. The central idea is based on the observation that when the OUT is electrically small—i.e., its dimensions are much smaller than the operating wavelength—the interaction between the radiated field and the object becomes highly localized. In this regime, the field behavior can be approximated as ray-like, despite the wave nature of microwaves, due to the limited scattering volume and reduced diffraction effects.

This quasi-ray behavior results in a localized interaction where the receiver closest to the source experiences the greatest influence from the object's internal structure along the direct path between transmitter and receiver. This interaction is conceptually analogous to X-ray imaging, where the recorded image is shaped by the cumulative attenuation of rays as they pass through various tissues. Similarly, in our system, the localized microwave signal is modulated primarily by the material properties encountered along its direct trajectory through the OUT.

This physical insight forms the basis of our tomographic reconstruction technique, which draws inspiration from X-ray computed tomography (CT). By collecting transmission measurements across multiple angles and applying the Radon transform, we can reconstruct two-dimensional projections that reveal the internal contrast and shape of the OUT. Impor-

tantly, our method requires only the magnitude of the transmission coefficients (—S21—), thereby simplifying the system and reducing sensitivity to phase noise and calibration errors.

Given its goal of mapping the geometric and dielectric contrast within the object—rather than its exact electromagnetic properties—our technique is categorized as a qualitative imaging method. Nevertheless, both simulation results confirm its ability to resolve fine structural details that would typically be obscured in conventional microwave imaging setups.

Building upon the ray-like behavior observed in low-frequency microwave imaging, we propose an extension of Microwave Computed Tomography (MCT) into the electrostatic regime, introducing a novel imaging paradigm termed Electrostatic Computed Tomography (ECT). This concept is grounded in the theoretical analogy between low-frequency electromagnetic wave propagation and electrostatic field behavior.

In MCT, the emergence of ray-like interactions between the object under test (OUT) and the measurement system is contingent upon two critical conditions: (1) the use of electrically and physically small sources and detectors (i.e., localized elements), and (2) the requirement that the OUT be electrically small relative to the operating wavelength. Under these constraints, the interaction between the transmitted wave and the object becomes spatially localized, enabling tomographic reconstruction techniques such as the Radon transform to be effectively applied.

As the operating frequency tends toward zero, the electromagnetic wavelength becomes infinitely large, thereby transitioning the system into the electrostatic regime. In this regime, the aforementioned conditions are inherently satisfied: the OUT is effectively vanishing in size compared to the wavelength, and all sources and detectors, regardless of their physical dimensions, are electrically small. Therefore, to preserve the ray-like behavior necessary for tomographic reconstruction, the only remaining condition is the physical miniaturization of the sources and detectors—ideally approximated as point elements.

Based on this premise, we propose that Electrostatic Computed Tomography is theoretically valid as long as the system employs physically small point sources and detectors and operates under quasi-static conditions. To experimentally validate this concept, we employed a measurement setup that closely mirrors the configuration used in our previous MCT work, with a key modification: the excitation source. Instead of a time-varying microwave excitation, we introduced a static electric dipole moment—implemented as a pair of opposite charges separated by a small distance—to serve as the electrostatic source.

For image reconstruction, we adopted a back-projection algorithm similar to that used in MCT, capitalizing on the directional characteristics of electrostatic fields. Despite the

static nature of the field, the lines of influence from source to detector retain a directional, ray-like quality that aligns well with Radon transform-based reconstruction methods. Through this approach, we were able to successfully recover the internal contrast of the OUT in simulated environments.

We further investigated two scanning geometries to facilitate comprehensive coverage: the pencil beam and fan beam configurations. While both are capable of generating accurate reconstructions, the fan beam geometry offers significant advantages in terms of computational efficiency, particularly in large-scale simulations, by reducing the number of required source positions.

Additionally, our study explores how the polarization of the electrostatic point source—i.e., the orientation of the dipole moment—affects image quality and spatial resolution. By analyzing the resulting field distributions and reconstructed images, we provide insights into the optimal design of ECT systems for various application domains.

This section presents the theoretical foundation, simulation results, and performance analysis of Electrostatic Computed Tomography, demonstrating its feasibility as a high-resolution, low-complexity imaging technique.

6.2 Theory of Quasi-Electrostatic Computerized Tomography

In our previous work[55], it was shown that if the wavelength is much larger than the size of the OUT, we could apply microwave tomography, using back-projected graphs and Radon Transform. Radon transform is applicable when the governing physics of the problem shows ray-like behavior. Two important considerations for the ray-like behavior of the microwave sources are as follows: placing OUT in close proximity to the microwave source and using low enough frequency transceivers to ensure sufficient penetration into the OUT. Notably, there is an analogy between this observation and the theory of quasistatics. Quasistatics is a simplified method used to examine electrodynamic systems, focusing on scenarios where electromagnetic propagation is not a major factor. This approach assumes that changes in the fields occur at a much slower rate compared to the spread of energy. In other words, electrostatic approximation is valid if wavelength approaches infinity. In this condition, the time-derivatives of the fields can be ignored., i.e.,

$$\frac{\partial \vec{\mathbf{B}}}{\partial t} \approx \frac{\partial \vec{\mathbf{E}}}{\partial t} \approx 0 \tag{6.1}$$

As a result, Maxwell equations reduce to

$$\begin{cases} \nabla \times \vec{\mathbf{E}} = 0 \\ \nabla \cdot \vec{\mathbf{E}} = \frac{\rho}{\varepsilon_0} \\ \nabla \times \vec{\mathbf{B}} = \mu_0 \vec{\mathbf{J}} \\ \nabla \cdot \vec{\mathbf{B}} = 0 \end{cases} \tag{6.2}$$

The first two equations of (6.2) represent electrostatics, while the last two equations represent magnetostatics. It is important to note that, under the assumption of the quasistatic approximation, the electric and magnetic fields are decoupled. As a result, electromagnetic radiation is assumed negligible.

In the proposed electrostatic tomography, similar to microwave tomography, we use sources with ray-like characteristics to obtain images of the OUT. A common attribute among all these methods is that the rays travel in a straight line, providing information about the path between the source (transmitter) and the corresponding detector (receiver). In our proposed tomography method based on electrostatics, it is crucial to position the source in close proximity to the OUT. This placement ensures the enclosure of a large number of electrostatic field contours and their interaction with all constituents of the OUT. As a result, the electric intensity detected by the detector on the opposite side of the OUT becomes directly correlated with the electrical properties of the constituents along the interrogated cutline. The aforementioned characteristics of the source contribute to its ray-like behavior, enabling the application of the Radon transform for image reconstruction in the electrostatics regime.

To test the the concept, we conducted a numerical experiment in which we arranged six blocks of dielectric material with distinct permittivities in a cascaded formation, as shown in Fig. 6.1. We used a dipole moment as the electrostatic source and systematically shifted it one by one to scan through the structure. We measured the electric intensity when the source was positioned precisely at the midpoint of each block.

As shown in Fig. 6.1, the anomaly identified in the 1-D structure corresponds to the spike seen in the graph at the position of the second block. However, in many real-world scenarios, objects of interest are often two-dimensional (2-D) or three-dimensional (3-D). In these cases, an image reconstruction algorithm becomes essential to retrieve the object's image, as we need to capture electric field from different angles and combine the resulting dataset to reconstruct the image. As previously discussed, physically localized electrostatic sources exhibit ray-like behavior, making the adaptation of Radon transform algorithms applicable in the electrostatic regime for image reconstruction. In this study, our focus is solely on image reconstruction of 2-D structures. This is primarily due to the large

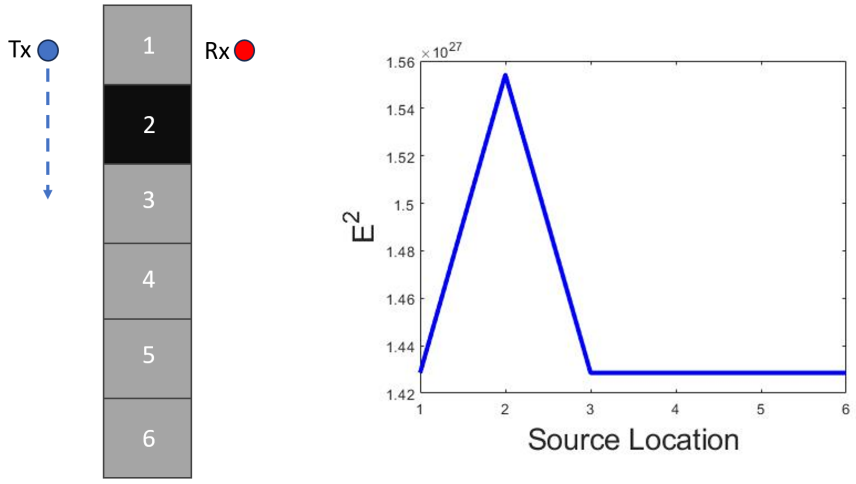


Figure 6.1: The electric intensity observed when stimulating the structure with a localized electrostatic source positioned in the near-field region, with media 1 to 6 having the subsequent permittivities:$\epsilon_1 = 2\epsilon_0$, $\epsilon_2 = 6\epsilon_0$, $\epsilon_3 = 2\epsilon_0$, $\epsilon_4 = 2\epsilon_0$, $\epsilon_5 = 2\epsilon_0$, and $\epsilon_6 = 2\epsilon_0$.

.

number of simulations involved, making numerical simulations of 3-D structures highly time-consuming and exceeding the capabilities of standard personal computers.

In a 2-D Radon transform, the 2-D function $f(x, y)$ that is a 2-D cut of the 3-D OUT along x-y plane, will be projected to a 1-D profile $g(\rho, \theta)$ (see Fig. 6.2). Using Radon transform, the $f(x, y)$ graph is projected to the $g(\rho, \theta)$ profile along the line $x \cos\theta + y \sin\theta = \rho$. The relationship between $f(x, y)$ and $g(\rho, \theta)$ relies on a line integral as follows:

$$g(\rho, \theta) = \int_{-\infty}^{\infty} \int_{-\infty}^{\infty} f(x, y)\delta(xcos\theta + ysin\theta - \rho)\, dx\, dy \tag{6.3}$$

where δ is the Dirac delta function. $g(\rho, \theta)$ is the projection profile of the OUT in different angles. Each point on the $g(\rho, \theta)$ graph is associated with a specific line integral. For instance, the point $g(\rho_k, \theta_l)$ is corresponding to the line integral of $f(x, y)$ on the line $\rho = \rho_k$ with the angle of $\theta = \theta_l$.

Fig. 6.2 shows the system setup for Radon transform projection. In the illustrated system setup, we excite the OUT with an electrostatic dipole moment polarized in the X-direction or Y-direction, depending on the utilized Radon transform algorithm, which will be elaborated upon in the continuation. As shown in Fig. 6.2, at each specific angle, the projected graph will be recorded on the detector side. This graph can be recorded by

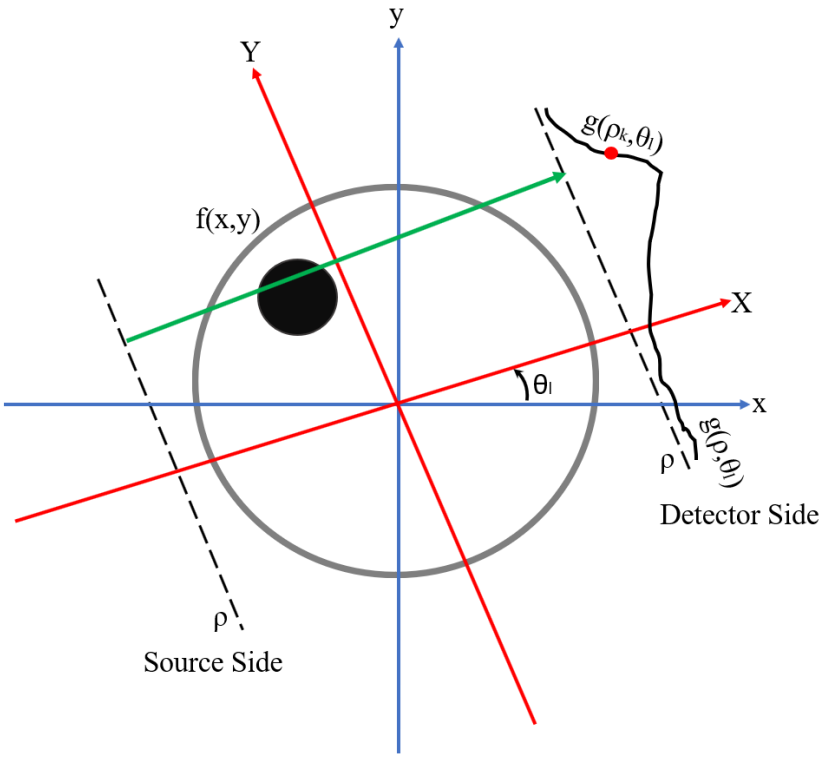


Figure 6.2: electrostatic computed tomography system setup.

moving a probe on the ρ line. However, in practice, recording a continuous $g(\rho, \theta)$ graph and taking the integral continuously (as shown in Eq. (6.3)) is not possible, so we need to approximate the continuous integration with a desecrate summation as follows:

$$g(\rho, \theta) = \sum_{x=0}^{M-1} \sum_{y=0}^{N-1} f(x, y)\delta(x \cos\theta + y \sin\theta - \rho), \tag{6.4}$$

where x, y, ρ, and θ are discrete parameters and $N \times M$ represents the total number of points inside the OUT, which have been projected on the $g(\rho, \theta)$ graph. Clearly, we will end up with a more accurate line integral if we increase N and M values in the summation. By decreasing the rotational angle and sampling increments, we can increase N and M. The projection profile $g(\rho, \theta)$ is the Radon transform for each discrete value of θ, when the OUT is scanned by the source along the ρ line.

Using the profiles of the Radon transforms $g(\rho, \theta_l)$, where different angles are associated with different values of θ_l, we can reconstruct the image of the OUT by applying back-

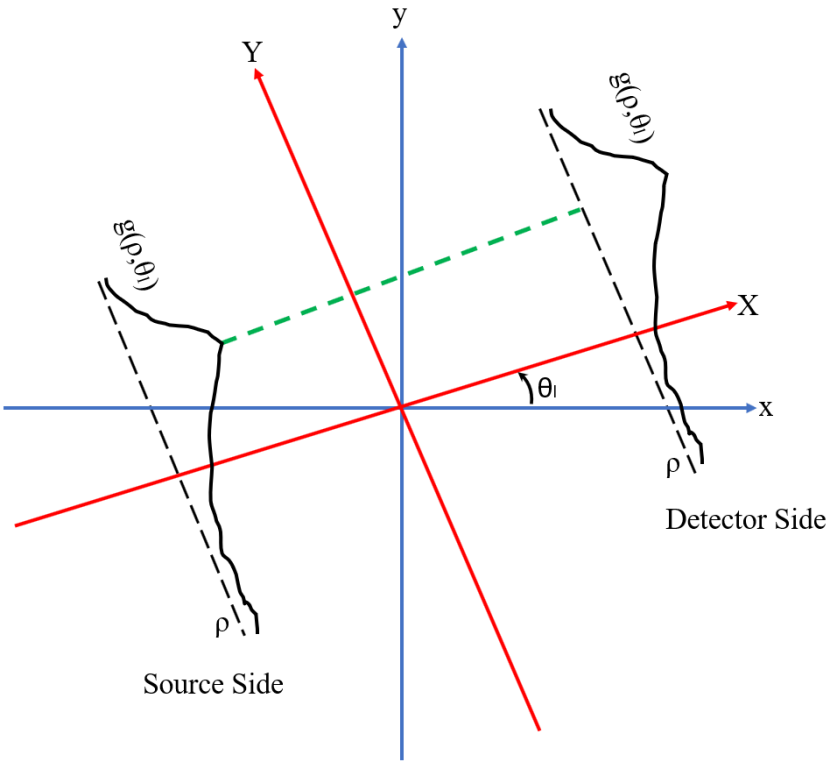


Figure 6.3: Back-projected graph from the source side to the detector side.

projection, which copies the $g(\rho, \theta_l)$ profiles from the detector side to the source side (see Fig. 6.3). Each $g(\rho, \theta_l)$ profile can provide us with an image at θ_l, which is called sinogram. Fig. 6.5 shows the Radon transforms and sinograms of the OUT in the electrostatic CT setup, where the rotational angle increment is assumed to be 45°.

By repeating the same process with all the angles, a blurry and raw image of the OUT will be obtained, which is called a laminogram. To remove the blurriness of the obtained image, we will apply the Fourier-slice theorem, which states that the Fourier transform of each back-projected profile would be one slice of the Fourier transform of $f(x, y)$. For instance, consider the back-projected graph $g(\rho, \theta_l)$ on the ρ line at the detector side of the tomography setup. By applying a 1-D Fourier transform on the $g(\rho, \theta)$ graph at each angle, $G(f, \theta)$ at that specific angle, which is one slice of a 2-D spatial Fourier transform of the OUT $f(x, y)$, will be obtained as (see Fig. 6.4)

$$G(f, \theta) = \int_{-\infty}^{\infty} g(\rho, \theta) \mathrm{e}^{-\mathrm{j}2\pi f \rho} \, d\rho. \tag{6.5}$$

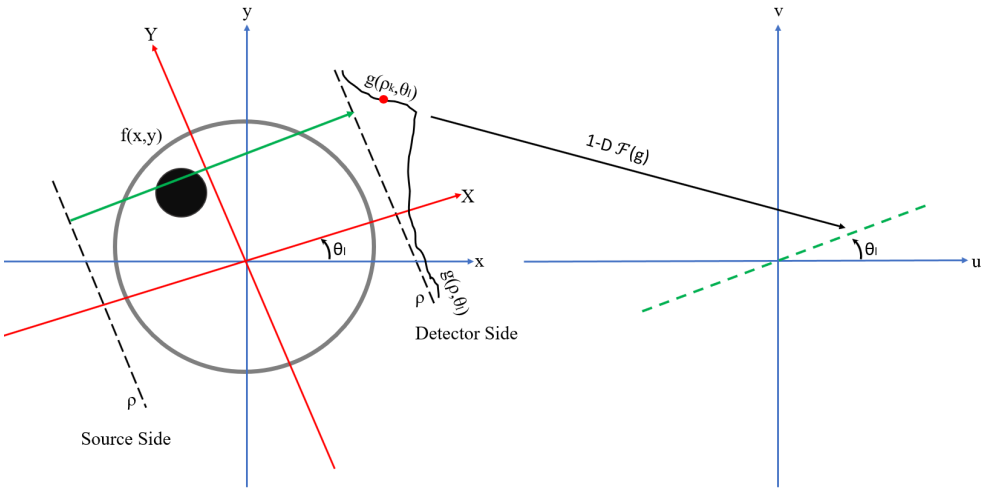


Figure 6.4: Fourier transform of g(ρ_k,θ_l) from the x-y plane to u-v plane.

Therefore, by applying a 1-D inverse Fourier transfer, $f(x, y)$ can be written as

$$f(x,y) = \int_0^{\pi} \Big[\int_{-\infty}^{\infty} |f| G(f,\theta) \mathrm{e}^{\mathrm{j}2\pi f\rho} \Big]_{\rho = x\cos\theta + y\sin\theta} df\, d\theta, \tag{6.6}$$

where $|f|$ is a ramp filter intended to dampen the low-frequencies in the back-projected graphs and magnify the high-frequency information. However, by doing so, when the bounds approach infinity, the integrand value becomes undefined. To solve this issue, we need to multiply the integrand by a low-pass filter (Hamming window) to reduce the high values. Thus, the post-processing part for removing the blurriness contains multiplying the $G(f, \theta)$ graph by a ramp filter and a Hamming window. Finally, by taking the inverse Fourier transform from the post-processed $G(f, \theta)$, we will obtain the final image of the OUT.

Simulation Results

The simulations were performed in COMSOL multiphysics 6.0 AC/DC module [119]. The physics of this module is based on the first two electrostatic equations: $\nabla \times \vec{\mathbf{E}} = 0$ and $\nabla \cdot \vec{\mathbf{E}} = \frac{\rho}{\varepsilon_0}$. The other two equations, namely magnetostatic equations ($\nabla \times \vec{\mathbf{B}} = \mu_0 \vec{\mathbf{J}}$ and $\nabla \cdot \vec{\mathbf{B}} = 0$), do not play any role in our calculations, since we are exciting the OUT with electric dipole moment and there is no coupling between the electric and magnetic fields.

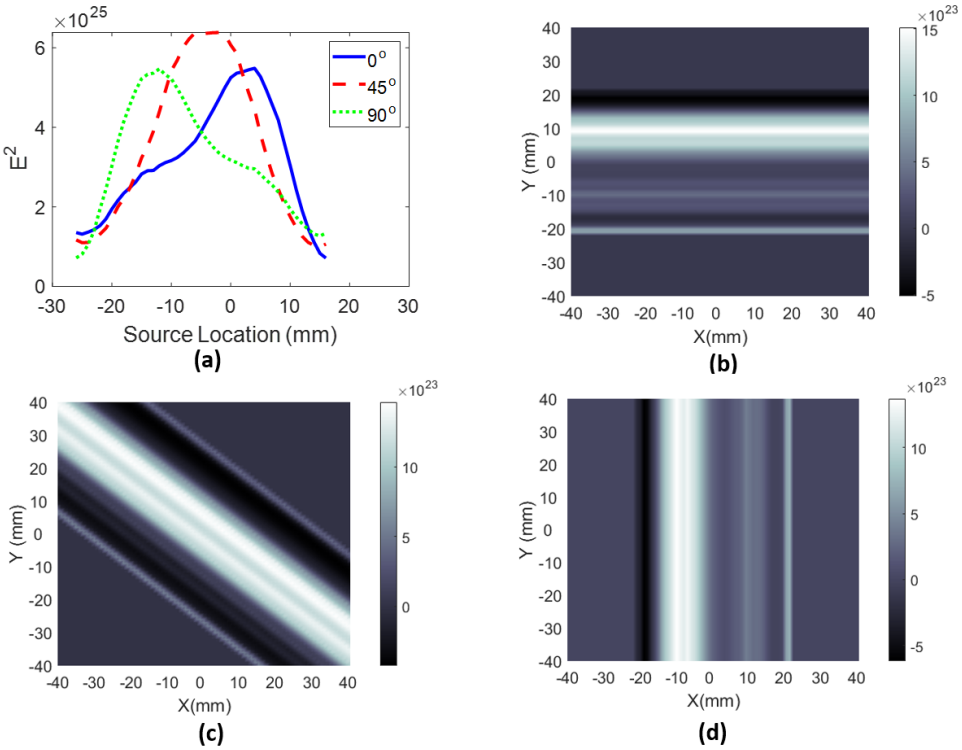


Figure 6.5: (a) Back-projected profiles g(ρ,θ_l) with different angles of θ_l (b) the corresponding sinogram of $\theta = \theta_1 = 0°$ (c) $\theta = \theta_2 = 45°$, and (d) $\theta = \theta_3 = 90°$.

Thus, the conservation of electric fields ($\nabla \times \vec{\mathbf{E}} = 0$) and the Gauss's law for electric fields ($\nabla \cdot \vec{\mathbf{E}} = \frac{\rho}{\varepsilon_0}$) will be the backbone physics of our simulations.

Using two different algorithms, namely the fan beam and pencil beam, which will be elaborated upon later, we will apply the proposed electrostatic tomography method to retrieve images of different objects. Fig. 6.6 (a) shows OUT-1, which contains an inclusion with a relative permittivity of $\epsilon_r = 20$ and with a diameter of 12 mm, inserted in a bigger cylindrical medium with a relative permittivity of $\epsilon_r = 2$ and a diameter of 40 mm. Figure. 6.6 (b) and (c) show the equipotential contours when an X-polarized or Y-polarized point source is utilized. Also, Fig. 6.6 (b) and (c) show how the equipotential contours interact with the OUT-1, as well as how they have been enclosed. It will be shown later that using the X-polarized dipole moment for the fan beam method will lead to undesired results (blurry images). But, in the pencil beam method, both X-polarized and Y-polarized excitation will lead to images with distinguishable inclusions.

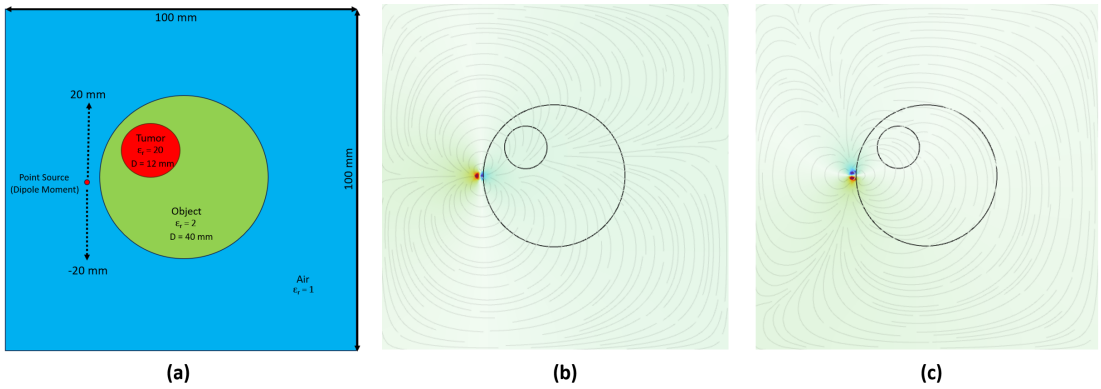


Figure 6.6: (a) OUT-1 model for one tumor (b) X-polarized excitation (c) Y-polarized excitation at $\theta_l = 0°$.

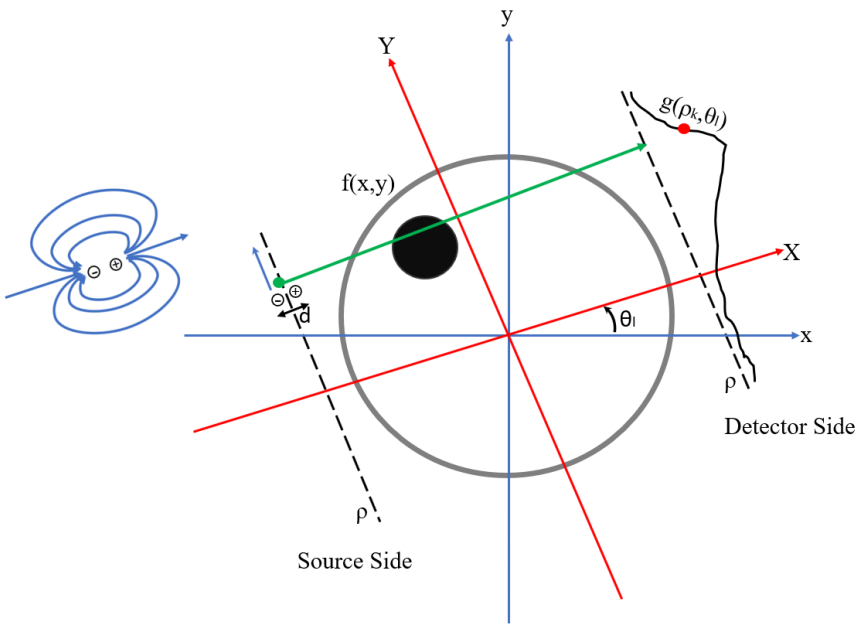


Figure 6.7: Pencil beam setup.

Depending on the algorithm used (fan beam or pencil beam), we need to use different system setups. The first method that we investigate here is the pencil beam algorithm, where we shift the point source on the ρ line in the source side with the increment of 1 mm (from -21 mm to 21 mm). Then, we rotate the OUT with $\theta_l = 5°$ angle increment (from 0° to 359°). Here, we chose $\theta_l = 5°$ to ensure a sufficiently fine rotational increment,

facilitating a clear representation of the OUT. In this approach, we ran $M \times N = 3096$ number of simulations, where $M = 43$ is the total number of points to fully scan the object on the ρ line, and $N = 72$ is the total number of rotations to fully scan the object under different angles (see Fig. 6.7). In Fig. 6.7, the pencil beam system setup is shown with an X-polarized point source excitation. However, this approach is applicable for both X- and Y-polarized dipole moments. Both polarizations are applicable, as it is sufficient in the pencil beam algorithm to examine the horizontal cutline (indicated by the green solid line in Fig. 6.7 along the X-axis) for retrieving the image. In either polarization, due to the presence of the localized point source, there exists a ray-like behavior in the excitation. Subsequently, we can record the corresponding cutline information by placing a detector probe in front of the excitation source, but on the opposing side of the object being examined. In summary, as long as the excitation source is local and exhibits ray-like behavior, regardless of its polarization, the pencil beam algorithm can be utilized.

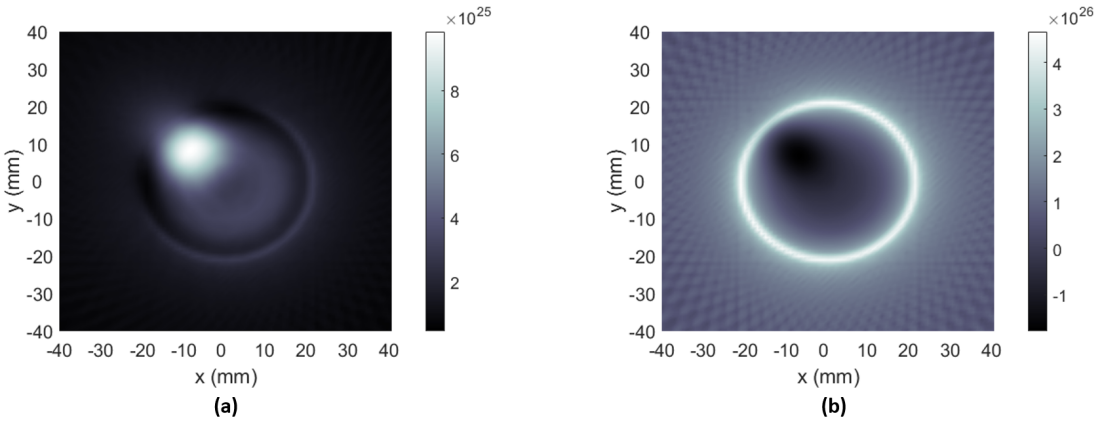


Figure 6.8: (a) The obtained image using the pencil beam method for OUT-1 for the X-polarized source (b) for the Y-polarized source.

The obtained images of the OUT-1 are shown in Fig. 6.8. Differences in permittivities between the larger and smaller cylinders result in discernible contrasts in the obtained images. The center of the smaller cylinder is placed at c_t = (-8 mm, 8 mm) with respect to the Cartesian coordinate system, which was accurately captured in the images. Another interesting observation in Fig. 6.8 (a) and (b) is that the brightness and darkness in the images are interchanged based on the polarization. This occurs because the electric fields generated by X- and Y-polarized point sources exhibit opposite fluctuations. Specifically, an increase in the electric field from the X-polarized source corresponds to a decrease in the electric field from the Y-polarized source, and vice versa.

The second method that we investigate here is the fan beam algorithm, where we fix the source at the center of the ρ line in one side, and then, rotate the OUT with θ_l angle increment. This approach is much faster than the pencil beam algorithm in terms of the simulation time since the probe and source are not shifted simultaneously in order to capture the corresponding information. In this approach, the total number of simulations is equal to the total number of rotations to fully scan the object. Here, we rotate the OUT with $\theta_l = 5°$ angle increment (from 0° to 359°). Thus, the total number of simulations would be $N = 72$ (see Fig. 6.9), which is much less than the total number of simulations in the pencil beam setup, which was $M \times N = 3096$.

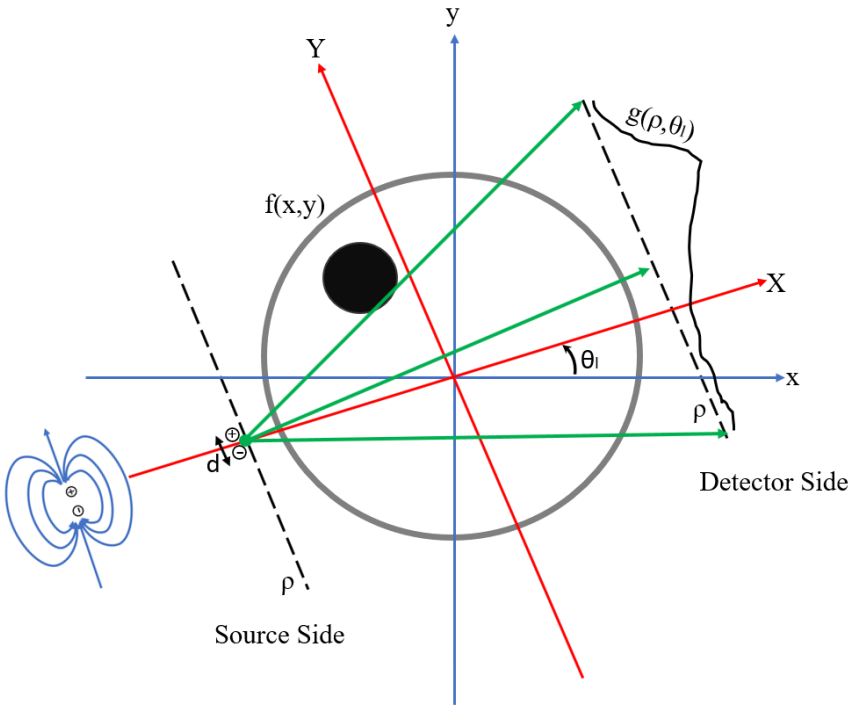


Figure 6.9: Fan beam setup.

Only a Y-polarized dipole moment is applicable in fan beam setup since we need to interrogate the vertical cutline and record a continuous back-projected graph $g(\rho, \theta)$ on the ρ line of the detector side for each angle. The obtained image shown in Fig. 6.10 consists of a bigger cylinder (representing the normal medium) and a smaller cylinder (representing the inclusion). Here, again, the inclusion is placed at c_t = (-8 mm, 8 mm) with respect to the Cartesian coordinate system. As is obvious, the image which is captured by the X-polarized source is blurry and the inclusion is not captured clearly (see Fig. 6.10 (a)),

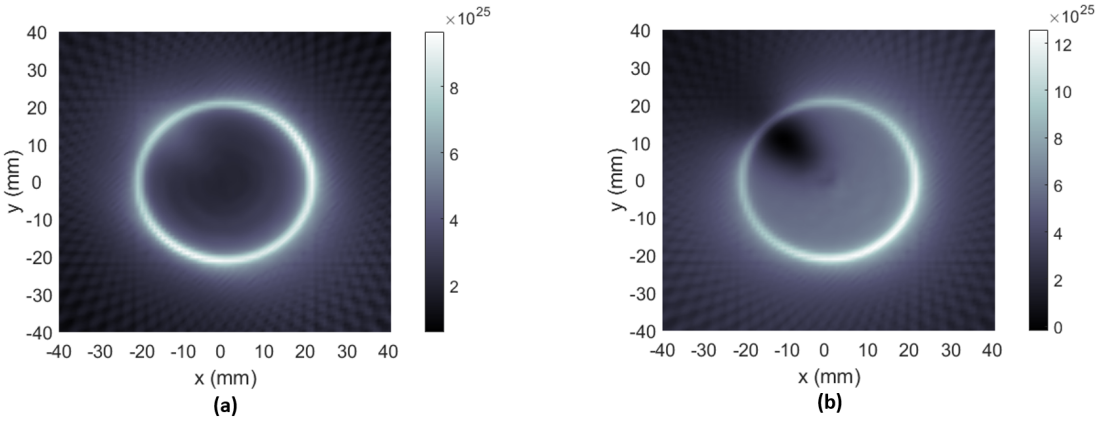


Figure 6.10: Images obtained using the fanbeam method for OUT-1 for the X-polarized source (b) for the Y-polarized source.

although there is an ambiguous brightness around the location of the inclusion. However, the image captured by the Y-polarized source clearly shows the inclusion with a dark circle at c_t (see Fig. 6.10 (b)). Similar to the pencil beam method, the images exhibit a reversal of brightness and darkness depending on the source polarization.

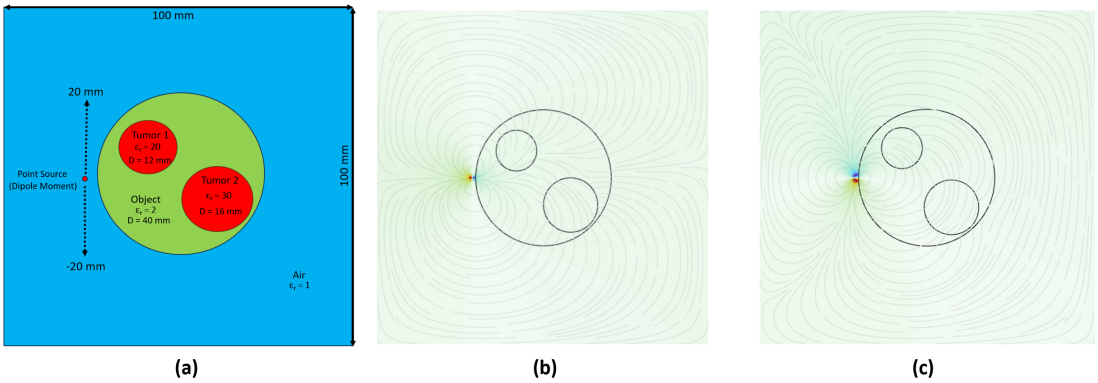


Figure 6.11: (a) OUT-2 model for two cylindrical inclusions. (b) X-polarized excitation (c) Y-polarized excitation at $\theta_l = 0°$.

Next, we test a different OUT by adding another inclusion with different properties and sizes inside the bigger cylinder. Fig. 6.11 (a) shows the OUT-2, where there exists an inclusion with $\epsilon_r = 20$ and a diameter of 12 mm and another inclusion with $\epsilon_r = 30$ and a diameter of 16 mm, both inserted in a bigger cylinder with $\epsilon_r = 2$ and a diameter of 40

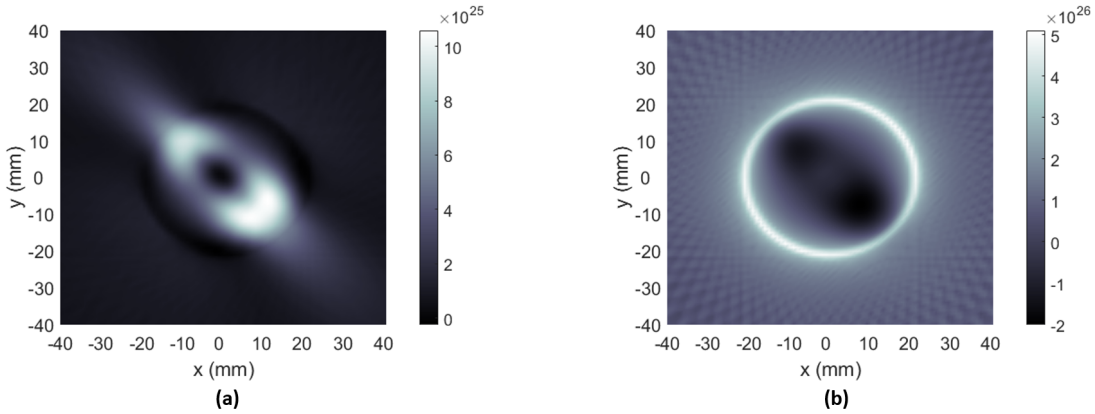


Figure 6.12: Images obtained using the pencilbeam method for OUT-2 for the X-polarized source (b) for the Y-polarized source.

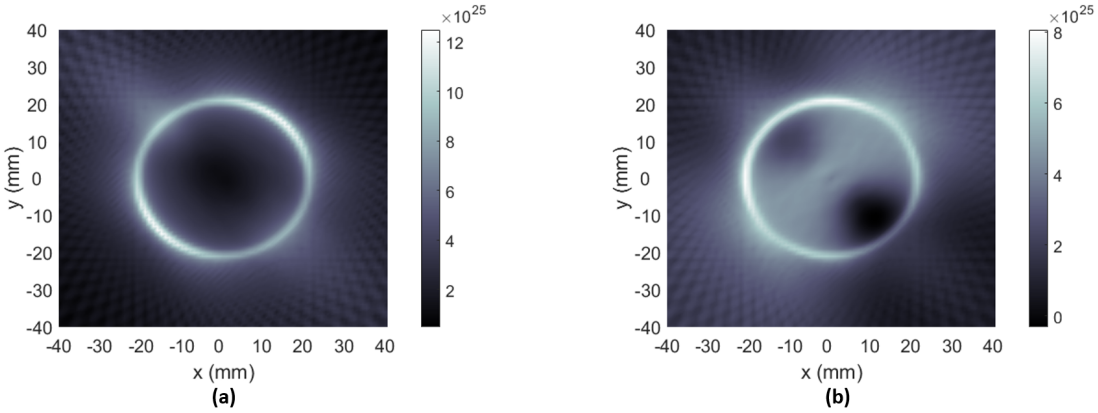


Figure 6.13: Images obtained using the fanbeam method for OUT-2 for the X-polarized source (b) for the Y-polarized source.

mm. Figures 6.11 (b) and (c) show the equipotential contours and how they interact with the OUT-2 when an X- and Y- polarized point source has been utilized, respectively.

The resultant image of the pencil beam method is shown in Fig. 6.12. We observe two bright or dark inclusions inside the bigger cylinder, depending on the X-polarized or Y-polarized excitation, which represents the denser regions in OUT-2 model. The images of the inclusions are elongated and deformed circles, rather than perfect circles. As the structure becomes more complicated, the internal reflections of the electrostatic fields, between the denser inclusions, will cause some spatial shift and distortion in the back-

projected graphs. Consequently, the captured image will be deformed. However, the obtained image still presents a good depiction of the inclusions inside the larger cylinder. We observe that the bottom-right inclusion is both brighter (or darker for Y-polarized) and bigger than the upper-left inclusion. In the captured image, using the pencil beam algorithm, the brightness (or darkness for Y-polarized) is related to the permittivity ϵ_r of the medium. Hence, a direct correlation exists between the luminosity (or darkness in the case of Y-polarized light) of the captured image and the permittivity of the respective medium.

We also performed the electrostatic tomography method with the fan beam algorithm for the OUT-2. Figure 6.13 (a) depicts the image acquired using X-polarized excitation, resulting in significant blurring. The identified inclusions in the resultant image appear as two indistinct areas of brightness near their respective locations. Furthermore, the size and density of these inclusions cannot be discerned. On the other hand, as is clear in Fig. 6.13 (b), we can clearly see two cylindrical inclusions inside the bigger medium for Y-polarized excitation. The bottom-right cylinder is both darker and larger than the upper-left cylinder since it has a higher value of permittivity and larger size.

The shape of the inclusions, in the fan beam method, is more accurate compared to the pencil beam method, and they are not elongated. This is due to the fact that, in order to capture the final image, using the fan beam method, we perform considerably less number of simulations. Thus, the effect of the multi-reflection of electrostatic fields will be minimal. In fact, in the pencil beam method, each detector point will have a specific amount of error, and these errors will accumulate and cause more distortion in the final image.

In tomographic imaging, the choice of excitation must align with the image reconstruction algorithm. To achieve this, electric dipoles oriented in different directions are used, allowing the collected data to match the assumptions of the reconstruction process. Although magnetic sources performed well in earlier sections, the modality introduced here is a new approach with its own specific design considerations, advantages, and requirements.

Chapter 7

Conclusion and Future Work

7.1 Accomplished Work

In Chapter 3, we introduced, for the first time in the field of microwave imaging, a novel imaging modality operating at low frequencies—specifically below 500 MHz. This innovative approach addresses the limitations of conventional microwave imaging systems that typically operate at higher frequencies and struggle with deeper tissue penetration. The proposed system integrates an electrically small dipole antenna and a newly designed metasurface-based antenna capable of efficient operation at 200 MHz.

The metasurface structure is composed of compact unit cells measuring 1 cm $\times$ 1 cm, enabling high spatial resolution imaging and enhancing the system's ability to detect early-stage anomalies. This compact cell size contributes significantly to the localization and characterization of small inclusions, making it particularly suitable for applications such as early breast cancer detection.

The performance of the system was rigorously evaluated through full-wave electromagnetic simulations, demonstrating its ability to accurately detect inclusions as small as 5 mm in radius. To further validate the system's effectiveness, we tested it on high-fidelity numerical breast phantoms, including heterogeneously dense tissue models (BI-RADS density type 3), which closely mimic realistic clinical conditions.

In addition to the hardware development, we implemented a robust classification pipeline using machine learning techniques. A convolutional neural network (CNN) was trained using both supervised and unsupervised learning methods, each of which results in a highly accurate classification framework for distinguishing between healthy and anomalous tissue

regions. The integration of this deep learning approach significantly enhanced the system's diagnostic potential and overall reliability.

In Chapter 4, we explored the underlying physical mechanisms contributing to anomaly detection in low-frequency microwave imaging, with a particular focus on the interaction between electromagnetic fields and biological tissues. Through detailed numerical simulations, it was observed that the magnetic field component plays a significantly more dominant role in the detection of anomalies compared to the electric field. This phenomenon can be theoretically justified by considering the second curl equation in Maxwell's equations, which reveals that the interaction between time-varying magnetic fields and conductive anomalies is more substantial than that of electric fields—especially in high-conductivity biological tissues.

Motivated by this insight, we proposed a novel transmitter design to replace the previously used electrically small dipole antenna. The new source comprises an array of spiral elements engineered to enhance the magnetic field component of the radiated electromagnetic waves. In addition to magnetic field enhancement, the array configuration ensures uniform field illumination across the imaging region, which is essential for reliable and consistent detection of subsurface anomalies.

Full-wave electromagnetic simulations were performed using anatomically realistic numerical phantoms to assess the effectiveness of the proposed spiral array source. The results confirmed a marked improvement in detection performance, validating the advantage of magnetic field–focused excitation in low-frequency imaging scenarios.

As the final contribution of this chapter, the metasurface antenna initially designed in Chapter 3 was fabricated for experimental validation. Due to the large thickness of the dielectric substrate used in the design, conventional printed circuit board (PCB) fabrication methods proved inadequate. To overcome this challenge, a custom fabrication approach was employed, involving multiple PCB layers and a manual stacking process to preserve the structural and electromagnetic integrity of the metasurface.

The fabricated metasurface was then integrated with the newly developed spiral array source in a practical system setup. Preliminary experimental evaluations were conducted using non-human biological tissue samples. The system demonstrated promising performance in detecting embedded anomalies, highlighting the feasibility and potential of the proposed magnetic-field–enhanced imaging modality for future clinical translation.

In Chapter 5, the primary objective was to enhance the spatial resolution of the microwave imaging system by reducing the size of the metasurface unit cells. A new miniaturized metasurface design was proposed to address this goal, allowing for a higher

density of unit cells to be incorporated into the same physical area, thereby increasing the imaging resolution.

The newly designed metasurface offered several significant advantages over the previous design introduced in Chapter 3. Firstly, the lateral dimensions of each unit cell were reduced from 1 cm $\times$ 1 cm to 3.3 mm $\times$ 3.3 mm—approximately one-ninth the area of the original design. This miniaturization enabled a much finer sampling of the electromagnetic field distribution, which is critical for capturing more detailed image features. Secondly, the thickness of the metasurface was reduced from 4 cm to only a few millimeters by employing a novel fabrication technique involving etching on the backside of the substrate. This not only minimized the overall profile of the structure but also improved its mechanical stability and integration capability.

Another key advantage of the new metasurface was its simplified measurement approach. Unlike the previous design that required SMA connectors and coaxial cables connected to a spectrum analyzer—an approach that was both time-consuming and prone to introducing mechanical disturbances—the new design allowed for direct voltage measurement across SMD pads using an oscilloscope. This significantly streamlined the data acquisition process, reduced measurement complexity, and minimized potential sources of noise.

The miniaturized metasurface was fabricated and comprehensively evaluated through both full-wave numerical simulations and experimental testing. The results confirmed a notable improvement in image quality and anomaly detection capability when compared to the earlier system configurations presented in Chapter 4.

Finally, this chapter introduced and implemented an automated data acquisition switching network. This system replaced manual switching with an integrated control mechanism, enabling faster scanning, reducing human error, and improving the signal-to-noise ratio by eliminating mechanical disturbances during measurement. The fabricated switching network marked a crucial step forward in transitioning from a laboratory prototype to a scalable and efficient imaging system suitable for real-world applications.

In Chapter 6, for the first time, we proposed and investigated the feasibility of Electrostatic Computed Tomography (ECT) as a new modality for tomography. By leveraging the analogy between low-frequency electromagnetic wave propagation and electrostatic field behavior, we demonstrated—through detailed numerical simulations—that it is possible to achieve ray-like energy transfer between localized electrostatic sources and detectors. This key behavior underpins the applicability of Radon Transform-based reconstruction algorithms within the electrostatic domain.

Our simulation results confirmed that the electrostatic field lines exhibit sufficient spatial directivity when using physically small (ideally point-like) sources and detectors, enabling high-fidelity image reconstruction through both pencil beam and fan beam scanning methods. The reconstructed images illustrate that the resolution of ECT is primarily governed by the physical size and localization of the source and detector elements, rather than by a fundamental physical limit such as the diffraction limit that constrains conventional wave-based imaging systems. This finding suggests that, in principle, image resolution in ECT is limited not by theory but by practical considerations in sensor design and fabrication technology.

Additionally, our analysis revealed that the polarization orientation of the electrostatic source—which determines the direction of the dipole moment—has a significant influence on the quality and effectiveness of image reconstruction. Understanding and optimizing this polarization effect will be crucial in designing future ECT systems for specific imaging applications.

7.2 Future Work

7.2.1 Suggestion 1

In Chapters 3 to 5, this thesis has focused on developing a novel low-frequency imaging modality, specifically for breast cancer detection, operating below 500 MHz. The research introduced a new metasurface-based microwave imaging system and demonstrated its potential through a series of theoretical, numerical, and experimental studies. While the proposed system shows promise in terms of resolution, sensitivity, and practical feasibility, several opportunities for future enhancement remain.

One of the primary limitations that may arise when comparing this approach to conventional high-resolution modalities, such as X-ray, is the physical constraint on pixel miniaturization. Although efforts were made in Chapter 5 to significantly reduce the unit cell size, there are fundamental and practical boundaries to how small these structures can be made. These limitations stem from several factors, including the finite size of surface-mount components (SMDs), the resolution and capabilities of standard PCB fabrication processes, and the physical constraints associated with resonator miniaturization—particularly at sub-500 MHz frequencies where resonator dimensions are inherently larger due to the longer wavelengths.

To overcome these constraints and further improve spatial resolution, future research

may explore the integration of complementary technologies with the current electromagnetic imaging framework. One promising direction involves the use of thermally sensitive materials and micro-structured pads. These components could interact with electromagnetic energy and induce localized temperature variations that are captured by high-resolution infrared (IR) cameras. Such a hybrid imaging system would leverage the fine spatial resolution of thermal imaging to augment the electromagnetic modality, potentially reducing the effective pixel size and enhancing the image clarity.

By combining low-frequency electromagnetic field interactions with advanced thermal imaging techniques, it may be possible to circumvent the existing resolution barriers imposed by electrical and mechanical constraints, thereby moving one step closer to an affordable, portable, and high-resolution breast cancer detection tool.

7.2.2 Suggestion 2

Another suggestion proposed by the author for future continuation of this work involves the application of advanced algorithms—such as genetic algorithms, convolutional neural networks (CNNs), and signal processing techniques—for the post-processing of the acquired images. One of the primary challenges in translating this modality into a commercially viable breast cancer detection system lies in the subtle variations introduced by small anomalies within biological tissues. These fine perturbations are often difficult to isolate and detect with high specificity and sensitivity.

In the current study, a subtraction-based approach was implemented, where one breast is used as a reference to detect anomalies in the other. Additionally, convolutional neural networks were employed to classify and interpret imaging data. While these approaches have yielded promising results, there remains significant potential for improvement.

Future research could focus on developing or adapting post-processing algorithms specifically optimized to enhance and magnify these subtle electromagnetic variations. Algorithms that can intelligently extract, amplify, and classify weak signals corresponding to small or early-stage anomalies would substantially improve both the sensitivity and specificity of the system. This would be a critical step toward the practical deployment of the proposed imaging modality in clinical environments.

7.2.3 Suggestion 3

In Chapter 6, we proposed Electrostatic Computed Tomography as a viable and potentially transformative imaging modality. It opens new possibilities for low-frequency,

high-resolution tomographic imaging, particularly in contexts where traditional electromagnetic wave propagation is either undesirable or infeasible. Future work will focus on experimental validation, miniaturization of the source and detector components, and further exploration of the interplay between field polarization and reconstruction accuracy.

References

[1] Avinash C Kak, Malcolm Slaney, and Ge Wang. *Principles of computerized tomographic imaging*. Wiley Online Library, 2002.

[2] Dawood Alsaedi, Mohamed El Badawe, and Omar M. Ramahi. A breast cancer detection system using metasurfaces with a convolution neural network: A feasibility study. *IEEE Transactions on Microwave Theory and Techniques*, 70(7):3566–3576, May 2022.

[3] Hamid Akbari-Chelaresi, Dawood Alsaedi, Mohammad El Badawe, Ali M. Albishi, Vahid Nayyeri, and Omar M. Ramahi. Metasurfaces antennas for biological imaging. In *IEEE Microwaves, Antennas, and Propagation Conference (MAPCON)*, pages 1670–1673, 2022. doi: 10.1109/MAPCON56011.2022.10047115.

[4] Mohamed El Badawe, Thamer Almoneef, and Omar Ramahi. A true metasurface antenna. *Scientific Reports*, 6:19268, 01 2016. doi: 10.1038/srep19268.

[5] Wei E. I. Liu, Zhi Ning Chen, Xianming Qing, Jin Shi, and Feng Han Lin. Miniaturized wideband metasurface antennas. *IEEE Transactions on Antennas and Propagation*, 65(12):7345–7349, 2017. doi: 10.1109/TAP.2017.2761550.

[6] Marco Faenzi, Gabriele Minatti, David Gonzalez-Ovejero, Francesco Caminita, Enrica Martini, Cristian Della Giovampaola, and S. Maci. Metasurface antennas: New models, applications and realizations. *Scientific Reports*, 9, 07 2019. doi: 10.1038/s41598-019-46522-z.

[7] Hamid Akbari-Chelaresi, Dawood Alsaedi, Seyed Hossein Mirjahanmardi, Mohamed El Badawe, Ali Almuhlafi, Vahid Nayyeri, and Omar Ramahi. Mammography using low-frequency electromagnetic fields with deep learning. *Scientific Reports*, 13, 08 2023. doi: 10.1038/s41598-023-40494-x.

[8] Waseem Akhtar, Mubashir Aslam, Arif Ali, Kashif Mirza, and Nadeem Ahmad. Film retakes in digital and conventional radiography. *Journal of the College of Physicians and Surgeons Pakistan*, 18(3):151, 2008.

[9] Trine Jensen, M Hansen, KE Jensen, J Pødenphant, TM Hansen, and Lars Hyldstrup. Comparison of dual x-ray absorptiometry (dxa), digital x-ray radiogrammetry (dxr), and conventional radiographs in the evaluation of osteoporosis and bone erosions in patients with rheumatoid arthritis. *Scandinavian journal of rheumatology*, 34(1):27–33, 2005.

[10] Hao Chen, Zhou Xu, and Ming Li. The application and development of radiography technology based on x-ray. In *International Symposium on Photoelectronic Detection and Imaging 2009: Terahertz and High Energy Radiation Detection Technologies and Applications*, volume 7385, pages 31–38. SPIE, 2009.

[11] Xiangyu Ou, Xue Chen, Xianning Xu, Lili Xie, Xiaofeng Chen, Zhongzhu Hong, Hua Bai, Xiaowang Liu, Qiushui Chen, Lin Li, et al. Recent development in x-ray imaging technology: Future and challenges. *Research*, 2021.

[12] Scott L Wellington and Harold J Vinegar. X-ray computerized tomography. *Journal of petroleum technology*, 39(08):885–898, 1987.

[13] Leon Axel, Peter H Arger, and Robert A Zimmerman. Applications of computerized tomography to diagnostic radiology. *Proceedings of the IEEE*, 71(3):293–297, 1983.

[14] Dorthe Wildenschild, CMP Vaz, ML Rivers, D Rikard, and BSB Christensen. Using x-ray computed tomography in hydrology: systems, resolutions, and limitations. *Journal of Hydrology*, 267(3-4):285–297, 2002.

[15] James Anthony Seibert. Projection x-ray imaging: Radiography, mammography, fluoroscopy. *Health Physics*, 116(2):148–156, 2019.

[16] AR Cowen, AG Davies, and MU Sivananthan. The design and imaging characteristics of dynamic, solid-state, flat-panel x-ray image detectors for digital fluoroscopy and fluorography. *Clinical radiology*, 63(10):1073–1085, 2008.

[17] Tommaso Cerciello, Paolo Bifulco, Mario Cesarelli, and Antonio Fratini. A comparison of denoising methods for x-ray fluoroscopic images. *Biomedical Signal Processing and Control*, 7(6):550–559, 2012.

[18] AR Cowen. Digital x-ray imaging. *Measurement Science and Technology*, 2(8):691, 1991.

[19] JW Jeong, JT Kang, JW Kim, S Park, ML Lee, and YH Song. Digital x-ray technology and applications. *Electronics and Telecommunications Trends*, 34(5):1–13, 2019.

[20] Varayini Yoganathan. Digital radiography in endodontics: advantages and disadvantages. *Endodontic*, page 5.

[21] Girish Katti, Syeda Arshiya Ara, and Ayesha Shireen. Magnetic resonance imaging (mri)–a review. *International journal of dental clinics*, 3(1):65–70, 2011.

[22] Chelsea S Kidwell and Amie W Hsia. Imaging of the brain and cerebral vasculature in patients with suspected stroke: advantages and disadvantages of ct and mri. *Current neurology and neuroscience reports*, 6(1):9–16, 2006.

[23] Gerd Muehllehner and Joel S Karp. Positron emission tomography. *Physics in Medicine & Biology*, 51(13):R117, 2006.

[24] Dale L Bailey, Michael N Maisey, David W Townsend, and Peter E Valk. *Positron emission tomography*, volume 2. Springer, 2005.

[25] Vincent Chan and Anahi Perlas. Basics of ultrasound imaging. *Atlas of ultrasound-guided procedures in interventional pain management*, pages 13–19, 2011.

[26] Peter NT Wells. Ultrasound imaging. *Physics in medicine & biology*, 51(13):R83, 2006.

[27] J Eber and C Villasenor. Ultrasound: advantages, disadvantages, and controversies. In *Nurse practitioner forum*, volume 2, pages 239–242, 1991.

[28] Uwe Hampel, Laurent Babout, Robert Banasiak, Eckhard Schleicher, Manuchehr Soleimani, Thomas Wondrak, Marko Vauhkonen, Timo Lähivaara, Chao Tan, Brian Hoyle, and Alexander Penn. A review on fast tomographic imaging techniques and their potential application in industrial process control. *Sensors*, 22:2309, 03 2022. doi: 10.3390/s22062309.

[29] Maged A Aldhaeebi, Thamer S Almoneef, Hussein Attia, and Omar M Ramahi. Electrically small magnetic probe with pca for near-field microwave breast tumors detection. *Progress In Electromagnetics Research M*, 84:177–186, Aug. 2019.

[30] Maged A Aldhaeebi, Thamer S Almoneef, Abdulbaset Ali, Zhao Ren, and Omar M Ramahi. Near field breast tumor detection using ultra-narrow band probe with machine learning techniques. *Scientific reports*, 8(1):1–16, Aug. 2018.

[31] Natalia K. Nikolova. Microwave imaging for breast cancer. *IEEE Microwave Magazine*, 12(7):78–94, Dec. 2011. doi: 10.1109/MMM.2011.942702.

[32] SS Chaudhary, RK Mishra, Arvind Swarup, and Joy M Thomas. Dielectric properties of normal & malignant human breast tissues at radiowave & microwave frequencies. *Indian journal of biochemistry & biophysics*, 21(1):76–79, Feb. 1984.

[33] B. Bocquet, J.C. van de Velde, A. Mamouni, Y. Leroy, G. Giaux, J. Delannoy, and D. Delvalee. Microwave radiometric imaging at 3 ghz for the exploration of breast tumors. *IEEE Transactions on Microwave Theory and Techniques*, 38(6):791–793, 1990. doi: 10.1109/22.130978.

[34] Jian Song, Zhiqin Zhao, Jiangniu Wu, Xiaozhang Zhu, Zaiping Nie, and Qing-Huo Liu. Thermo-acoustic imaging for different breast tissues in microwave induced thermo-acoustic tomography system. In *2013 IEEE Antennas and Propagation Society International Symposium (APSURSI)*, pages 2032–2033, 2013. doi: 10.1109/APS.2013.6711674.

[35] C. Pichot, L. Jofre, G. Peronnet, and J. Bolomey. Active microwave imaging of inhomogeneous bodies. *IEEE Transactions on Antennas and Propagation*, 33(4): 416–425, 1985. doi: 10.1109/TAP.1985.1143603.

[36] Paul M Meaney, Margaret W Fanning, Dun Li, Steven P Poplack, and Keith D Paulsen. A clinical prototype for active microwave imaging of the breast. *IEEE Transactions on Microwave Theory and Techniques*, 48(11):1841–1853, Nov. 2000.

[37] Paul M. Meaney, Margaret W. Fanning, Roberta M. di Florio-Alexander, Peter A. Kaufman, Shireen D. Geimer, Tian Zhou, and Keith D. Paulsen. Microwave tomography in the context of complex breast cancer imaging. In *2010 Annual International Conference of the IEEE Engineering in Medicine and Biology*, pages 3398–3401, 2010. doi: 10.1109/IEMBS.2010.5627932.

[38] E.C. Fear, X. Li, S.C. Hagness, and M.A. Stuchly. Confocal microwave imaging for breast cancer detection: localization of tumors in three dimensions. *IEEE Transactions on Biomedical Engineering*, 49(8):812–822, 2002. doi: 10.1109/TBME.2002.800759.

[39] Fengzhou Wang, Tughrul Arslan, and Guohua Wang. Breast cancer detection with microwave imaging system using wearable conformal antenna arrays. In *2017 IEEE International Conference on Imaging Systems and Techniques (IST)*, pages 1–6, 2017. doi: 10.1109/IST.2017.8261547.

[40] A.E. Bulyshev, S.Y. Semenov, A.E. Souvorov, R.H. Svenson, A.G. Nazarov, Y.E. Sizov, and G.P. Tatsis. Computational modeling of three-dimensional microwave tomography of breast cancer. *IEEE Transactions on Biomedical Engineering*, 48(9): 1053–1056, 2001. doi: 10.1109/10.942596.

[41] A.E. Souvorov, A.E. Bulyshev, S.Y. Semenov, R.H. Svenson, and G.P. Tatsis. Two-dimensional computer analysis of a microwave flat antenna array for breast cancer tomography. *IEEE Transactions on Microwave Theory and Techniques*, 48(8):1413–1415, 2000. doi: 10.1109/22.859490.

[42] L. Jofre, M.S. Hawley, A. Broquetas, E. de los Reyes, M. Ferrando, and A.R. Elias-Fuste. Medical imaging with a microwave tomographic scanner. *IEEE Transactions on Biomedical Engineering*, 37(3):303–312, 1990. doi: 10.1109/10.52331.

[43] Sima Noghanian, Abas Sabouni, Travis Desell, and Ali Ashtari. *Microwave Tomography: Global Optimization, Parallelization and Performance Evaluation*. 03 2014. ISBN 978-1-4939-0751-9. doi: 10.1007/978-1-4939-0752-6.

[44] Qianqian Fang, P.M. Meaney, and K.D. Paulsen. Microwave image reconstruction of tissue property dispersion characteristics utilizing multiple-frequency information. *IEEE Transactions on Microwave Theory and Techniques*, 52(8):1866–1875, 2004. doi: 10.1109/TMTT.2004.832014.

[45] S.Y. Semenov, A.E. Bulyshev, A.E. Souvorov, R.H. Svenson, Y.E. Sizov, V.Y. Vorisov, V.G. Posukh, I.M. Kozlov, A.G. Nazarov, and G.P. Tatsis. Microwave tomography: theoretical and experimental investigation of the iteration reconstruction algorithm. *IEEE Transactions on Microwave Theory and Techniques*, 46(2):133–141, 1998. doi: 10.1109/22.660979.

[46] Tomasz M. Grzegorczyk, Paul M. Meaney, Peter A. Kaufman, Roberta M. diFlorio Alexander, and Keith D. Paulsen. Fast 3-d tomographic microwave imaging for breast cancer detection. *IEEE Transactions on Medical Imaging*, 31(8):1584–1592, 2012. doi: 10.1109/TMI.2012.2197218.

[47] Seong-Ho Son, Nikolai A. Simonov, Hyuk Je Kim, Jong-Moon Lee, and Soon-Ik Jeon. Preclinical prototype development of a microwave tomography system for breast

cancer detection. *ETRI Journal*, 32, 2010. URL https://api.semanticscholar.org/CorpusID:62709751.

[48] J. E. Bridges. Non-invasive system for breast cancer detection, January 1998.

[49] E. C. Fear, J. Bourqui, C. Curtis, D. Mew, B. Docktor, and C. Romano. Microwave breast imaging with a monostatic radar-based system: A study of application to patients. *IEEE Transactions on Microwave Theory and Techniques*, 61(5):2119–2128, 2013. doi: 10.1109/TMTT.2013.2255884.

[50] Emily Porter, Evgeny Kirshin, Adam Santorelli, Mark Coates, and Milica Popović. Time-domain multistatic radar system for microwave breast screening. *IEEE Antennas and Wireless Propagation Letters*, 12:229–232, 2013. doi: 10.1109/LAWP.2013.2247374.

[51] D. Tajik, F. Foroutan, D. S. Shumakov, A. D. Pitcher, and N. K. Nikolova. Real-time microwave imaging of a compressed breast phantom with planar scanning. *IEEE Journal of Electromagnetics, RF and Microwaves in Medicine and Biology*, 2(3):154–162, 2018.

[52] D. Tajik, R. Kazemivala, and N. K. Nikolova. Real-time imaging with simultaneous use of born and rytov approximations in quantitative microwave holography. *IEEE Transactions on Microwave Theory and Techniques*, 70(3):1896–1909, 2022.

[53] R. Kazemivala, D. Tajik, and N. K. Nikolova. Simultaneous use of the born and rytov approximations in real-time imaging with fourier-space scattered power mapping. *IEEE Transactions on Microwave Theory and Techniques*, 70(5):2904–2920, 2022.

[54] R. Kazemivala and N. K. Nikolova. Real-time synthetic aperture radar imaging with random sampling employing scattered power mapping. *Sensors*, 24(12):3849, 2024.

[55] Seyed Hossein Mirjahanmardi and Omar M. Ramahi. Toward computerized tomography with microwaves. *IEEE Transactions on Microwave Theory and Techniques*, 70(11):5278–5288, 2022. doi: 10.1109/TMTT.2022.3205635.

[56] L. Sani, A. Vispa, R. Loretoni, M. Duranti, N. Ghavami, D. Alvarez Sánchez-Bayuela, and et al. Breast lesion detection through mammowave device: Empirical detection capability assessment of microwave images' parameters. *PLoS ONE*, 16(4):e0250005, 2021.

[57] DÁ. Sánchez-Bayuela, N. Ghavami, G. Tiberi, L. Sani, A. Vispa, and et al. A multicentric, single arm, prospective, stratified clinical investigation to evaluate mammowave's ability in breast lesions detection. *PLoS ONE*, 18(7):e0288312, 2023.

[58] B.M. Moloney, P.F. McAnena, S.M. Elwahab, A. Fasoula, L. Duchesne, J.D. Gil Cano, and et al. The wavelia microwave breast imaging system–tumour discriminating features and their clinical usefulness. *Br J Radiol*, 94:20210907, 2021.

[59] M. Shere, I. Lyburn, R. Sidebottom, H. Massey, C. Gillett, and L. Jones. MARIA m5: A multicentre clinical study to evaluate the ability of the micrima radio-wave radar breast imaging system (MARIA) to detect lesions in the symptomatic breast. *Eur. J. Radiol.*, 116:61–67, Jul. 2019.

[60] A. Janjic and et al. SAFE: A novel microwave imaging system design for breast cancer screening and early detection—clinical evaluation. *Diagnostics*, 11(533), 2021. doi: 10.3390/diagnostics11030533.

[61] Katja Kemp Jacobsen and et al. Comparing sensitivity and specificity of screening mammography in the united states and denmark. *International Journal of Cancer*, 137(9):2198–2207, 2015.

[62] M. Zeeshan, B. Salam, Q.S.B. Khalid, S. Alam, and R. Sayani. Diagnostic accuracy of digital mammography in the detection of breast cancer. *Cureus*, 10(4):e2448, 2018. doi: 10.7759/cureus.2448.

[63] S.C. Hagness, A. Taflove, and J.E. Bridges. Two-dimensional fdtd analysis of a pulsed microwave confocal system for breast cancer detection: fixed-focus and antenna-array sensors. *IEEE Transactions on Biomedical Engineering*, 45(12):1470–1479, 1998. doi: 10.1109/10.730440.

[64] E.C. Fear, J. Sill, and M.A. Stuchly. Experimental feasibility study of confocal microwave imaging for breast tumor detection. *IEEE Transactions on Microwave Theory and Techniques*, 51(3):887–892, 2003. doi: 10.1109/TMTT.2003.808630.

[65] C.J. Shannon, M. Okoniewski, and E.C. Fear. A dielectric filled ultra-wideband antenna for breast cancer detection. In *IEEE Antennas and Propagation Society International Symposium. Digest. Held in conjunction with: USNC/CNC/URSI North American Radio Sci. Meeting (Cat. No.03CH37450)*, volume 1, pages 218–221 vol.1, 2003. doi: 10.1109/APS.2003.1217438.

[66] R. Nilavalan, J. Leendertz, I.J. Craddock, A. Preece, and R. Benjamin. Numerical analysis of microwave detection of breast tumours using synthetic focussing techniques. In *IEEE Antennas and Propagation Society Symposium, 2004.*, volume 3, pages 2440–2443 Vol.3, 2004. doi: 10.1109/APS.2004.1331866.

[67] P. Kosmas and C.M. Rappaport. A matched-filter fdtd-based time reversal approach for microwave breast cancer detection. *IEEE Transactions on Antennas and Propagation*, 54(4):1257–1264, 2006. doi: 10.1109/TAP.2006.872670.

[68] Yifan Chen, Erry Gunawan, Kay Soon Low, Shih-chang Wang, Cheong Boon Soh, and Thomas Choudary Putti. Time-reversal ultrawideband breast imaging: Pulse design criteria considering multiple tumors with unknown tissue properties. *IEEE Transactions on Antennas and Propagation*, 56(9):3073–3077, 2008. doi: 10.1109/TAP.2008.928811.

[69] Maciej Klemm, Ian J. Craddock, Jack A. Leendertz, Alan Preece, and Ralph Benjamin. Radar-based breast cancer detection using a hemispherical antenna array—experimental results. *IEEE Transactions on Antennas and Propagation*, 57 (6):1692–1704, 2009. doi: 10.1109/TAP.2009.2019856.

[70] Jianqi Teo, Yifan Chen, Cheong Boon Soh, Erry Gunawan, Kay Soon Low, Thomas Choudary Putti, and Shih-Chang Wang. Breast lesion classification using ultrawideband early time breast lesion response. *IEEE Transactions on Antennas and Propagation*, 58(8):2604–2613, 2010. doi: 10.1109/TAP.2010.2050423.

[71] M. Klemm, D. Gibbins, J. Leendertz, T. Horseman, A. W. Preece, R. Benjamin, and I. J. Craddock. Development and testing of a 60-element uwb conformal array for breast cancer imaging. In *Proceedings of the 5th European Conference on Antennas and Propagation (EUCAP)*, pages 3077–3079, 2011.

[72] Ananda Sanagavarapu Mohan, Md Delwar Hossain, and Mohammed Jainul Abedin. Beamspace based time reversal processing for breast cancer detection. In *Proceedings of the 2012 IEEE International Symposium on Antennas and Propagation*, pages 1–2, 2012. doi: 10.1109/APS.2012.6348952.

[73] Douglas Kurrant and Elise Fear. Defining regions of interest for microwave imaging using near-field reflection data. *IEEE Transactions on Microwave Theory and Techniques*, 61(5):2137–2145, 2013. doi: 10.1109/TMTT.2013.2250993.

[74] M. A. Elahi, A. Shahzad, M. Glavin, E. Jones, and M. O'Halloran. Hybrid artifact removal for confocal microwave breast imaging. *IEEE Antennas and Wireless Propagation Letters*, 13:149–152, 2014. doi: 10.1109/LAWP.2014.2298975.

[75] Hyuna Sung, Jacques Ferlay, Rebecca L Siegel, Mathieu Laversanne, Isabelle Soerjomataram, Ahmedin Jemal, and Freddie Bray. Global cancer statistics 2020: GLOBOCAN estimates of incidence and mortality worldwide for 36 cancers in 185 countries. *CA: a cancer journal for clinicians*, 71(3):209–249, Feb. 2021.

[76] Md Delwar Hossain and Ananda Sanagavarapu Mohan. Cancer detection in highly dense breasts using coherently focused time-reversal microwave imaging. *IEEE Transactions on Computational Imaging*, 3(4):928–939, Aug. 2017.

[77] Mark Lewis, Akash Prashar, Andoni P Toms, Matthew P Armon, and Paul N Malcolm. The diagnosis of thoracic outlet syndrome. *Journal of Vascular Diagnostics and Interventions*, 2:113–120, Oct 2014.

[78] George K Lui, Arwa Saidi, Ami B Bhatt, Luke J Burchill, Jason F Deen, Michael G Earing, Michael Gewitz, Jonathan Ginns, Joseph D Kay, Yuli Y Kim, et al. Diagnosis and management of noncardiac complications in adults with congenital heart disease: a scientific statement from the american heart association. *Circulation*, 136(20):e348–e392, Oct. 2017.

[79] Andrew P Smith, Patricia A Hall, Donna M Marcello, et al. Emerging technologies in breast cancer detection. *Radiology management*, 26(4):16–27, Aug. 2004.

[80] Ahmad Ashraf Abdul Halim, Allan Melvin Andrew, Mohd Najib Mohd Yasin, Mohd Amiruddin Abd Rahman, Muzammil Jusoh, Vijayasarveswari Veeraperumal, Hasliza A Rahim, Usman Illahi, Muhammad Khalis Abdul Karim, and Edgar Scavino. Existing and emerging breast cancer detection technologies and its challenges: A review. *Applied Sciences*, 11(22):10753, Nov. 2021.

[81] S.K. Davis, H. Tandradinata, S.C. Hagness, and B.D. Van Veen. Ultrawideband microwave breast cancer detection: a detection-theoretic approach using the generalized likelihood ratio test. *IEEE Transactions on Biomedical Engineering*, 52(7): 1237–1250, 2005. doi: 10.1109/TBME.2005.847528.

[82] Maged A Aldhaeebi, Khawla Alzoubi, Thamer S Almoneef, Saeed M Bamatraf, Hussein Attia, and Omar M Ramahi. Review of microwaves techniques for breast cancer detection. *Sensors*, 20(8):2390, April 2020.

[83] Haolin Zhang, Maokun Li, Fan Yang, Shenheng Xu, Yan Yin, Hongyu Zhou, Yubo Yang, Sihang Zeng, and Jianchong Shao. A feasibility study of 2-d microwave thorax imaging based on the supervised descent method. *Electronics*, 10(3):352, Feb 2021.

[84] AT Mobashsher, KS Bialkowski, AM Abbosh, and S Crozier. Design and experimental evaluation of a non-invasive microwave head imaging system for intracranial haemorrhage detection. *Plos one*, 11(4):e0152351, April 2016.

[85] Zhao Wang, Eng Gee Lim, Yujun Tang, and Mark Leach. Medical applications of microwave imaging. *The Scientific World Journal*, 2014, Oct. 2014.

[86] Benjamin R Lavoie, Michal Okoniewski, and Elise C Fear. Estimating the effective permittivity for reconstructing accurate microwave-radar images. *PloS one*, 11(9): e0160849, Sep. 2016.

[87] Mariya Lazebnik, Dijana Popovic, Leah McCartney, Cynthia B Watkins, Mary J Lindstrom, Josephine Harter, Sarah Sewall, Travis Ogilvie, Anthony Magliocco, Tara M Breslin, et al. A large-scale study of the ultrawideband microwave dielectric properties of normal, benign and malignant breast tissues obtained from cancer surgeries. *Physics in medicine and biology*, 52(20):6093, Oct. 2007.

[88] Lorenzo Sani, Alessandro Vispa, Riccardo Loretoni, Michele Duranti, Navid Ghavami, Daniel Alvarez Sánchez-Bayuela, Stefano Caschera, Martina Paoli, Alessandra Bigotti, Mario Badia, et al. Breast lesion detection through mammowave device: Empirical detection capability assessment of microwave images parameters. *Plos one*, 16(4):e0250005, April 2021.

[89] M Klemm, JA Leendertz, D Gibbins, IJ Craddock, A Preece, and R Benjamin. Microwave radar-based breast cancer detection: Imaging in inhomogeneous breast phantoms. *IEEE Antennas and Wireless Propagation Letters*, 8:1349–1352, Nov. 2009.

[90] O. M. Ramahi, D. Alsaedi, and H. Akbari-Chelaresi. Mammography apparatus using low-frequency electromagnetic fields, June U.S. Provisional application. filing date, June 12, 2023.

[91] Salvatore Caorsi and Paolo Gamba. Electromagnetic detection of dielectric cylinders by a neural network approach. *IEEE Transactions on Geoscience and Remote Sensing*, 37(2):820–827, 1999.

[92] Wenyi Shao and Yong Du. Microwave imaging by deep learning network: Feasibility and training method. *IEEE transactions on antennas and propagation*, 68(7):5626–5635, 2020.

[93] Pratik Shah and Mahta Moghaddam. Super resolution for microwave imaging: A deep learning approach. In *2017 IEEE International Symposium on Antennas and Propagation & USNC/URSI National Radio Science Meeting*, pages 849–850. IEEE, 2017.

[94] Thamer S Almoneef and Omar M Ramahi. Metamaterial electromagnetic energy harvester with near unity efficiency. *Applied Physics Letters*, 106(15):153902, April 2015.

[95] Ali Albishi and Omar M. Ramahi. Detection of surface and subsurface cracks in metallic and non-metallic materials using a complementary split-ring resonator. *Sensors*, 14(10):19354–19370, Oct. 2014.

[96] Bagher Ghaderi, Vahid Nayyeri, Mohammad Soleimani, and Omar M. Ramahi. Multi-polarisation electromagnetic energy harvesting with high efficiency. volume 12, pages 2271–2275, 2018.

[97] CST Microwave Studio, version 2022, https://www.cst.com, last access: Dec., 2022.

[98] Seyed H. Mirjahanmardi, Saleh Ba Raean, Hamid Akbari-Chelaresi, Vahid Nayyeri, and Omar M. Ramahi. Computerized tomography with low-frequency electromagnetic radiation. In *2023 International Microwave and Antenna Symposium (IMAS)*, pages 95–97, 2023. doi: 10.1109/IMAS55807.2023.10066933.

[99] Omar M. Ramahi, Saleh Ba Raean, Hamid Akbari-Chelaresi, Seyed H. Mirjahanmardi, and Vahid Nayyeri. Computerized tomography with radon transform using microwaves and electrostatics. In *2022 IEEE International RF and Microwave Conference (RFM)*, pages 1–3, 2022. doi: 10.1109/RFM56185.2022.10064983.

[100] Yasuko Nagao, Yoshihiro Kawaguchi, Yasuyuki Sugiyama, Shigetoyo Saji, and Yoshitomo Kashiki. Relationship between mammographic density and the risk of breast cancer in japanese women: a case-control study. *Breast Cancer*, 10(3):228–233, July 2003.

[101] Karla Kerlikowske, Weiwei Zhu, Anna NA Tosteson, Brian L Sprague, Jeffrey A Tice, Constance D Lehman, Diana L Miglioretti, and Breast Cancer Surveillance

Consortium. Identifying women with dense breasts at high risk for interval cancer: a cohort study. *Annals of internal medicine*, 162(10):673–681, May 2015.

[102] M. J. Yaffe, J. M. Boone, N. Packard, O Alonzo-Proulx, S. Y. Huang, C. L. Peressotti, A. Al-Mayah, and K. Brock. The myth of the 50-50 breast. *Medical physics*, 36(12): 5437–5443, 2009.

[103] D. A. Kennedy, T. Lee, and D. Seely. A comparative review of thermography as a breast cancer screening technique. *Integrative cancer therapies*, 8(1):9–16, 2009.

[104] N. Carrara. Dielectric properties of body tissues. http://niremf.ifac.cnr.it/tissprop. URL http://niremf.ifac.cnr.it/tissprop.

[105] Maciej Klemm, Jack Leendertz, David Gibbins, I.J. Craddock, Alan Preece, and Ralph Benjamin. Microwave radar-based differential breast cancer imaging: Imaging in homogeneous breast phantoms and low contrast scenarios. *Antennas and Propagation, IEEE Transactions on*, 58:2337 – 2344, 08 2010. doi: 10.1109/TAP.2010.2048860.

[106] S Hudson, L Wilkinson, R Denholm, B De Stavola, and I Dos-Santos-Silva. Ethnic and age differences in right-left breast asymmetry in a large population-based screening population. *The British journal of biology*, 93(1105):20190328, 2019.

[107] AM Abbosh, B Mohammed, and KS Bialkowski. Differential microwave imaging of the breast pair. *IEEE Antennas and Wireless Propagation Letters*, 15:1434–1437, 2015.

[108] University of wisconsin cross-disciplinary electromagnetics laboratory. https://uwcem.ece.wisc.edu. URL https://uwcem.ece.wisc.edu.

[109] M Lazebnik, L McCartney, D Popovic, C. B Watkins, M. J Lindstrom, J Harter, S Sewall, A Magliocco, J. H. Booske, and S. C. Okoniewski M.and Hagness. A large-scale study of the ultrawideband microwave dielectric properties of normal breast tissue obtained from reduction surgeries. *Physics in medicine and biology*, 52(10): 2637–2656, 2007.

[110] Mariya Lazebnik, Michal Okoniewski, John H Booske, and Susan C Hagness. Highly accurate debye models for normal and malignant breast tissue dielectric properties at microwave frequencies. *IEEE microwave and wireless components letters*, 17(12): 822–824, 2007.

[111] Vitaliy Zhurbenko. Challenges in the design of microwave imaging systems for breast cancer detection. *Advances in Electrical and Computer Engineering*, 11, 02 2011. doi: 10.4316/AECE.2011.01015.

[112] Rohit Chandra, Huiyuan Zhou, Ilangko Balasingham, and Ram Narayanan. On the opportunities and challenges in microwave medical sensing and imaging. *IEEE transactions on bio-medical engineering*, 62, 05 2015. doi: 10.1109/TBME.2015.2432137.

[113] Paul Meaney, Amir Golnabi, Neil Epstein, Shireen Geimer, Margaret Fanning, John Weaver, and Keith Paulsen. Integration of microwave tomography with magnetic resonance for improved breast imaging. *Medical Physics*, 40:103101, 09 2013. doi: 10.1118/1.4820361.

[114] Paul Meaney, Fridon Shubitidze, Margaret Fanning, Maciej Kmiec, Neil Epstein, and Keith Paulsen. Surface wave multipath signals in near-field microwave imaging. *International journal of biomedical imaging*, 2012:697253, 04 2012. doi: 10.1155/2012/697253.

[115] Majid Ostadrahimi, Amer Zakaria, Joe LoVetri, and Lotfollah Shafai. A near-field dual polarized (te–tm) microwave imaging system. *IEEE Transactions on Microwave Theory and Techniques*, 61(3):1376–1384, 2013. doi: 10.1109/TMTT.2012.2237181.

[116] David M. Sheen, Douglas L. McMakin, and Thomas E. Hall. Near field imaging at microwave and millimeter wave frequencies. In *2007 IEEE/MTT-S International Microwave Symposium*, pages 1693–1696, 2007. doi: 10.1109/MWSYM.2007.380033.

[117] Dun Li, Paul Meaney, Timothy Raynolds, Sarah Pendergrass, Margaret Fanning, and Keith Paulsen. Parallel-detection microwave spectroscopy system for breast imaging. *Review of Scientific Instruments*, 75:2305–2313, 06 2004. doi: 10.1063/1.1764609.

[118] Hamid Akbari-Chelaresi, Pooria Salami, and Leila Yousefi. Far-field sub-wavelength imaging using high-order dielectric continuous metasurfaces. *Opt. Express*, 30(21): 39025–39039, Oct 2022. doi: 10.1364/OE.470221. URL https://opg.optica.org/oe/abstract.cfm?URI=oe-30-21-39025.

[119] COMSOL Multiphysics® v. 6.0. www.comsol.com. COMSOL AB, Stockholm, Sweden.

[120] Gabriele Minatti, Enrica Martini, and Stefano Maci. Efficiency of metasurface antennas. *IEEE Transactions on Antennas and Propagation*, 65(4):1532–1541, 2017. doi: 10.1109/TAP.2017.2669728.

[121] Xu Li, E.J. Bond, B.D. Van Veen, and S.C. Hagness. An overview of ultra-wideband microwave imaging via space-time beamforming for early-stage breast-cancer detection. *IEEE Antennas and Propagation Magazine*, 47(1):19–34, 2005. doi: 10.1109/MAP.2005.1436217.

[122] Alireza Mashal, Fuqiang Gao, and Susan C Hagness. Heterogeneous anthropomorphic phantoms with realistic dielectric properties for microwave breast imaging experiments. *Microwave and optical technology letters*, 53(8):1896–1902, 2011.

[123] Earl Zastrow, Shakti K Davis, Mariya Lazebnik, Frederick Kelcz, Barry D Van Veen, and Susan C Hagness. Development of anatomically realistic numerical breast phantoms with accurate dielectric properties for modeling microwave interactions with the human breast. *IEEE Transactions on Biomedical Engineering*, 55(12):2792–2800, 2008.

[124] Mariya Lazebnik, Leah McCartney, Dijana Popovic, Cynthia B Watkins, Mary J Lindstrom, Josephine Harter, Sarah Sewall, Anthony Magliocco, John H Booske, Michal Okoniewski, et al. A large-scale study of the ultrawideband microwave dielectric properties of normal breast tissue obtained from reduction surgeries. *Physics in medicine and biology*, 52(10):2637, 2007.

[125] Deborah A Kennedy, Tanya Lee, and Dugald Seely. A comparative review of thermography as a breast cancer screening technique. *Integrative cancer therapies*, 8(1): 9–16, 2009.

[126] Maciej Klemm, Jack A Leendertz, David Gibbins, Ian J Craddock, Alan Preece, and Ralph Benjamin. Microwave radar-based differential breast cancer imaging: Imaging in homogeneous breast phantoms and low contrast scenarios. *IEEE Transactions on Antennas and Propagation*, 58(7):2337–2344, 2010.

[127] AM Abbosh, B Mohammed, and KS Bialkowski. Differential microwave imaging of the breast pair. *IEEE Antennas and Wireless Propagation Letters*, 15:1434–1437, 2015.